Magnetism and Magnetotransport Studies of IV-VI Ferromagnetic Semiconductor

LIM SZE TER

(B. ENG. (Hons.), NUS)

A THESIS SUBMITTED FOR THE DEGREE OF

DOCTOR OF PHILOSOPHY

NUS Graduate School for Interactive Sciences and Engineering

NATIONAL UNIVERSITY OF SINGAPORE

2011

ACKNOWLEDGEMENTS

I would first like to thank my supervisors and thesis advisors Associate Professor Teo Kie Leong, Associate Professor Thomas Liew and Professor Chong Tow Chong for providing me the numerous opportunities to learn and grow as a person and scientist under their tutelage. I am truly grateful for the strong support you have given my research, as well as your guidiance and motivations throughout these four years.

At the same time, I would like to thank my family for their kind understanding, support and encouragement. Equally noble and important is my wife Bijun who always has faith in me and staying by my side all these time.

I am also grateful to Dr Ko Viloane, Dr Mambakkam Govindan Sreenivasan, Dr Chen Wenqian, Dr Randall Law, Dr Sunny Lua, Dr Bi Jing Feng, Dr Yang Yi, Dr Jonathan Cheah and Lu Hui who have provided me with not only technical and experimental assistance, but also company and entertainment that made the research process much more enjoyable.

Finally, I would like to thank the Agency for Science, Technology and Research (A*STAR) and Data Storage Institute (DSI) for their financial support, the NUS Graduate School for Integrative Sciences and Engineering (NGS) staff for being so efficient and friendly in handling our administrative issues, and all the staff and students of DSI, ISML and AML for their friendship.

CONTENTS

ABSTRACT

Among the IV-VI ferromagnetic semiconductors (FMS), $Ge_{1-x}Mn_xTe$ reveals relatively high Curie temperature (T_c) of 200 K under appropriate growth conditions. This makes it a promising material for spintronic applications and warrants much research interests. This thesis focuses on the study of magnetic and transport properties of $Ge_{1-x}Mn_xTe$ thin films grown by molecular beam epitaxy. Anomalous Hall effect is clearly observed in the samples which can be attributed to extrinsic skew scattering. The interplay between localized magnetic moments from the Mn ions and the free carriers resulting from the presence of both Ge vacancy and Ge-Te disorder type of defects determine the ferromagnetic properties in $Ge_{1-x}Mn_xTe$. This interaction is investigated by means of magnetotransport studies in $Ge_{1-x}Mn_xTe$ under the effect of hydrostatic pressure (P). The T_c is observed to change with P which is due to the increase in carrier concentration responsible for the interactions between Mn ions. A two valence model as well as RKKY interaction are invoked to explain these results. Magnetoresistance (MR) measurements have been used to investigate the localization and antilocalization effects. The spin-orbit, elastic and inelastic scattering times as well as coherence length as a function of pressure are obtained from the fitting of MR results. Additionally, exchange bias effect (EB) of $Ge_{1-x}Mn_xTe$ with antiferromagnetic MnTe and MnO materials has been investigated. While $Ge_{1-x}Mn_xTe$-MnTe system only leads to a modification of coercivity field, a negative EB shift in the hysteresis loop is observed for $Ge_{1-x}Mn_xTe$-MnO bilayer when it is cooled in applied field. Our findings pose challenges as well as opportunities for future studies of $Ge_{1-x}Mn_xTe$ for spintronic applications.

LIST OF FIGURES

LIST OF TABLES

LIST OF SYMBOLS AND ABBREVIATIONS

AHE	Anomalous Hall effect
ALD	Atomic layer deposition
AFM	Antiferromagnetic or atomic force microscopy
BEP	Beam equivalent pressure
DMS	Diluted magnetic semiconductor
EB	Exchange bias
EDS	Energy-dispersive X-ray spectroscopy
FET	Field effect transistor
FMS	Ferromagnetic semiconductor
FM	Ferromagnetic
GMR	Giant magnetoresistance
LED	Light emitting diode
MRAM	Magnetoresistive random access memory
MBE	Molecular beam epitaxy
MOVPE	Metal organic vapour phase epitaxy
MIT	Metal insulator transition
MR	Magnetoresistance
PLD	Pulse laser deposition
RKKY	Ruderman-Kittel-Kasuya-Yosida
RTD	Resonant tunnelling device
RHEED	Reflection high energy electron diffraction
SQUID	Superconducting quantum interference device
TEM	Transmission electron microscopy
UHV	Ultrahigh vacuum
VB	Valence band
WL	Weak localization
XAS	X-ray absorption spectroscopy
XMCD	X-ray magnetic circular dicroism
XRD	X-ray diffraction
XPS	X-ray photoelectron spectroscopy
M-T	Temperature dependence of magnetization
M-H	Magnetic field dependence of magnetization (hysteresis loop)
a or a_o	Lattice constant
a_H	Bohr radius
T_s	Substrate temperature

T_N	Néel temperature
T_B	Blocking temperature
T_c	Curie temperature
T_R	Temperature at resistivity minimum
$\rho(T)$	Temperature dependence of resistivity
ρ_M	Resistivity minimum
ρ_{xy}	Hall resistivity
ρ_o	Normal Hall resistivity
ρ_{AH}	Anomalous Hall resistivity
ρ_{xx}	Longitudinal resistivity
ρ_c	Critical concentration
R_o	Ordinary Hall coefficients
R_S	Anomalous Hall coefficients
M_r	Remanent magnetization
S	Magnetic spin moment
x	Magnetic impurity composition
n_i	Magnetic impurity concentration
I_{RKKY}	Total RKKY exchange integral
m^*	Effective hole mass
k_F	Fermi wave vector
v_n or v	Number of equivalent energy valley
p_o	Carrier concentration
J_{pd}	Exchange integral between holes and magnetic impurity ions
R_{ij}	Distance between magnetic ion site i and j,
z_{ij}	Number of nearest neighbours
λ	Mean free paths of the carriers
$F(2k_F R_{ij})$	Oscillatory spatial function
H_C	Coercive field
H_E	Exchange bias field
H_{FC}	Applied cooling field
μ	Carrier mobility
E_F	Fermi level
L_Φ	Phase coherent length
J_{se}	Superexchange interaction
τ_e	Elastic scattering time
τ_{ie}	Inelastic scattering time
τ_{SO}	Spin orbit scattering time

LIST OF PUBLICATIONS

RELEVANT JOURNAL PAPERS ON Ge$_{1-x}$Mn$_x$Te

1. S. T. Lim, Lu Hui, J. F. Bi, T. Liew and K. L. Teo, *Exchange bias effect of Ge$_{1-x}$Mn$_x$Te with antiferromagnetic MnTe and MnO materials*, J. Appl. Phys. **111**, 07C308 (2012).

2. S. T. Lim, Lu Hui, J. F. Bi, T. Liew and K. L. Teo, *Weak localization and antilocalization of hole carriers in degenerate p-Ge$_{1-x}$Mn$_x$Te*, J. Appl. Phys. **110**, 113916 (2011).

3. S. T. Lim, J. F. Bi, Lu Hui and K. L. Teo, *Exchange interaction and Curie temperature in Ge$_{1-x}$Mn$_x$Te ferromagnetic semiconductors*, J. Appl. Phys. **110**, 023905 (2011).

4. S. T. Lim, J. F. Bi, K. L. Teo, T. Liew and T. C. Chong, *Magnetism and Magnetotransport studies in Ge$_{1-x}$Mn$_x$Te*, J. Appl. Phys. **109**, 07C314 (2011).

5. S. T. Lim, J. F. Bi, K. L. Teo, Y. P. Feng, T. Liew and T. C. Chong, *Effect of hydrostatic pressure in degenerate Ge$_{1-x}$Mn$_x$Te*, Appl. Phys. Lett. **95**, 072510 (2009).

6. S. T. Lim, C. H. Sim, W. Q. Chen, J. F. Bi, K. L. Teo, T. Liew and T. C. Chong, *Temperature dependent magneto-transport studies in ferromagnetic Ge$_{1-x}$Mn$_x$Te with high Mn composition*, Int. J. Mod. Phys. B **23**, 3591 (2009).

7. W. Q. Chen, S. T. Lim, C. H. Sim, J. F. Bi , K. L. Teo, T. Liew and T. C. Chong, *Optical, Magnetic and Transport behaviours of Ge$_{1-x}$Mn$_x$Te ferromagnetic semiconductors grown by molecular-beam epitaxy*, J. Appl. Phys. **104**, 063912 (2008).

8. W. Q. Chen, S. T. Lim, K. L.Teo, M. B. A. Jalil, T. Liew and T. C. Chong, *Magnetic and transport behaviors in Ge$_{1-x}$Mn$_x$Te with high Mn composition*, Appl. Phys. Lett. **90,** 142514 (2007).

OTHER JOURNAL PAPERS ON ZnO

1. J. D. Ye, S. Pannirselvam, S. T. Lim, J. F. Bi, X. W. Sun, G. Q. Lo and K. L. Teo, *Two-dimensional electron gas in Zn-polar ZnMgO/ZnO heterostructure grown by metal-organic vapor phase epitaxy,* Appl. Phys. Lett. **97**, 111908 (2010).

2. S. T. Lim, W. D. Song, K. L. Teo, T. Liew and T. C. Chong, *The Gd concentration dependence of the magnetic properties of room temperature ferromagnetic ZnO:Gd semiconductor*, Int. J. Mod. Phys. B **23**, 3550 (2009).

CONFERENCE PRESENTATIONS

1. S. T. Lim, H. Lu, J. F. Bi, T. Liew and K. L. Teo, *Exchange bias effect of* $Ge_{1-x}Mn_xTe$ *with antiferromagnetic MnTe and MnO materials*, 56th Annual Conference on Magnetism and Magnetic Materials, Scottsdale, USA, Oct. 31 – Nov. 3 (2011).

2. S. T. Lim, J. F. Bi, K. L. Teo, T. Liew and T. C. Chong, *Magnetism and Magnetotransport studies in* $Ge_{1-x}Mn_xTe$, 55th Annual Conference on Magnetism and Magnetic Materials, Atlanta, USA, Nov. 14 – 18 (2010).

3. S. T. Lim, J. F. Bi, K. L. Teo, T. Liew, T. C. Chong, *Magneto-transport properties of diluted magnetic semiconductor* $Ge_{1-x}Mn_xTe$ *thin film,* Fifth International School and Conference on Spintronics and Quantum Information Technology, Cracow, Poland, Jul. 7 – 11 (2009).

4. S. T. Lim, W. D. Song, K. L. Teo, T. Liew, T. C. Chong, *The Gd concentration dependence of the magnetic properties of room temperature ferromagnetic ZnO: Gd semiconductor,* International Conference on Electronic Materials, Hilton Sydney, Sydney, Australia, Jul. 28 – Aug. 1 (2008).

5. S. T. Lim, C. H. Sim, W. Q. Chen, J. F. Bi, K. L. Teo, T. Liew, T. C. Chong, *Temperature dependent magneto-transport studies in ferromagnetic* $Ge_{1-x}Mn_xTe$ *with high Mn composition,* International Conference on Electronic Materials, Hilton Sydney, Sydney, Australia, Jul. 28 – Aug. 1 (2008).

AWARDS

1. Best Poster Award for IEEE Magnetics Society Singapore Chapter Poster Competition (2011)

2. Best Poster Presentation Award for DSI Graduating RS Poster Presentation (2010)

3. Best Oral Paper Award (IUMRS-ICEM 2008)

CHAPTER 1

1. INTRODUCTION

In the relentless effort to overcome the limits of miniaturization in conventional electronics devices, several new alternative concepts have been explored and investigated. One of which is spintronics, or spin-based electronics, where the spin degree of freedom of electrons or holes is being exploited, in addition to its charge. The harnessing of the spin property of carriers does not only lead to a new generation of spin-enabled devices which are non-volatile, possess higher data processing speed, with enhanced integration capabilities and lower power consumption but also offers prospects of merging electronics, photonics and magnetism into a single technology for multifunctional universal device [1,2].

The debut of spintronics was brought about by the discovery of giant magnetoresistive (GMR) effect in layered magnetic thin-film structures that are composed of alternating layers of ferromagnetic and nonmagnetic metal layers [3,4]. The GMR effect was first applied to hard disk drives read heads, which had significantly increased the storage density, and subsequently see applications in memory elements for magnetoresistive random access memory (MRAM) [5]. Alongside with metal-based spintronics, which utilize magnetic metals, semiconductor spintronics emerged as an attractive area of research due to its compatibility with conventional semiconductor technology. In addition to the ease of integration into existing electronics, semiconductor spintronics offer several desirable traits arising from the properties of semiconductors. They include the ability to regulate carrier concentrations by means of doping, allowing for optical or bandgap engineering, and a longer spin-coherent time of carriers as compared to metals [6]. These led to potential new spin-based devices such as spin field effect transistor (spin-FET) [7], spin light-emitting diode (spin-LED) [8,9], spin RTD (resonant tunnelling device) [10] and quantum bits for quantum computation [11].

The field of semiconductor spintronics can be broadly classified into two areas. One of which focuses on the study of spin related phenomenon, such as spin polarization, spin transport, spin manipulation and spin Hall effect, in conventional semiconductors [12,13,14,15,16,17]. While the other focus is on the study of ferromagnetism in ferromagnetic semiconductors (FMS), where semiconductors are being doped with other elements, typically transition metals, to exhibit magnetic properties [18]. The latter is the focus of this thesis. Among the various *p*-type FMS, $Ge_{1-x}Mn_xTe$ reveals relatively high Curie temperature (T_c) of 200 K [19]. This makes it a promising material for spintronic applications and warrants much research interests. Therefore this thesis focuses on the study of magnetic and transport properties of $Ge_{1-x}Mn_xTe$ thin films grown by molecular beam epitaxy (MBE).

1.1 Background

The beginning of spintronic research on magnetic semiconductors can be traced back to the 1960s, where the magnetism and semiconducting properties of europium chalcogenides and chromium spinels were being investigated [20]. However, these materials are not suitable for spintronic applications due to low T_c and the difficulties in fabricating good quality films [21]. Extensive studies of diluted magnetic semiconductor (DMS) started in 1970s, where Mn was used to grow II-VI Mn based alloys [22]. Comparing to the europium chalcogenides and chromium spinels, DMS exhibited smaller defects concentrations and were easily doped with shallow impurities.

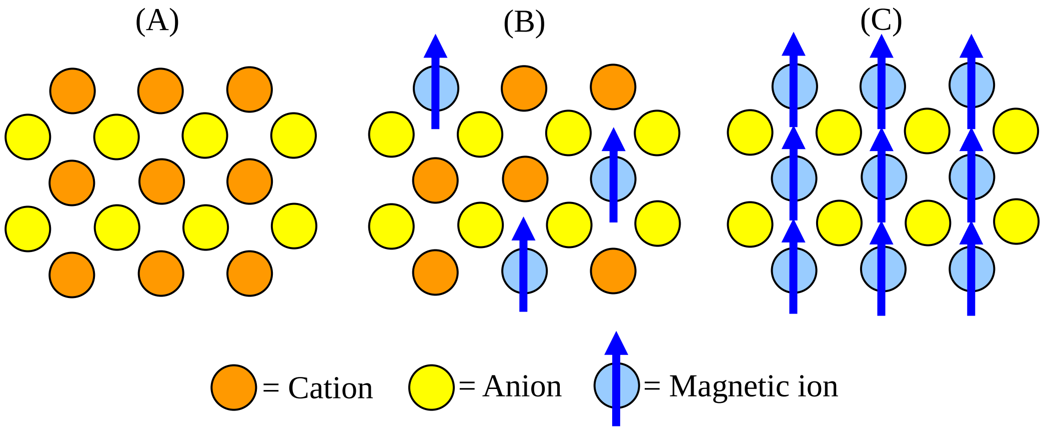

Figure 1.1 Three types of semiconductors: (A) a non-magnetic semiconductor, which contains no magnetic ions; (B) a diluted magnetic semiconductor, an alloy between nonmagnetic semiconductor and magnetic element; and (C) a magnetic semiconductor, in which a periodic array of magnetic element is present [23].

The family of DMS consist of standard non-magnetic smiconductors, in which a small amount of atoms, usually cations, are substituted by elements that produce localized magnetic moments in the semiconductor matrix [23] as shown in Figure 1.1.

Usually, the magnetic moments are originated from 3*d* or 4*f* open shells of transition metals (Sc, Ti, V, Cr, Mn, Fe, Co, Ni and Cu) or rare-earths elements (La, Eu, Gd and Er, etc.), respectively. Often the term DMS refers to the composition of the doped elements, while the term ferromagnetic semiconductor (FMS) is used to describe, in general, semiconductors that display ferromagnetic properties.

The study of FMSs and their heterostructures were then focused mostly on II-VI FMS, such as (Cd, Mn)Te and (Zn, Mn)Se [24], in which the valence of the cations matches that of Mn ions. Although this allows FMS to be easily prepared in bulk or thin film, the T_c in II-VI FMS is low as the magnetic interaction is dominated by the antiferromagnetic exchange among the Mn spins [25]. Subsequently, the research on FMS was extended towards materials containing elements other than Mn as well as to III-V [26] and IV-VI [27] compounds and group IV elemental semiconductors and various oxides [28]. Owing to the development of growth techniques which enable material synthesis under non-thermal equilibrium condition there were rapid progress in FMS research in the 1990s.

Several significant discoveries were reported since then [29]. One of them was the discovery of ferromagnetic $Ga_{1-x}Mn_xAs$ by Ohno *et al.* in 1996 [30] and with T_c of 110 K at ($x = 0.05$) [31]. This initiated tremendous interest in forging a better understanding in the ferromagnetic mechanisms underlying FMS. The *p-d* Zener model was proposed by

Dietl *et al*. in 2000 [32], according to which the ferromagnetism among the spins of isolated Mn atoms is mediated by hole carriers. Additionally, it predicted that T_c above room temperature can be achieved for *p*-type ZnO and GaN doped with 5% of Mn, as shown in Figure 1.2.

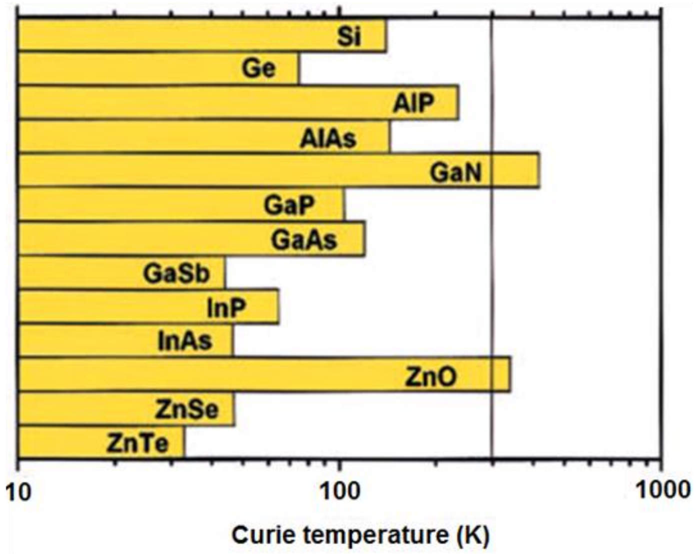

Figure 1.2 Computed values of the Curie temperature T_c for various *p*-type semiconductors containing 5 % of Mn and 3.5×10^{20} holes per cm^3. The line indicates T_c at room temperature [32].

The role of carriers in mediating ferromagnetism in FMS was verified experimentally in (In, Mn)As where its magnetic properties was tuned by changing the carrier density through external gating [33]. Following which, several discoveries in controlling of magnetism by various external means other than magnetic field were unravelled. They include electrical manipulation of coercive field [34] and magnetic anisotropy [35], current-induced domain-wall switching [36], light-induced ferromagnetic order [37], strain-induced reversal of magnetization easy axis [38], and even pressure-induced ferromagnetism [39]. These unique properties were not easily attainable in ferromagnetic metals.

These demonstrations further propelled the research in FMS, especially to attain room temperature ferromagnetism, for practical spintronic applications. As a consequence, numerous findings on high T_c FMS were reported, particularly in oxides and nitrides, such as (Ga, Mn)N [40], (Ga, Cr)N [41], (Ti, Co)O [42], (Zn, Co)O [43] and (Zn, Mn)O [44] to name a few. However, the results were mostly irreproducible and often due to spurious effects [45,46]. The origin of ferromagnetism in these materials remained elusive and generally attributed to embedded transition metal ions and defects. To date, the highest T_c attained for carrier mediated p-type Mn doped FMS is about 200 K for $Ga_{1-x}Mn_xAs$ [47,48] and $Ge_{1-x}Mn_xTe$ [19,49,50].

As the research in FMS progresses, it becomes clear that there is significant interest in the pursuit of T_c well above room temperature, and moving towards spin transport devices and possible technologies that might emerge. Fundamentally the spin-dependent phenomena and its physics remain intriguing and it is a hot research topic in the field of condense matter physics [51].

1.2 Motivation

Ferromagnetic semiconductors have attracted considerable attention due to their potential to bridge between functional semiconductors and ferromagnetic metals, thereby leveraging on the benefits of both material systems. This provides a scenario of having a fast, non-volatile universal memory logic device. The main advantage of having a spintronic device based on ferromagnetic semiconductor materials is its conductivity matching with conventional semiconductor used for logic devices, which is required for efficient spin injection. Thus in comparison with ferromagnetic metal materials, the spin injection efficiency is greatly reduced due to the large conductivity mismatch. This has to be overcome with the insertion of a Schottky barrier. Additionally, the magnetism in ferromagnetic semiconductor materials is mostly carrier mediated, which allows it to be manipulated by external means other than magnetic field, such voltage or electrical-field, current and light. This would be difficult to attain in ferromagnetic metal materials due to its high carrier concentration. Despite these advantages, the use of ferromagnetic semiconductor material in functional devices has been limited by its low T_c.

Over the last decade, much attention has been devoted to the research of III-V FMS $Ga_{1-x}Mn_xAs$ and it is widely accepted as a model to study FMS [46]. Notably, it has come close to realise practical application with a $T_c \sim 200$ K [47,48]. Recent progress in IV-VI FMS $Ge_{1-x}Mn_xTe$ grown by MBE shows that $T_c \sim 190$ K can be attained at Mn composition of $x \sim 0.1$ [49] and T_c as high as 200 K for $x \sim 0.55$ [50] and $x \sim 0.46$ can also be achieved under appropriate growth conditions [19]. This renders $Ge_{1-x}Mn_xTe$ a promising *p*-type FMS for spintronic applications in the infrared regime and warrants much research interest.

In contrast to the III-Mn-V FMS, the hole density and Mn ion concentration in $Ge_{1-x}Mn_xTe$ [52,53] can be controlled independently, as the incorporated Mn^{2+} is isoelectric to Ge. Moreover, the solubility limit of Mn in GeTe host lattice is large and reaches more than 95 % [52,54,55]. It is well known that crystalline GeTe is a narrow band-gap (0.1 to 0.2 eV) degenerate semiconductor with a high intrinsic hole carrier density (10^{20}-10^{21} cm^{-3}) due to native cation vacancies [56,57]. The ferromagnetism in $Ge_{1-x}Mn_xTe$ is then driven by the (Ruderman-Kittel-Kasuya-Yosida) RKKY indirect exchange interaction between Mn ions via this high hole concentration. Consequently, it is possible to control the carrier concentrations and hence the magnetic properties by changing the stoichiometric composition of GeTe and Te [58,59].

Comparing to II-Mn-VI and III-Mn-V FMS, IV-Mn-VI FMS such as $Ge_{1-x}Mn_xTe$ is far less explored. Ferromagnetic ordering with T_c up to 150 K was first observed in bulk $Ge_{1-x}Mn_xTe$ ($x = 0.5$), fabricated by annealing solid mixtures of GeTe and MnTe [60]. Subsequently, thin film $Ge_{1-x}Mn_xTe$ grown using ionized-cluster beam and radio frequency sputtering were reported to display T_c of 140 K ($x = 0.51$) [54,58] and 90 K (x

= 0.5) [53], respectively. MBE has only recently been employed to grow thin film $Ge_{1-x}Mn_xTe$ on BaF_2 substrates [19,49,50,52,61]. As also noted by Hassan *et al.* [19], the reported results on the magnetic properties, in particular the T_c have varied for similar Mn concentration, although most studies have found the highest T_c near $x = 50$ %. Therefore, it remains pertinent, from the growth point of view, to study the effects of various growth conditions, such as GeTe, Mn, Te fluxes and substrate temperatures on the structural and physical properties of $Ge_{1-x}Mn_xTe$.

The quality of the epilayers is highly dependent on the growth conditions. In $Ge_{1-x}Mn_xTe$, two different growth conditions with the same Mn concentration of 8% can lead to different magnetic properties and Curie temperatures [49]. The temperature dependence of magnetization (*M*-*T*) had showed one with concave and other with convex behaviour, which was suggested to have a short range and long range ferromagnetism, respectively. However, detailed experiments of its transport properties are still lacking. Therefore it is of interest to study the correlation between the magnetic and the transport properties in $Ge_{1-x}Mn_xTe$.

Another method to probe the Curie temperature (T_c) is via hydrostatic pressure experiments. Recent experiments on (In,Mn)Sb under hydrostatic pressure has clearly demonstrated an increase in carrier-mediated coupling , and thus an increase in its Curie temperature, as the lattice parameter is reduced by the applied pressure [62]. Tuning the exchange coupling by this process increases the magnetization, and also induces the ferromagnetic phase in an initially paramagnetic alloy. Thus the effect of pressure alters the magnetic properties of FMS and provides a better understanding of the physics governing the T_c of the material. On this basis, it is motivating to study the effects of hydrostatic pressure on $Ge_{1-x}Mn_xTe$ and thereby understand the interplay among factors that influences its T_c.

Magnetotransport studies of FMS have served as direct and convenient means of probing the electronic and magnetic properties of the material [63]. Magnetization is often manifested in the anomalous Hall term of the Hall resistivity which may arise from scattering processes involving spin-orbit coupling such as side-jump and skew scattering. [64] Although carrier mediated ferromagnetism [58,59] and anomalous Hall effect (AHE) [61] have been observed in $Ge_{1-x}Mn_xTe$, magnetotransport studies on this material have been limited.

Recent report by Lechner *et al.* [65] on MBE grown $Ge_{1-x}Mn_xTe$ has revealed exchange bias effects that are induced by phase separated antiferromagnetic (AFM) MnTe and ferromagnetic (FM) $Ge_{0.5}Mn_{0.5}Te$ phases. However it is difficult to reproduce the result as phase separation occurs randomly. In order to utilize the effect of exchange bias on possible spintronic application would require specific thin films of AFM and FM bilayer to be grown. Thus it is appealing to investigate the possible exchange bias effects that can be induced in AFM and $Ge_{1-x}Mn_xTe$ bilayer structures.

1.3 Objectives

The objectives of the research work described in this thesis can be listed as follows.

i) To study the effects of various growth conditions, such as GeTe, Mn, Te fluxes and substrate temperatures on the physical properties of $Ge_{1-x}Mn_xTe$ grown using MBE on BaF_2 and GaAs substrates and to optimize the growth conditions for a homogeneous FMS $Ge_{1-x}Mn_xTe$.

ii) To study the correlation between the magnetic and transport properties in $Ge_{1-x}Mn_xTe$.

iii) To investigate the effects of hydrostatic pressure on $Ge_{1-x}Mn_xTe$ and thereby to understand the interplay among factors that influences its T_c.

iv) To perform magnetoresistance studies on $Ge_{1-x}Mn_xTe$ to probe its electronic and magnetic properties.

v) To investigate the exchange bias effects of $Ge_{1-x}Mn_xTe$ with AFM MnTe and MnO materials.

1.4 Outlines of thesis

Chapter 1 provides a brief introduction on the background of FMS as well as its importance in the study of spintronics. The motivations and objectives in studying IV-VI FMS $Ge_{1-x}Mn_xTe$ are presented.

Chapter 2 provides a review on FMS, which includes the fundamentals and theoretical background relating to its ferromagnetism as well as summarizing the works on various types of FMS. Specifically, the research work done on $Ge_{1-x}Mn_xTe$ is also summarized.

Chapter 3 describes the molecular beam epitaxial growth technique and key characterization tools that were employed. The experimental setup and the principles behind them are briefly discussed.

Chapter 4 summarizes the effects of various growth conditions, such as GeTe, Mn, Te fluxes and substrate temperatures on the magnetic and structural properties of $Ge_{1-x}Mn_xTe$ grown using MBE on BaF_2 and GaAs substrates. Optimum growth conditions for single layer as well as for heterostructures of $Ge_{1-x}Mn_xTe$ are proposed.

Chapter 5 presents the results for the comparison between transport and magnetic properties in relation to the observation of two transition temperatures observed in $Ge_{0.9}Mn_{0.1}Te$.

Chapter 6 illustrates the enhancement of T_c in $Ge_{0.9}Mn_{0.1}Te$ with applied pressure. The results were analyzed within the framework of a two valence band and the RKKY models.

Chapter 7 shows that the T_c can also be suppressed under high applied pressure which is attributed to the increase in antiferromagnetic superexchange between Mn ions. The exchange integral between holes and Mn ions is found to correlate to the behaviour of the T_c with pressure.

Chapter 8 presents the magnetotransport studies of $Ge_{1-x}Mn_xTe$. The magnetoresistance is characterized by both positive and negative contributions, which can be described by the antilocalization and weak localization models, respectively.

Chapter 9 shows the exchange bias effect in GeMnTe heterostructures. The $Ge_{1-x}Mn_xTe$-MnTe system only leads to a modification of coercivity field, while a negative exchange bias shift in the hysteresis loop is observed for $Ge_{1-x}Mn_xTe$-MnO bilayer when it is cooled in applied field.

Chapter 10 gives the conclusion.

Chapter 1 References

[1] G. A. Prinz, *Magnetoelectronics*, Science **282**, 1660 (1998).

[2] S. A. Wolf, D. D. Awschalom, R. A. Buhrman *et al.*, *Spintronics: A Spin-Based Electronics Vision for the Future*, Science **294**, 1488 (2001).

[3] M. N. Baibich, J. M. Broto, A. Fert *et al.*, *Giant Magnetoresistance of (001)Fe/(001)Cr Magnetic Superlattices*, Phys. Rev. Lett. **61**, 2472 (1988).

[4] G. Binasch, P. Grünberg, F. Saurenbach *et al.*, *Enhanced magnetoresistance in layered magnetic structures with antiferromagnetic interlayer exchange*, Phys. Rev. B **39**, 4828 (1989).

[5] Y. Wu, *Nano Spintronics for Data Storage*, Encyclopedia for Nanoscience and Nanotechnology, American Scientific Publishers, USA. **7**, 493 (2003).

[6] J. M. Kikkawa, I. P. Smorchkova, N. Samarth *et al.*, *Room-Temperature Spin Memory in Two-Dimensional Electron Gases*, Science **277**, 1284 (1997)

[7] S. Datta and B. Das, *Electronic analog of the electro-optic modulator,* Appl. Phys. Lett. **56**, 665 (1990).

[8] R. Fiderling, M. Keim, G. Reuscher *et al.*, *Injection and detection of a spin-polarized current in a light-emitting diode*, Nature **402**, 787 (1999).

[9] Y. Ohno, D. K. Young, B. Beschoten *et al.*, *Electrical spin injection in a ferromagnetic semiconductor heterostructure,* Nature **402**, 790 (1999).

[10] P. Bruno, and J. Wunderlich, *Resonant tunneling spin valve: A novel magnetoelectronics device*, J. Appl. Phys. **84**, 978 (1998).

[11] D. Loss and D. P. DiVincenzo, *Quantum computation with quantum dots,* Phys. Rev. A **57**, 120 (1998).

[12] J. M. Kikkawa and D. D. Awschalom, *Lateral drag of spin coherence in gallium arsenide*, Nature **397**, 139(1999).

[13] G. Salis, Y. Kato, K. Ensslin *et al.*, *Electrical control of spin coherence in semiconductor nanostructures*, Nature **414**, 619 (2001).

[14] J. A. Gupta, R. Knobel, N. Samarth *et al.*, *Ultrafast Manipulation of Electron Spin Coherence,* Science **292**, 2458 (2001).

[15] Y. Kato, R. C. Myers, A. C. Gossard *et al.*, *Coherent spin manipulation without magnetic fields in strained semiconductors*, Nature **427**, 50 (2003).

[16] N. P. Stern, S. Ghosh, G. Xiang et al., *Current-Induced Polarization and the Spin Hall Effect at Room Temperature*, Phys. Rev. Lett. **97,** 126603 (2006).

[17] Saroj P. Dash, Sandeep Sharma, Ram S. Patel *et al.*, *Electrical creation of spin polarization in silicon at room temperature*, Nature **462**, 491 (2009).

[18] H. Ohno, *Making Nonmagnetic Semiconductors Ferromagnetic*, Science **281**,

951 (1998).

[19] M. Hassan, G. Springholz, R. T. Lechner *et al.*, *Molecular beam epitaxy of single phase GeMnTe with high ferromagnetic transition temperature*, J. Cryst. Growth **323**, 363 (2011).

[20] E. L. Nagaev, *Physics of Magnetic Semiconductors*, (Mir, Moscow, 1983) and references therein.

[21] A. Mauger and C. Godart, *The Magnetic, Optical, and Transport-Properties of Representatives of a Class of Magnetic Semiconductors-The Europium Chalcogenides*, Phys. Rep. **141,** 51 (1986).

[22] R. Gałazka, *Semimagnetic semiconductors*, In Proceedings 14th International Conference on Physics of Semiconductors, Edinburgh 1978, Wilson, B. (Ed.), IoP: Bristol, p. 133 (1978).

[23] H. Ohno, *Making Nonmagnetic Semiconductors Ferromagnetic*, Science **281**, 951 (1998).

[24] J. K. Furdyna and J. Kossut, Semiconductors and Semimetals, Vol. 25, eds. R.K. Willardson, A.C. Beer (Academic Press, New York, 1988).

[25] A. Haury, A. Wasiela, A. Arnoult, *et al.*, *Observation of a Ferromagnetic Transition Induced by Two-Dimensional Hole Gas in Modulation-Doped CdMnTe Quantum Wells*, Phys. Rev. Lett. **79**, 511 (1997).

[26] F. Matsukura, H. Ohno and T. Dietl, *Handbook of Magnetic Materials*, vol. 14, Ed. K.H.J. Buschow, p. 1-87, (Elsevier, Amsterdam 2002).

[27] G. Bauer, W. Pascher, W. Zawadzki, *Magneto-optical properties of semimagnetic lead chalcogenides*, Semicond. Sci. Technol. **7**, 703 (1992).

[28] W. Prellier, A. Fouchet and B. Mercey, *Oxide-diluted magnetic semiconductors: a review of the experimental status*, J. Phys.: Condens. Matter **15**, R1583 (2003).

[29] D. D. Awschalom and M. E. Flatté, *Challenges for semiconductor spintronics*, Nature Phys. **3**, 153 (2007).

[30] H. Ohno, A. Shen, F. Matsukura *et al.*, *(Ga,Mn)As: A new diluted magnetic semiconductor based on GaAs*, Appl. Phys. Lett. **69**, 363 (1996).

[31] F. Matsukura, H. Ohno, A. Shen *et al.*, *Transport properties and origin of ferromagnetism in (Ga,Mn)As*, Phys. Rev. B **57,** R2037 (1998).

[32] T. Dietl, H. Ohno, F. Matsukura *et al.*, *Zener model description of ferromagnetism in Zinc-Blende magnetic semiconductors*, Science **287**, 1019 (2000).

[33] H. Ohno, D. Chiba, F. Matsukura *et al.*, *Electric-field control of ferromagnetism*, Nature **408**, 944 (2000).

[34] D. Chiba, M. Yamanouchi, F. Matsukura *et al.*, *Electrical Manipulation of*

Magnetization Reversal in a Ferromagnetic Semiconductor, Science **301**, 943 (2003).

[35] D. Chiba, M. Sawicki, Y. Nishitani et al., *Magnetization vector manipulation by electric fields*, Nature **455**, 515 (2008).

[36] M. Yamanouchi, D. Chiba, F. Matsukura *et al.*, *Current-induced domain-wall switching in a ferromagnetic semiconductor structure*, Nature **428**, 539 (2004).

[37] S. Koshihara, A. Oiwa, M. Hirasawa *et al.*, *Ferromagnetic Order Induced by Photogenerated Carriers in Magnetic III-V Semiconductor Heterostructures of (In, Mn)As/GaSb*, Phys. Rev. Lett. **78**, 4617 (1997).

[38] A. Shen, H. Ohno, F. Matsukura *et al.*, *Epitaxy of (Ga, Mn)As, a new diluted magnetic semiconductor based on GaAs*, J. Cryst. Growth **175**, 1069 (1997).

[39] M. Csontos, G. Mihály, B. Jankó *et al.*, *Pressure-induced ferromagnetism in (In,Mn)Sb dilute magnetic semiconductor*, Nat. Mater. **6**, 447 (2005).

[40] M. L. Reed, N. A. El-Masry, H. H. Stadelmaier *et al.*, *Room temperature ferromagnetic properties of (Ga, Mn)N*, Appl. Phys. Lett., **79**, 3473 (2001).

[41] S. E. Park, H. J. Lee, Y. C. Cho *et al.*, *Room-temperature ferromagnetism in Cr-doped GaN single crystals*, Appl. Phys. Lett., **80**, 4187 (2002).

[42] Y. Matsumoto, M. Murakami, T. Shono *et al.*, *Room-temperature ferromagnetism in transparent transition metal-doped titanium dioxide*, Science **291**, 854 (2001).

[43] K. Ueda, H. Tabata, and T. Kawai, *Magnetic and electric properties of transition-metal-doped ZnO films*, Appl. Phys. Lett. **79**, 988 (2001).

[44] S. W. Jung, S. J. An, G. C. Yi *et al.*, *Ferromagnetic properties of* $Zn_{1-x}Mn_xO$ *epitaxial thin films*, Appl. Phys. Lett. **80**, 4561 (2002).

[45] Interview with S. Chambers, *Is it really intrinsic ferromagnetism?*, Nature Mater. **9**, 956 (2010).

[46] T. Dietl, *A ten-year perspective on dilute magnetic semiconductors and oxides*, Nature Mater. **9**, 965 (2010).

[47] L. Chen, S. Yan, P. F. Xu *et al.*, *Low-temperature magnetotransport behaviors of heavily Mn-doped (Ga, Mn)As films with high ferromagnetic transition temperature*, Appl. Phys. Lett. **95**, 182505 (2009).

[48] L. Chen, X. Yang, F. Yang *et al.*, *Enhancing the Curie Temperature of Ferromagnetic Semiconducto (Ga, Mn)As to 200 K via Nanostructure Engineering*, Nano Lett. **11**, 2584 (2011).

[49] Y. Fukuma, H. Asada, S. Miyawaki *et al.*, *Carrier-induced ferromagnetism in* $Ge_{0.92}Mn_{0.08}Te$ *epilayers with a Curie temperature up to 190 K*, Appl. Phys. Lett. **93**, 252502 (2008).

[50] W. Q. Chen, S. T. Lim, C. H. Sim *et al.*, *Optical, magnetic, and transport behaviors of* $Ge_{1-x}Mn_xTe$ *ferromagnetic semiconductors grown by molecular-beam epitaxy*, J. Appl. Phys. **104**, 063912 (2008).

[51] H. Ohno, *A window on the future of spintronics*, Nature Mater. **9**, 952 (2010).

[52] W. Q. Chen, K. L. Teo, M. B. A. Jalil *et al.*, *Compositional dependencies of ferromagnetic* $Ge_{1-x}Mn_xTe$ *grown by solid-source molecular-beam epitaxy*, J. Appl. Phys. **99**, 08D515 (2006).

[53] Y. Fukuma, H. Asada, N. Nishimura *et al.*, *Ferromagnetic properties of IV-VI diluted magnetic semiconductor* $Ge_{1-x}Mn_xTe$ *films prepared by radio frequency sputtering*, J. Appl. Phys. **93**, 4034 (2003).

[54] Y. Fukuma, T. Murakami, H. Asada *et al.*, *Film growth of* $Ge_{1-x}Mn_xTe$ *using ionized-cluster beam technique*, Physica E **10,** 273 (2001).

[55] W. Q. Chen, K. L. Teo, S. T. Lim *et al.*, *Magnetic and transport behaviors in* $Ge_{1-x}Mn_xTe$ *with high Mn composition*, Appl. Phys. Lett. **90**, 142514 (2007).

[56] R. Tsu, W. E. Howard, and L. Esaki, *Optical and Electrical Properties and Band Structure of GeTe and SnTe*, Phys. Rev. **172**, 779 (1968).

[57] S. K. Bahl and K. L. Chopra, *Amorphous versus Crystalline GeTe Films. III. Electrical Properties and Band Structure*, J. Appl. Phys. **41**, 2196 (1970).

[58] Y. Fukuma, M. Arifuku, H. Asada *et al.*, *Correlation between magnetic properties and carrier concentration in GeMnTe*, J. Appl. Phys. **91**, 7502 (2002).

[59] Y. Fukuma, H.Asada, M. arifuku *et al.*, *Carrier-induced ferromagnetism in* $Ge_{1-x}Mn_xTe$, Appl. Phys. Lett. **80,** 1013 (2002).

[60] R. W. Cochrane, M. Plischke and J. O. Ström-olsen, *Magnetization studies of* $(GeTe)_{1-x}(MnTe)_x$ *pseudobinary alloys*, Phys. Rev. B, **9** 3013 (1974).

[61] Y. Fukuma, K. Goto, S. Senba *et al.*, *IV-VI diluted magnetic semiconductor* $Ge_{1-x}Mn_xTe$ *epilayer grown by molecular beam epitaxy*, J. Appl. Phys. **103**, 053904 (2008).

[62] M. Csontos, G. Mihály, B. Jankó *et al.*, *Pressure-induced ferromagnetism in (In,Mn)Sb dilute magnetic semiconductor*, Nat. Mater. **4**, 447 (2005).

[63] T. Dietl, *Interplay between Carrier Localization and Magnetism in Diluted Magnetic and Ferromagnetic Semiconductors*, J. Phys. Soc. Jpn. **77**, 031005 (2008).

[64] A. Crépieux, and P. Bruno, *Theory of the anomalous Hall effect from the Kubo formula and the Dirac equation*, Phys. Rev. B **64**, 014416 (2001).

[65] R. T. Lechner, G. Springholz, M. Hassan *et al.*, *Phase separation and exchange biasing in the ferromagnetic IV-VI semiconductor* $Ge_{1-x}Mn_xTe$, Appl. Phys. Lett. **97**, 023101 (2010).

CHAPTER 2

2. REVIEW OF FERROMAGNETIC SEMICONDUCTORS

The last decade has seen tremendous progress in ferromagnetic semiconductor (FMS). A great deal of effort has been directed into the investigation of the mechanisms behind the ferromagnetism of FMS, in an attempt to find ways to increase the T_c above room temperature so as to be used in practical applications. Nevertheless, the ferromagnetism in FMS has already played important role in exploring new physics and concepts in spintronics [1]. This chapter provides an overview of the theory and models that have been used to explain the origin of ferromagnetism in FMS and some of its transport behaviours. Finally, a brief review of various types of FMS materials, including $Ge_{1-x}Mn_xTe$ will be given.

2.1 Theory and Origin of Ferromagnetism in FMS

It is well known that the magnetism exhibit by matters is originated from the magnetic moment of electrons which are either itinerant or localized. Some reviews on the fundamentals of magnetism in solids can be found in Ref. [2,3]. A nonvanishing magnetic moment is realized only in the case of partially filled shell. Typical examples are transition-metal ions and rare-earth ions, in which the 3*d* and 4*f* shells are incompletely filled, respectively. These ions are incorporated into semiconductors to exude a net magnetic moment, in the absence of an external magnetic field, below a critical temperature. Often, magnetic moments are not free but interact with each other and with their surroundings. The magnetic ordering in FMS is notably due to the exchange interactions between localized spins of the magnetic ions and band carriers [4]. The exchange interaction is of quantum mechanical origin and arises from Coulomb interaction. It can be inferred as the relative orientation of the magnetic moments to minimize the total energy of the system. Several models are proposed to account for the magnetic properties in FMS and have been discussed in detail in a number of reviews [5,6,7,8,9].

2.1.1 Potential and kinetic exchange interactions

Two electronic subsystems can be distinguished from the band structure of FMS. One comprising of delocalized band electrons arise primarily from outer *s*- and *p*-orbital of host atoms and the other consisting of the magnetic impurity electrons with magnetic moments in the ionic open 3*d* (or 4*f*) shell. While the effective-mass carriers from valence and conduction bands determine the electrical and optical properties, the localized magnetic moments are responsible for the magnetic properties of FMS. The spin dependent *sp*-*d*(*f*) exchange interactions between these two subsystems can be attributed to the direct Coulomb potential exchange and the hybridization-mediated kinetic exchange mechanism.

The direct Coulomb potential exchange is a first-order perturbation effect and the original spin-dependent Kondo Hamiltonian is of the form:

$$\hat{H}_{ex} = -2\sum_{k,k'} J_{kk'} e^{i\left(\vec{k}'-\vec{k}\right)\vec{R}} \hat{\vec{s}}_L \cdot \hat{\vec{s}}_{kk'} \tag{2.1}$$

Where $J_{kk'}$ is the exchange constant, $\hat{\vec{s}}_L$ and $\hat{\vec{s}}_{kk'}$ are the spin operator of the state L of the impurity at position R and the spin operator for the band electrons, respectively. Essentially, the exchange is governs by the Pauli Exclusion Principle which precludes two electrons having the same spin to appear concurrently at the same location. Consequently a parallel spin alignment is favourable as the magnitude of the Coulomb potential energy is lower compared to two electrons with antiparallel spins. Thus the direct Coulomb exchange potential leads to ferromagnetic Kondo Hamiltonian [10] and accounts for the Hund's rule, intra-atomic *s*-*d* exchange interaction and exchange interactions between spins of carriers within the same band [8].

On the other hand, the hybridization-mediated kinetic exchange which originates from the mixing of *s*,*p*-band states with the localized *d*(*f*) states, usually leads to an antiferromagnetic interaction between the spin pair [11,12]. This is because the quantum hopping of electrons, with an orientation matching to a relevant empty level, lowers the electron kinetic energy. Thus for FMS containing transition metals with singly occupied *d*-orbital, the transition of a band electron would be one with an opposite spin configuration.

The establishment of long range spatial ordering of the spin polarizations depends on whether the *d* electrons remain localized on the magnetic ions or contribute to the Fermi volume. In the former case, usually occurs in insulators or intrinsic semiconductors, and in the absence of carriers, the spins of magnetic ions are coupled via the superexchange or the double exchange mechanism. While in the latter case, typically arises in metals or extrinsic semiconductors, where *s*- or *p*-band itinerant carriers mediate the spin coupling between magnetic ions via the Rudeman-Kittel-Kasuya-Yosida (RKKY) or the *sp*-*d* Zener mechanism. Finally, it is noteworthy to mention the role of precipitation and spinodal decomposition in FMS, arising from the low solubility of transition metals in tetrahedral coordinated semiconductors, which leads to the observation of high T_c in FMS. All these mechanisms will be briefly described in the subsequent sections.

2.1.2 Superexchange

The superexchange is a mechanism in which the spins of two ions are correlated due to the aforementioned hybridization-mediated kinetic exchange interaction between each of the two ions and the valence *p*-band. The energy associated with the delocalization of the p electrons on the two ions depends strongly on the relative orientation of the spins of the two d electrons. A minimum total energy of the system is usually attained for an antiferromagnetic arrangement of neighbouring localized spins and the sign of the exchange interaction is negative. Thus superexchange mechanism occurs in magnetic dopants with singly occupied hybridized d-orbital (t_{2g}) such as Mn^{2+}, Fe^{2+}, and Co^{2+} ions, are found to be antiferromagnetic. This leads to the suppression of ferromagnetism in most Mn doped FMS [9], including $Ge_{1-x}Mn_xTe$ [13,14], when the Mn concentration is high. Figure 2.1 shows the antiferromagnetic superexchange interaction when Mn ions are coupled to Te ions.

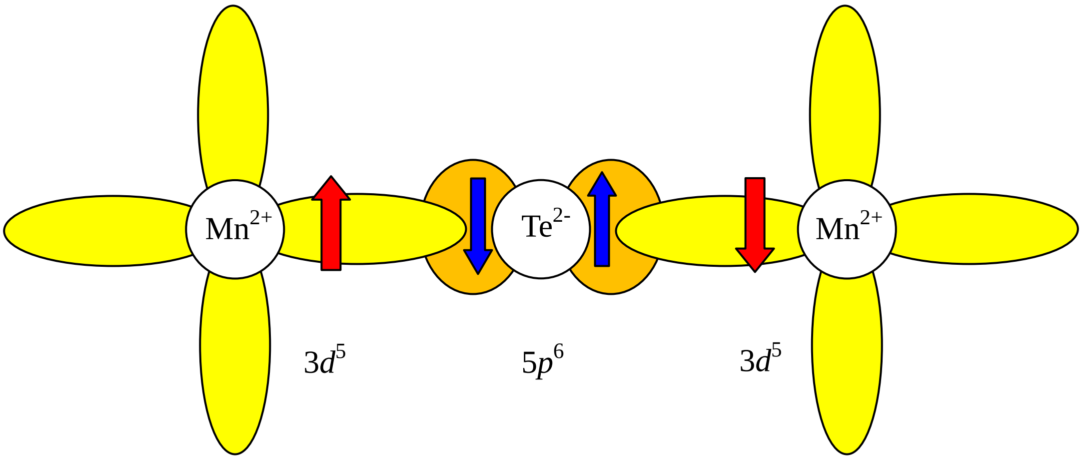

Figure 2.1 Antiferromagnetic superexchange interaction in MnTe.

However, the value and sign of the superexchange interaction also depends on the types of d-orbital and the number of electrons involved. A weakly ferromagnetic superexchange is observed for Cr based II-VI FMS [15,16]. Additionally, in europium chalcogenides and chromium spinels the superexchange is ferromagnetic, albeit a low T_c.

In the case of rock-salt Eu compounds, a competition between antiferromagnetic cation-anion-cation and ferromagnetic cation-cation superexchange (*s*-*f* coupling) is apparent [17].

2.1.3 Double exchange

The double exchange is a mechanism which occurs when the isolated magnetic ions acquire different charge states [18]. The spin coupling between these magnetic ions is by the virtual hopping of the additional electron from one ion to the other through interactions with the *p*-orbital. This mechanism always favours a ferromagnetic spin configuration because it facilitates the hopping of the electron which reduces of the kinetic energy of the addition electron resulting from the delocalization associated with the hybridization. Figure 2.2 shows the ferromagnetic alignment of the Mn ions due to the double exchange interaction.

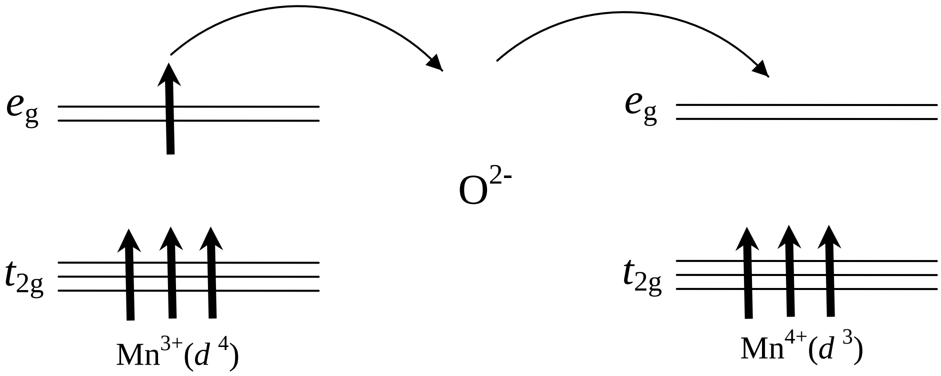

Figure 2.2 Double exchange interaction favors hopping via an anion (O^{2-}) for ferromagnetic alignment of the Mn ions by reducing kinetic energy.

The energy gain due to the double exchange comes from the band broadening of the partially occupied impurity band. It was successful in interpreting the origin of ferromagnetism in manganites of perovskite structure, such as $La_{1-x}Sr_xMnO_3$, where both Mn^{3+} and Mn^{4+} ions coexist [19]. In general, it is effective when half of the magnetic impurity and for one spin state is occupied and does not apply to d^0, d^5, d^{10} spin configurations. Double exchange is also found to be dominant in the wide band gap semiconductors II-VI and II-V based FMS [20,21], such as $Zn_{1-x}Co_xO$, $Ga_{1-x}Mn_xN$, $Ga_{1-x}Cr_xN$ and $Zn_{1-x}Cr_xTe$, from first principle calculations. This is apparently due to the short range ferromagnetic interaction originated from a partially occupied deep 3*d* impurity band.

2.1.4 RKKY Model

The Rudeman-Kittel-Kasuya-Yosida (RKKY) model was originally introduced to explain the interactions between nuclear spins in metal via the conduction electrons [22]. Thus, it is only suitable for describing the spin interaction between magnetic ions in FMS material which possesses high concentration of free carriers (~10^{20} cm^{-3}) and also in degenerate semiconductors [5]. The RKKY interaction involves ions interacting with the band electrons due to the Coulomb exchange described by Eq. (2.1). In the presence of a spin-polarized impurity ion, the spin-up and spin-down electrons experience a different potential and are scattered accordingly. Consequently, the superposition of the two spin carrier densities results in an oscillatory spin function which decays with the distance relative to the magnetic impurity ion.

The carrier mediated ferromagnetism in IV-VI FMS [23], such as $Pb_{1-x-y}Sn_yMn_xTe$ [24] and $Ge_{1-x}Mn_xTe$ [25], can be attributed to the RKKY mechanism due to the sufficiently high carrier concentrations (10^{20} – 10^{21} cm^{-3}). Within the framework of RKKY model, the Curie temperature for a randomly diluted magnetic system can be expressed as

$$T_C = \frac{2xS(S+1)}{3k_B} I_{RKKY} \tag{2.2}$$

where S is the spin magnetic moment of the magnetic impurities ($S = \frac{5}{2}$ for Mn^{2+}), k_B is the Boltzmann constant, x is the magnetic impurity composition and I_{RKKY} is the total RKKY exchange integral which is the sum contributions from magnetic ions interacting with free hole carriers from the valence bands. Thus, the total RKKY exchange integral, depending on the valence bands, n, involved, can be expressed as

$$\begin{aligned} I_{RKKY} &= \sum_n v_n I_n \\ &= \sum_n v_n \left[\left(m^*\right) \left(\frac{a_o^2}{2^9 \pi^3 \hbar^2} \right) \left(2k_F a_o\right)^4 \right] J_{pd}^2 \sum_{ij} z_{ij} F\left(2k_F R_{ij}\right) e^{-R_{ij}/\lambda} \end{aligned} \tag{2.3}$$

where m^* is the effective hole mass, a_o is the lattice constant, $k_F = \left(\frac{3\pi^2 p_o}{v_n} \right)^{1/3}$ is Fermi wave vector per one valley for a spherical Fermi surface with the number of equivalent energy valleys, v_n, and p_o is the carrier concentration, J_{pd} is the exchange integral between holes and magnetic impurity ions, $R_{ij} = a_o\sqrt{\frac{i}{2}}$ is the distance between magnetic ion site i and j, z_{ij} is the number of nearest neighbors in the R_{ij} range, λ is the mean free paths of the carriers and $F(2k_F R_{ij})$ is the oscillatory spatial function:

$$F(2k_F R_{ij}) = \left[\frac{\sin 2k_F R_{ij} - 2k_F R_{ij}\cos 2k_F R_{ij}}{(2k_F R_{ij})^4}\right] \tag{2.4}$$

Therefore, it is able to provide quantitative estimation of the T_c in heavily doped FMS. Additionally, the RKKY theory has been used to account for ferromagnetism in high p doped II-VI FMS [26,27], such as $Zn_{1-x}Mn_xTe$ and $Cd_{1-x}Mn_xTe$, and also for Mn based III-V FMS, where the Mn magnetic ions act as acceptors [28,29].

However, in most FMS, where the carrier densities are low and the mean ion-ion distance is small with respect to $1/k_F$ and the *p-d* Zener model has to be invoked to explain the observed properties of Mn based III-V and II-VI thin films [30].

2.1.5 Zener Model

The Zener model was initially proposed to describe the exchange coupling between band carriers and the localized spins that led to the ferromagnetism in transition metals [31]. This involves the spin splitting of the bands resulting from the spin polarization of the localized spins [32] as shown in Figure 2.3. The ferromagnetic ordering is driven by the lowering of the carriers' energy through the redistribution of the carriers between the spin sub-bands.

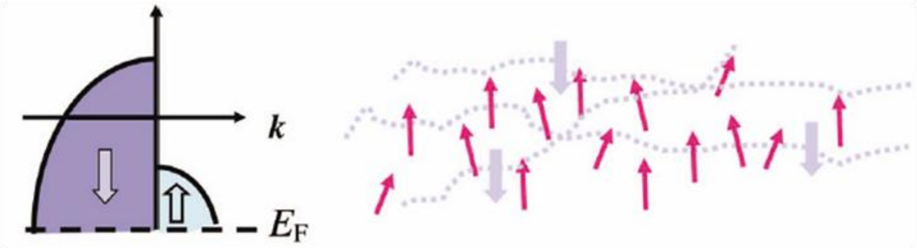

Figure 2.3 Representation of carrier-mediated ferromagnetism in *p*-type FMS. Owing to the *p*-*d* exchange interaction, ferromagnetic ordering of localized spins (red arrows) leads to spin splitting of the valence band [32].

However, Dietl *et al.* [30] show that the Zener model is insufficient to account for the ferromagnetic correlation between the distant magnetic spins, as the *d* electrons remain localized at the magnetic ion and do not contribute to charge transport. Instead, Dietl *et al.* proposed the *p*-*d* Zener model to describe the ferromagnetic interactions mediated by free carriers in tetrahedral coordinated semiconductors [30].

According to which, the holes in the extended or weakly localized states mediate the long range interactions between the localized spins on both side of the Anderson-Mott metal-insulator transition. Furthermore the holes transmit magnetic information efficiently between the localized impurity spins due to the large density of states in the valence band and strong spin-dependent *p*–*d* hybridization. The *p*-*d* Zener takes into account the carrier-carrier interaction, spin-orbit coupling and the k-p interaction, i.e. the mixing of the angular momentum basis states associated with the delocalization of atomic orbitals. Without taking these interactions into consideration, both the Zener and RKKY models are equivalent. This approach was found to be capable of adequately describing the magnitude of T_c and the magnetic anisotropy fields induced by biaxial strains in $Ga_{1-x}Mn_xAs$ and $Zn_{1-x}Mn_xTe$ [30]. It also suggested that *p*-type GaN and ZnO containing 5% of Mn and 3.5×10^{20} holes per cm^3 could support ferromagnetic ordering above room temperature, as shown in Figure 1.2.

Although the model has been effective in describing several experimental properties of FMS, especially for $Ga_{1-x}Mn_xAs$, it becomes inadequate for FMS with higher Mn concentration. As such there remain important issues of solubility limits, self compensation and interplay between disorder, localization and electron-electron correlations to be addressed experimentally as well as in theory.

2.1.6 Precipitation and Spinodal Decomposition

The theories considered so far assume a random but macroscopically uniform distribution of magnetic impurities, that is to say a homogeneous FMS. In this aspect, most optical, transport and magnetic properties of the band electrons in the FMS has been successfully interpreted within the virtual crystal and the mean field approximation [5,33]. The schematic diagrams of the two approximations and phase diagram for which the approximations are applicable are shown in Figure 2.4.

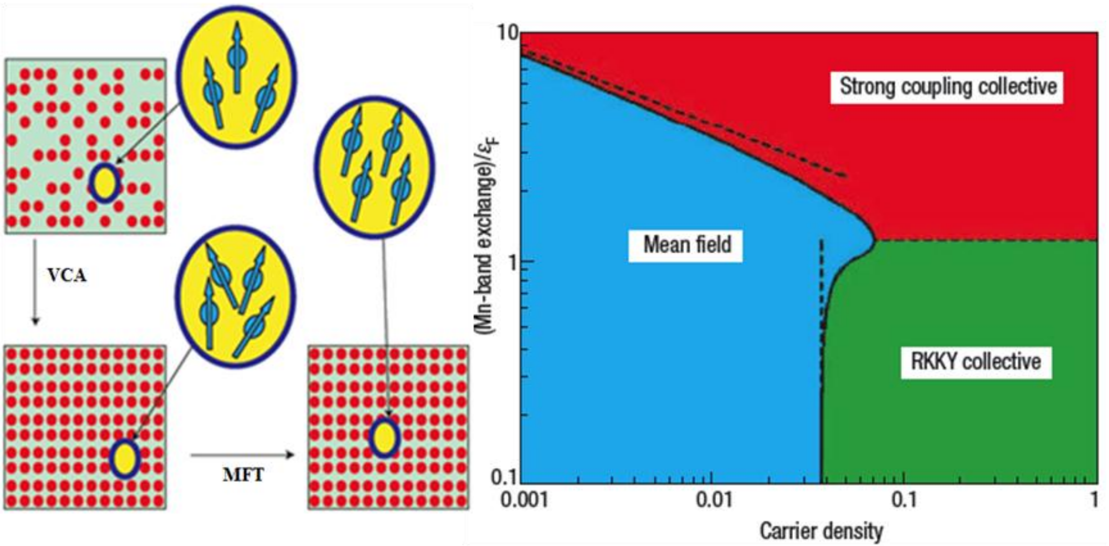

(a) (b)

Figure 2.4 (a) A schematic illustration of the virtual crystal and mean field approximations that are valid for systems with long-range coupling between Mn spins. (b) A schematic phase diagram for carrier-induced ferromagnetism in ferromagnetic semiconductors as a function of the exchange coupling strength relative to the band Fermi energy and the carrier concentration relative to the Mn concentration [33].

However, due to the solubility limit of magnetic constituent in a particular host at a given growth or thermal processing conditions the film may decompose into nanoregions with low and high concentrations of magnetic ions [6,7,8,34,35]. In particular, both hexagonal and zinc-blende Mn rich $Ga_{1-x}Mn_xAs$ nanocrystals are observed in annealed $Ga_{1-x}Mn_xAs$, and these correspond to precipitation of other secondary phases and spinodal decomposition, respectively [36,37]. As such, the occurrence of these nanocrystals renders the approximations invalid.

The experimental detection of these non-random spin distributions, coherent phases and possible contaminations has been highly challenging. Numerous elemental-specific nano-characterization techniques have been developed and employed simultaneously to discern these nanocrystals. These techniques include synchrotron X-ray diffraction, X-ray magnetic circular dichroism (XMCD) and transmission electron microscopy (TEM) with electron dispersive spectroscopy. For instance, the presence of coherent zinc-blende MnAs nanocrystals embedded in (Ga,Mn)As have been observed by TEM which attributes to the high Curie temperature [37]. Additionally, ferromagnetic precipitates of Fe_3N with Fe nanocrystals and hexagonal Mn-rich nanocrystal are detected in (Ga,Fe)N [38] and (Ga,Mn)N [39], respectively. Evidence of chemical phase separation is also found in (Zn,Cr)Te [40,41], (Al,Cr)N and (Ga,Cr)N [42]. Furthermore, under suitable growth conditions, nanocolumns are formed in GeMn [43], (Al,Cr)N [42] and (Zn,Cr)Te [44].

Owing to the high concentration of magnetic constituent detected in the nanocrystals, their spin ordering temperature is expected to be relatively high, even persisting above room temperature. Thus they account for the origin of the high temperature ferromagnetic response in FMS and diluted magnetic oxides, for which the average magnetic ions is below the percolation limit for the nearest neighbour coupling. And at the same time, the free carrier densities in these materials are too low to mediate an efficient long-range exchange interaction. In the case of oxides, the formation of magnetic impurities along extended defects such as dislocation and grain boundaries may also lead to the appearance of high T_c ferromagnetism. A more comprehensive discussions on the precipitation and spinodal decomposition in FMS and their *ab initio* and Monte Carlo modelling can be found in a number of reviews [7,8,9].

In the context of $Ge_{1-x}Mn_xTe$, other possible crystallographic phases that may occur at ambient temperature and pressure are listed in Table 2.1.

Table 2.1 A list of all the other possible crystallographic phases of $Ge_{1-x}Mn_xTe$.

Compounds	Structure	T_c / T_N	References
GeTe	Rhombohedral (Distorted Rock-salt) a = 5.9869 Å α = 88.27°	-	[45]
Mn	Cubic a = 8.868 Å (α)	T_N = 95 K	[46,47]
MnTe	Hexagonal NiAs-type a = 4.148 ± 0.001Å c = 6.711 ± 0.002Å	T_N = 310 K	[48,49]
	Zinc blende a = 6.33 Å	T_N = 65 K	[50,51]
Mn_5Ge_3	Hexagonal a = 7.184 Å c = 5.58 Å	T_c = 296 K	[52]
$Mn_{11}Ge_8$	Orthorhombic a = 13.20 Å b = 15.87 Å c = 5.087 Å	T_c = 274 K (T_N =150 K)	[53]

It can be observed that most of the phases lead to antiferromagnetic behaviour in $Ge_{1-x}Mn_xTe$, except for Mn_5Ge_3 and $Mn_{11}Ge_8$, which have relatively high T_c of 296 K and 274 K, respectively.

2.2 Magnetism and Magnetotransport related effects in FMS

As a consequence of the interaction between the localized impurity spin and itinerant band carriers, leading to the ferromagnetic ordering in FMS, several interesting transport behaviours have been observed in these materials. In the case when the FMS approaches the metallic side of the metal insulator transition (MIT), Kondo effect and weak localization becomes prominent. Nevertheless, the effect of spin-orbit coupling and strong Zeeman splitting effects, antilocalization can also contribute to the magnetotransport which displays a positive magnetoresistance. More importantly, FMS also exhibit anomalous Hall Effect behaviour where its magnetic property can be examined from its transport properties. Lastly, the exchange bias, the basis of which spins valves function, can also be observed in FMS materials when coupled with an antiferromagnetic material. These phenomenons will be discussed in this section.

2.2.1 Kondo Effect

A minimum in the resistivity-temperature curve of dilute magnetic alloys has been found in a number of alloys, including those of Cu, Ag, Au, Mg, Zn with Cr, Mn, Fe, Mo, Re, Os as impurities [54]. One of the explanations of this phenomenon is the Kondo effect, which can occur when metal is doped with magnetic impurities, whose spin states introduce an extra degree of freedom into the scattering problem.

The Kondo effect is due to the interaction between the spins of the conduction electrons and those of the localized impurities, which then provides a mechanism for inelastic scattering of the conduction electrons. It was found that the exchange interaction between the conduction and localized electrons is negative, which favors an antiparallel spins configuration [54,55,56]. The antiferromagnetic interaction leads to an electron scattering probability which increases below the Kondo temperature. This gives rise to the resistance minimum and also a logarithmic temperature dependence of resistivity at low temperature.

In $Ga_{1-x}Mn_xAs$, the resistance minimum at low temperature could be attributed to the Kondo effect [57 ,106]. This is due to the presence of antiferromagnetic superexchange between interstitial Mn (Mn_I) and those located at the Ga site (Mn_{Ga}) [57]. However, the low temperature transport behaviour in $Ga_{1-x}Mn_xAs$ can also be due to Mott variable-range hopping [106] and electron-electron interaction [58] for heavily Mn doped and metallic $Ga_{1-x}Mn_xAs$, respectively. Additionally, there can be competing effect from RKKY interaction [56] in FMS with high carrier density that favours ferromagnetic interactions between localized spins via the conduction electrons.

2.2.2 Anormalous Hall Effect

The anomalous Hall effect (AHE) has been useful in providing evidence of spin polarized current which is resulted from the interaction between carriers and localized magnetic moments [59,60,61,62,103]. It is adequate to verify carrier-mediated ferromagnetism in FMS but still fall short of proving intrinsic ferromagnetism in FMS [63] because clusters and secondary phases can interact with carriers as well. From the theoretical perspective, the standard approach to the AHE is based on the known models of side jump [64] and skew scattering [65] on impurities due to spin-orbit interaction. Nevertheless several mechanisms contributing to AHE have been proposed [66,67,68]. In FMS, the Hall resistivity (ρ_{xy}) can be described as the sum of normal Hall contribution (ρ_o) due to Lorentz force and anomalous Hall term (ρ_{AH}) that is proportional to the magnetization (*M*),

$$\rho_{xy} = \rho_o + \rho_{AH} = R_o H + R_s M$$

$$M \propto \frac{\rho_{xy} - R_o H}{\rho_{xx}{}^{n}} \tag{2.5}$$

where H is the magnetic field, ρ_{xx} is the longitudinal resistivity, n = 1 (for skew-scattering) and n = 2 (for side-jump), R_o and R_s are the ordinary and anomalous Hall coefficients, respectively. Thus the magnetization property can be obtained from the AHE and often use to verify with the magnetization results obtained from magnetometers. The R_o can be determined from the slope of ρ_{xy}, ($d\rho_{xy}/dH$) at high H region where the ordinary Hall effect dominates. Subsequently, the hole concentration, $p_o = 1/(R_o e)$ and mobility, $\mu = 1/(p_o \rho_{xx} e)$ can be calculated.

2.2.3 Weak-Localization and Antilocalization Effects

In addition to the Kondo effect, another effect which also leads to a minimum in the conductance minimum is the weak localization (WL) effect which is closely related to the time reversal symmetry [69]. This phenomenon is the consequence of interactions between a local spin and the spins of conduction electrons. It is known that WL occurs in disordered metallic systems at very low temperatures and it manifest itself as a quantum correction to the conductivity in metal or semiconductor [70,71]. Furthermore at temperature well below the conductance maximum it exhibits negative magnetoresistance (MR) in the absence of strong spin-orbit scattering.

The classical Drude-Boltzmann theory is valid in the limit $k_F \lambda >> 1$. As disorder increases, the $k_F \lambda$ value decreases and the system approaches the weak localized regime where quantum corrections start to affect the conductance value significantly. The WL theory was found to describe satisfactorily the MR display by a number of FMS [72] such as gated modulation-doped *n*-type (Cd, Mn)Te quantum wells [73], *n*-type (Cd, Mn)Se [74], *n*-type (Zn, Mn)O [75] and *p*-type (Ga, Mn)As, Also, for (Ga, Mn)As, the upturn of the resistance at low temperature was able to be explained in terms of quantum corrections to the conductivity in the weakly localized regime [76]. The theory of WL in ferromagnetic (Ga,Mn)As was discussed in Ref. [77] and signatures of WL were also observed in (Ga,Mn)As nanostructures [78].

In the presence of strong spin-orbit coupling and Zeeman splitting effects, antilocalization effect becomes apparent and leads to positive MR. This scenario was observed when Mg film was covered with a thin layer of strong spin-orbit coupler Au, that induced weak field positive MR in the initially negative MR displayed by Mg film [69]. Similarly, the presence of magnetic ions in FMS has led to the appearance of positive MR observed also for *n*-type (Cd, Mn)Se [74], (Cd, Mn)Te [73] and (Zn, Co)O [79] which is quantitatively described by the effect of field-induced giant spin splitting on disorder-modified electron-electron interactions. In IV-VI FMS, such as $Pb_{1-x}Eu_xTe$, it displays both antilocalization (positive MR) and localization (negative MR) behaviours depending on the type of carrier and Eu concentrations [80,81]. For *n*-type $Pb_{1-x}Eu_xTe$, only negative MR is observed at low temperatures due to partial reduction of electron-electron scattering by lattice screening and interference of self-crossing trajectories [80]. On the other hand, *p*-type $Pb_{1-x}Eu_xTe$ samples exhibit antilocalization effects due to the larger effective g factors in *p*-type samples when Eu magnetic ions are introduced [81]. Seemingly, the increase in disorder due to the inclusion of magnetic ions results in quantum-mechanical interference effects and renders the consideration of quantum corrections to conductivity important.

2.2.4 Exchange Bias Effect

Exchange bias (EB) is one of the phenomena associated with the exchange anisotropy created at the interface between an antiferromagnetic (AFM) and a ferromagnetic (FM) material. This anisotropy was discovered in 1956 by Meiklejohn and Bean when studying Co particles embedded in their native antiferromagnetic oxide (CoO) [82]. In most examples of EB, $T_B < T_N << T_c$, where T_B and T_N are the blocking temperature and Néel temperatures of the AFM layer, respectively and T_c is the Curie temperature of the FM layer [83]. When cooling with an applied field at $T > T_N$ through the T_N, the AFM spins are aligned to the FM spins and the coupling between them result in the EB effect. The manifestations of EB effect are notably the coercivity enhancement as well as shift in the hysteresis loop.

The study of EB effect between FMS and antiferromagnetic materials has attracted much attention as it provides a strong motivation for their integration into potential spintronic devices. In widely studied $Ga_{1-x}Mn_xAs$, proximity effects on the magnetic properties when interface with either MnTe or ZnMnSe have been studied [84]. However, only enhancement in coercivity has been observed in these samples. In the case of MnTe, the reasons were assigned to the soft magnetic anisotropy of the zinc-blende MnTe and a thick FM layer. According to the theoretical model proposed by Meiklejohn and Bean [85], the following condition should be satisfied for the observation of exchange anisotropy,

$$K_{AFM} t_{AFM} \geq J_{INT} \tag{2.6}$$

where K_{AFM} and t_{AFM} are the magnetic anisotropy and thickness of the AFM layer, respectively and $J_{INT} = H_E M_{FM} t_{FM}$ is the interface coupling constant determine by the product of exchange bias field (H_E), the saturation magnetization (M_{FM}) and the thickness (t_{FM}) of the FM layer. On the other hand, EB coupling was reported in $Ga_{1-x}Mn_xAs$ [86,87] and Cr doped GaN [88] by using an AFM MnO overlayer. In other FMS, such as ZnCoO when coupled to NiO, was able to observed vertical shift in the hysteresis loop as well [89]. Recently, EB effect was also observed in FM IV-VI $Ge_{1-x}Mn_xTe$ and it was attributed to the coexistence of FM $Ge_{1-x}Mn_xTe$ and AFM MnTe phases arising from phase separation [90].

2.3 Different Groups of FMS

Several material systems have been studied since the 1960s in an effort to combine semiconducting properties with a ferromagnetic ordering that persists above room temperature. This section provides a brief review of some commonly studied semiconductor compounds used to achieve this purpose. They include the widely studied group II-VI and III-V FMS, technologically important group IV FMS, narrow-gap IV-VI FMS and the much controversial wide-gap, oxide as well as non-transition metal FMS.

2.3.1 Group II-VI and III-V FMS

One of the earliest studied FMS is that of II-VI compounds. Owing to the matching between the valency of cations and that of Mn ions, they are relatively easy to prepare in bulk form or in thin epitaxial layers. Accordingly, Mn is an isoelectronic impurity in II-VI compounds and it is possible to control the spin and carrier density independently. However, at a given Mn and hole concentrations, the T_c is much lower in II-VI FMS than in III-V FMS, due to the destructive influence of the short-range antiferromagnetic superexchange. Typical II-VI FMS are those of CdTe, BeTe, ZnTe, ZnSe and ZnO doped with either Mn or Cr transition ions [91].

The theoretical prediction that the antiferromagnetic coupling can be overcompensated by ferromagnetic interactions mediated by the valence band holes [92] was verified by experimental studies of *p*-type modulation-doped (Cd, Mn)Te quantum wells [93,94] as well as of *p*-type (Zn, Mn)Te:N [95,96,97], (Zn, Mn)Te:P [96,97], and (Be,Mn)Te:N [97,98]. Furthermore, relatively high T_c of 100 K and even up to room temperature were observed in (Zn, Cr)Se [99] and (Zn, Cr)Te [100], respectively. However, the origin of the ferromagnetic ordering was attributed to precipitation and spinodal decomposition as discussed in Section 2.1.6. In the former case, the magnetic response was due to precipitates as the T_c does not scale with the Cr concentration and is close to the $ZnCr_2Se_4$. While, the latter, was due to nanoparticles of metallic zinc-blende CrTe or Cr-rich (Zn, Cr)Te characterized by $T_c \approx 320$ K [101,102].

The III-V FMS, especially $Ga_{1-x}Mn_xAs$ and $In_{1-x}Mn_xAs$, have been widely studied due to the application of III-V compound semiconductors in high-speed, photonic, microwave, and optoelectronic devices. In contrast to II-VI FMS, the Mn dopant acts as both an acceptor and a source of localized magnetic moments for carrier mediated ferromagnetism in III-V FMS. One of the significant breakthroughs in FMS was the discovery of relatively high T_c of 110 K in $Ga_{1-x}Mn_xAs$ ($x = 0.05$) grown using the MBE system [103]. In order to incorporate a large concentration of Mn in the GaAs lattice without forming inclusions of the thermodynamically more stable metallic MnAs phase, $Ga_{1-x}Mn_xAs$ must be grown by MBE at relatively low temperatures under a non-equilibrium condition. Yet, the solubility limit of Mn in GaAs remains low ($x < 0.1$).

On the other hand, the low growth temperature leads to a high density of point defects such as As anti-sites and Mn interstitials. These defects act as double donors, compensating the free holes carriers as well as Mn spins, owing to the antiferromagnetic coupling between interstitial and substitutional Mn pairs, and thus limits the T_c [104,105]. Moreover, there appears to be an upper limit for carrier density in GaAs. The attempt to increase the Mn or Be acceptor concentration in GaMnAs also resulted in MnAs precipitates and interstitial Mn [105]. The detrimental effects of interstitial Mn on ferromagnetism can be partly reduced by an annealing process that promotes the diffusion of the interstitial Mn ions to the surface [33]. As a result of the improvements in growth protocols and post-growth processes, that allow higher Mn and hole concentrations in $Ga_{1-x}Mn_xAs$, the T_c now approaches 190 K for thin film [106] and 200 K in nanostructures [107].

In general, the *p*-*d* Zener model was sufficient to describe the magnitudes of T_c and the magnetic anisotropy fields induced by biaxial strains in $Ga_{1-x}Mn_xAs$ [30]. Although, the T_c in III-V FMS is still low for practical applications, it has already played a significant role in exploring new physics and concepts in spintronics. Some examples include the electrical manipulation of magnetism [108], current-induced domain-wall switching [109] and illustration of spin-LED [110,111].

2.3.2 Group IV and Group IV-VI FMS

From a technological viewpoint, spin injection in group IV semiconductors such as Si and Ge would represent a milestone development [112,113] as this would allow integration of spintronics with the current industrial standard which is dominated by Si and SiO_2. In this aspect, group IV FMS would be an ideal source for the spin injection. Further motivation came from the theoretical prediction [30] that relatively high T_c can be achieved in 5% Mn doped Si and Ge (see Figure 1.2).

The first experimental observation of ferromagnetism in group IV FMS came from MBE-grown *p*-type Mn_xGe_{1-x} ($x = 0.033$) with $T_c = 116$ K [112]. Interestingly, similar observations have been reported by various groups but with different T_c values [114,115,116]. It was realized that Mn is not easily soluble in Ge and often result in various Mn-rich phases such as Mn_5Ge_3 ($T_c \sim 296$ K) and $Mn_{11}Ge_8$ ($T_c \sim 270$ K). Thus, the apparently conflicting observations can be attributed to the coexistence of these chemically inhomogeneous phases [117]. Apart from doping with Mn, ferromagnetism has also been observed in other transition metals doped Ge such as Cr ($T_c \sim 126$ K), Fe ($T_c \sim 233$ K and 350 K with Mn co-doping) and Co ($T_c \sim 270$ K with Mn co-doping). Ferromagnetic signatures have also been observed in Mn doped Si [118,119,120]. However, similar to the case of Mn_xGe_{1-x}, different T_c were reported ($T_c \sim 210$ K [118], $T_c > 400$ K [119]). Seemingly, the magnetic property of Mn_xSi_{1-x} is highly sensitive to preparation conditions and often phase separated manganese silicides nanocrystallites were observed [120]. Owing to the random occurrence of these phases, the magnetic and transport properties in these materials are not readily reproducible. However, the report on the formation of periodically arranged GeMn noncloumns under suitable growth conditions is encouraging [43].

Group IV-VI magnetic alloys and compounds have generated considerable interest largely due to the demonstration of carrier mediated ferromagnetism in

$Pb_{1\text{-}x\text{-}y}Sn_yMn_xTe$ [24]. Typical IV-VI FMS are those of PbTe, PbS, PbSe, SnTe and GeTe doped with either transition metal Mn or rare-earth metal Eu and Gd ions [23,24,121,122]. These are narrow gap semiconductors and usually acquire a rock-salt crystalline structure. The magnetism in these materials is mediated by carriers via the RKKY interactions [23,24]. As such the magnetic properties can be controlled by modifying the carrier concentration, which arises from the native defects, by adjusting their stoichiometric composition. However, similar to II-VI FMS, superexchange also limits the ferromagnetic ordering in IV-VI FMS [121]. In some of the earlier studied IV-VI FMS, such as $Pb_{1\text{-}x\text{-}y}Sn_yMn_xTe$, $Sn_{1\text{-}x}Mn_xTe$ and $Ge_{1\text{-}x}Mn_xTe$, the T_c reported were 4 K [123], 6 K [124] and 150 K [13], respectively. As such, owing to the relatively high T_c exhibited by $Ge_{1\text{-}x}Mn_xTe$, the recent focus has been on transition metal doped GeTe [125]. Among the transition metals doped GeTe investigated by Fukuma *et al.* [125], only those doped with Cr, Mn and Fe are ferromagnetic whereas others doped with Ti, V, Co and Ni are paramagnetic.

2.3.3 Wide-gap, Oxide and Non-transition metal FMS

Wide band gap and oxide based FMS, such as transition metal doped GaN and ZnO, have attracted considerable interest due to the theoretical prediction of T_c in excess of room temperature by Dietl *et al.* [30]. Numerous experimental observations of high T_c in these materials were reported. They include (Ga, Mn)N ($T_c \sim 370$ K) [126], (Ga, Cr)N ($T_c = 280$ K) [127], (Ti, Co)O ($T_c > 400$ K) [128], (Zn, Co)O ($T_c \sim 300$ K) [129] and (Zn, Mn)O ($T_c > 420$ K) [130]. However, the observed results are often conflicting and irreproducible. This discrepancy is likely due to different growth techniques and synthesis conditions which affects the mechanism of ferromagnetism in these materials. The origin of ferromagnetism in these materials is generally attributed to embedded transition-metal ions, chemical phase separations and defects [7]. From the theoretical aspect, efforts have been directed to simulate and model these effects. These theoretical studies often require the combination of mean-field approximation, the random phase approximation, Monte Carlo simulation with magnetic force theorem and first principle studies [9]. Some of these simulations are able to reproduce the experimental observed nanocrystals and estimate the T_c [131].

Interestingly, the theoretical studies also lead to the prediction of FMS materials without transition impurities, such as C or N doped CaO, MgO, SiO_2 and ZnO [9]. In these materials in which magnetism is induced by incorporating non-magnetic impurities, the substitutional ions may have a nonzero moment and the 2*p*-electrons of these ions, rather than the 3*d*-electrons, play an essential role in introducing magnetism in the host materials. The theoretical prediction was verified experimentally in C doped ZnO which showed ferromagnetism with Curie temperatures higher than 400 K [132].

This attracts considerable attention as issues pertaining to the presence of condense magnetic semiconductor or other magnetic phases can be disregarded. However, it is well known that oxide materials contain grain boundaries and intrinsic defects such as oxygen vacancies may also enhance ferromagnetism [133].

2.4 Review of $Ge_{1-x}Mn_xTe$

Magnetization studies of $(GeTe)_{1-x}(MnTe)_x$ pseudobinary alloys was first carried out by Cochrane *et al.* [13], for $0 < x < 0.5$, whose properties were explained using the RKKY theory. Although, the individual compounds of GeTe and MnTe are diamagnetic and antiferromagnetic, respectively, ferromagnetic ordering is observed in the alloy. The structure of the alloy can be rhombohedral, rock-salt, NiAs or mixture of both depending on the mole fraction of MnTe. The phase diagram of GeTe-MnTe system [134] is shown in Figure 2.5.

Further research in $Ge_{1-x}Mn_xTe$ was carried out by various groups in recent years. Several observations of the optical, magnetic, electrical and structural properties of $Ge_{1-x}Mn_xTe$ fabricated using several techniques, such as ionized-cluster beam [25,135,136], sputtering [14], and MBE [137,138,139,140,141,142], were reported. Similar to II-VI FMS, the incorporated Mn^{2+} is isoelectric to Ge and the hole carriers, which arise from native defects, can be independently controlled by varying the GeTe stoichiometry.

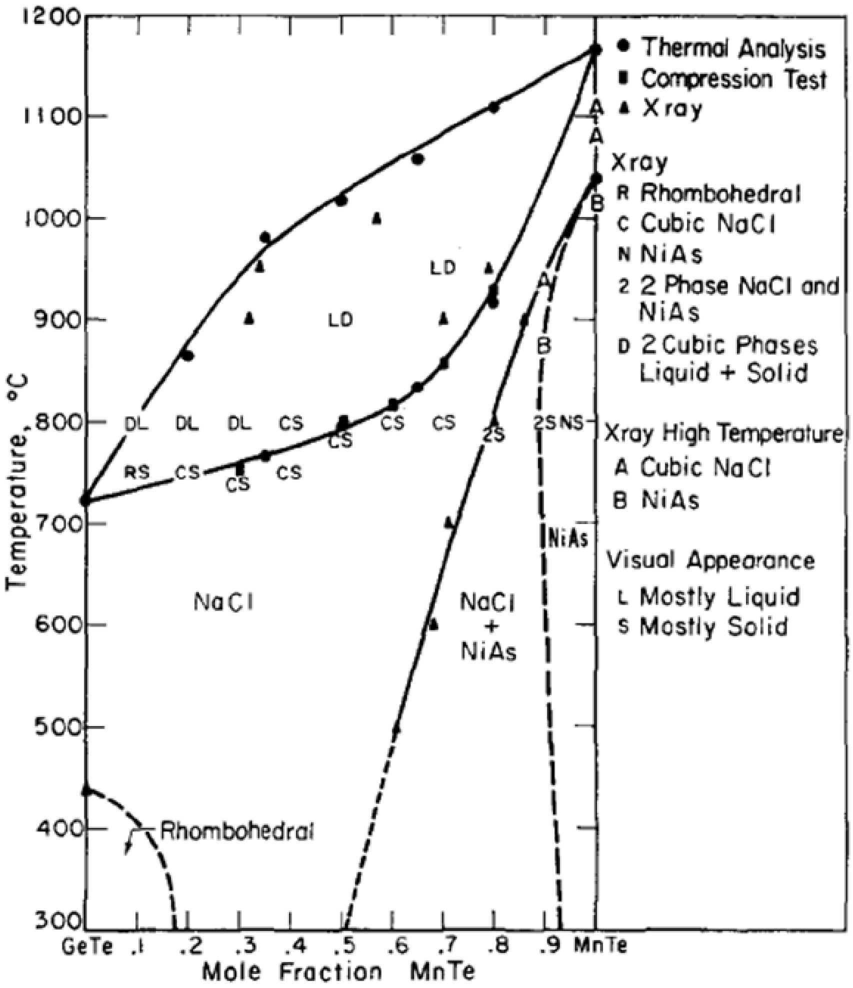

Figure 2.5 Phase diagram for GeTe-MnTe system [134].

The correlation between the carrier concentrations and the T_c was reported in Ref. [136,139] and it is consistent with the RKKY theory for high carrier concentration (~10^{20} cm^{-3}). Additionally, the Mn solubility in GeTe reaches more than 95 % and the maximum T_c is observed for x ~ 0.5 [137]. By incorporating Mn ions into the narrow gap GeTe, the lattice constant is found to decrease almost linearly with increasing Mn composition [135]. In contrast, a gradual increase in the bandgap is observed for higher Mn composition due to Burstein-Moss effect which shifts the absorption edge to higher energies as the states near the conduction band are being populated [141]. The local environment of Mn ions has been analysed using the X-ray absorption spectroscopy (XAS) and XMCD which suggest that the Mn 3*d* states are localized with divalent character and are responsible for the magnetism in $Ge_{1-x}Mn_xTe$ [143,144]. The theoretical studies of $Ge_{1-x}Mn_xTe$, by means of *ab initio* calculations are consistent with experimental results, verifying the localization of Mn 3*d* states deep in the valence band [145]. Furthermore, together with the density functional study the magnetization is found to increase monotonically with the number of holes created by Ge vacancy and the highest achieved at moderate Mn composition of $x \sim 0.5$ [146]. Interestingly, with a particular composition of $Ge_5Mn_2Te_8$, the ternary compound is predicted to be half metallic by Zhao *et al.* [147] using the full-potential density functional method.

Recent progress in IV-VI FMS $Ge_{1-x}Mn_xTe$ grown by MBE shows that $T_c \sim 190$ K can be attained at Mn composition of $x \sim 0.1$ [139] and T_c as high as 200 K at $x \sim 0.5$ can also be achieved under appropriate growth conditions [141,142]. Lastly, it was reported by Lechner *et al.* [90] that as the Mn content approaches $x = 0.5$, there is tendency for phase separation to occur at higher growth temperature to form hexagonal AFM MnTe and rhombohedral FM $Ge_{1-x}Mn_xTe$ phase resulting in magnetic exchange bias effects.

Chapter 2 References

[1] H. Ohno, *A window on the future of spintronics*, Nature Mater. **9**, 952 (2010).

[2] K. Yosida, *Theory of Magnetism*, (Springer, Berlin, 1996).

[3] E. Du Trémolet de Lacheisserie, D. Gignoux, M. Schlenker, *Magnetism: Fundamentals*, (Springer, France, 2002).

[4] M. Jaczyński, J. Kossut and R. R. Gałązka, *Influence of Exchange Interaction on the Quantum Transport Phenomena in* $Hg_{1-x}Mn_xTe$, Phys. Status Solidi b **88**, 73 (1978).

[5] P. Kacman, *Spin interactions in diluted magnetic semiconductors and magnetic semiconductor structures*, Semicond. Sci. Technol. **16**, R25 (2001).

[6] T. Dietl, in *Spintronics*, ed. T. Dietl, D. Awschalom, M. Kaminska and H. Ohno, Elsevier, Amsterdam, vol. **82** of *Semiconductors and Semimetals*, 371 (2008).

[7] T. Dietl, *A ten-year perspective on dilute magnetic semiconductors and oxides*, Nature Mater. **9**, 965 (2010).

[8] A. Bonanni and T. Dietl, *A story of high-temperature ferromagnetism in semiconductors*, Chem. Soc. Rev. **39**, 528 (2010).

[9] W. Chen and I. Buyanova (ed), *Handbook of Spintronic Semiconductors*, Pan Stanford Publishing, Singapore (2010).

[10] J. K. Furdyna and J. Kossut (ed), *Diluted Magnetic Semiconductors, Semiconductors and Semimetals*, vol. **25** (New York: Academic, 1988).

[11] T. Dietl, *Physics in High Magnetic Fields* (Springer Series in Solid-State Physics vol **24**) ed M. Miura (Berlin: Springer, 1981).

[12] A. K. Bhattacharjee, G. Fishman and B. Coqblin, *Virtual bound-state model for the exchange interaction in semimagnetic semiconductors such as Cd1-xMnxTe*, Physica B, C **117-8**, 449 (1983).

[13] R. W. Cochrane, M. Plischke and J. O. Ström-olsen, *Magnetization studies of* $(GeTe)_{1-x}(MnTe)_x$ *pseudobinary alloys*, Phys. Rev. B, **9** 3013 (1974).

[14] Y. Fukuma, H. Asada, N. Nishimura *et al.*, *Ferromagnetic properties of IV-VI diluted magnetic semiconductor Ge1-xMnxTe films prepared by radio frequency sputtering*, J. Appl. Phys. **93**, 4034 (2003).

[15] J. Blinowski, P. Kacman and J. A. Majewski, *Ferromagnetism in Cr-based diluted magnetic semiconductors*,J. Cryst. Growth **159**, 972 (1996).

[16] J. Blinowski, P. Kacman and J. A. Majewski, *Ferromagnetic superexchange in Cr-based diluted magnetic semiconductors*,Phys. Rev. B **53**, 9524 (1996).

[17] P. Wachter, in *Handbook on the Physics and Chemistry of Rare Earth*, ed. J. K. A. Gschneidner and L. Eyring, North-Holland, Amsterdam vol. **2**, 507 (1979).

[18] C. Zener, *Interaction between the d-Shells in the Transition Metals. II. Ferromagnetic Compounds of Manganese with Perovskite Structure***,** Phys. Rev., **82**, 403 (1951).

[19] P. -G. de Gennes, *Effects of Double Exchange in Magnetic Crystals*, Phys. Rev. **118**, 141 (1960).

[20] H. Akai, *Ferromagnetism and Its Stability in the Diluted Magnetic Semiconductor (In, Mn)As,* Phys. Rev. Lett. **81**, 3002 (1998).

[21] K. Sato and H. Katayama-Yoshida, *First principles materials design for semiconductor spintronics,* Semicond. Sci. Technol. **17**, 367 (2002).

[22] P. Mohn, *Magnetism in the Solid State* (Spriger, New York, 2003).

[23] T. Story, P. J. T. Eggenkarnp, C. H. W. Swiiste *et al.*, *Ruderman Kittel Kasuya Yosida exchange interaction in many-valley IV-VI semimagnetic semiconductors*, Phys. Rev. B **45**, 1660 (1992).

[24] T. Story, G. Karczewski, L. SWierkowski *et al.*, *Magnetism and band structure of the semimagnetic semiconductor Pb-Sn-Mn-T*e, Phys. Rev. B **42**, 10477 (1990).

[25] Y. Fukuma, H. Asada, M. Arifuku *et al.*, *Carrier-enhanced ferromagnetism in* $Ge_{1-x}Mn_xTe$, Appl. Phys. Lett. **80**, 1013 (2002).

[26] T. Dietl T, A. Haury A and Y. Merle d'Aubign´e, *Free carrier-induced ferromagnetism in structures of diluted magnetic semiconductors*, Phys. Rev. B **55**, R3347 (1997).

[27] J. Cibert, P. Kossacki, A. Haury *et al.*, *Ferromagnetic transition in II–VI semimagnetic QWs*, J. Cryst. Growth **201–2**, 670 (1999).

[28] T. Dietl, J. Cibert, D. Ferrand *et al.*, *Carrier-mediated ferromagnetic interactions in structures of magnetic semiconductors,* Mater. Sci. Eng. B **63**, 103 (1999).

[29] H. Ohno, *Properties of ferromagnetic III-V semiconductors*, J. Magn. Magn. Mater. **200**, 110 (1999).

[30] T. Dietl, H. Ohno, F. Matsukura *et al.*, *Zener model description of ferromagnetism in Zinc-Blende magnetic semiconductors*, Science **287**, 1019 (2000).

[31] C. Zener, *Interaction Between the d Shells in the Transition Metals*, Phys. Rev. **81**, 440 (1951).

[32] T. Dietl and H. Ohno, *Engineering magnetism in semiconductors*, Materials Today **9**, 18 (2006).

[33] A. H. Macdonald, P. Schiffer and N. Samarth, *Ferromagnetic semiconductors: moving beyond (Ga,Mn)As*, Nat.Mater. **4**, 195 (2005).

[34] B. W. Wessels, *Ferromagnetic semiconductors and the role of disorder*, New J. Phys. **10**, 055008 (2008).

[35] T. Dietl, *Origin and control of ferromagnetism in dilute magnetic semiconductors and oxides*, J. Appl. Phys. **103**, 07D111 (2008).

[36] M. Moreno, A. Trampert, B. Jenichen *et al.*, *Correlation of structure and magnetism in GaAs with embedded Mn(Ga)As magnetic nanoclusters*, J. Appl. Phys. **92**, 4672 (2002).

[37] M. Yokoyama, H. Yamaguchi, T. Ogawa *et al.*, *Zinc-blende-type MnAs nanoclusters embedded in GaAs*, J. Appl. Phys. **97**, 10D317 (2005).

[38] A. Bonanni, M. Kiecana, C. Simbrunner *et al.*, *Paramagnetic GaN:Fe and ferromagnetic (Ga,Fe)N: The relationship between structural, electronic, and magnetic properties*, Phys. Rev. B **75**, 125210 (2007).

[39] G. Martinez–Criado, A. Somogyi, S. Ramos *et al.*, *Mn-rich clusters in GaN: Hexagonal or cubic symmetry?*, Appl. Phys. Lett. **86**, 131927 (2005).

[40] S. Kuroda, N. Nishizawa, M. Mitome *et al.*, *Origin and control of high-temperature ferromagnetism in semiconductors*, Nat. Mater. **6**, 440 (2007).

[41] M. G. Sreenivasan, K. L. Teo, X. Z. Cheng *et al.*, *Structural, magnetic, and transport investigations of CrTe clustering effect in (Zn,Cr)Te system*, J. Appl. Phys. **102**, 053702 (2007).

[42] L. Gu, S. Wu, H. Liu *et al.*, *Characterization of Al(Cr)N and Ga(Cr)N dilute magnetic semiconductors*, J. Magn. Magn. Mater. **290–291**, 1395 (2005).

[43] M. Jamet, A. Barski, T. Devillers *et al.*, *High-Curie-temperature ferromagnetism in self-organized* $Ge_{1-x}Mn_x$ *nanocolumns*, Nature Mater. **5,** 653–659 (2006).

[44] Y. Nishio, K. Ishikawa, S. Kuroda *et al.*, F*ormation of Cr-rich nano-clusters and columns in (Zn,Cr)Te grown by MBE*, In Mater. Res. Soc. Symp. Proc., vol. 1183-FF01-11 of MRS Proceedings (Materials Research Society, 2009).

[45] Y. Ishihara, Y. Yoshita and I. Nakada, *Specific Heat of Germanium Monotelluride*, J. Phys. Soc. Jap. **55**, 1948 (1986).

[46] J. A. C. Marples , *The Lattice Parameters Of α-Manganese at Low Temperatures*, Phys. Lett. A **24**, 207 (1967).

[47] J. Nogués and I. K. Schuller, *Exchange bias*, J. Magn. Magn. Mater. **192**, 203 (1999).

[48] C. Reig, V. Muñoza,b, C. Gó mezc *et al.*, *Growth and characterisation of MnTe crystals*, J. Crystal Growth **223**, 349 (2001).

[49] W. Szuszkiewicz, E. Dynowska, B. Witkowska *et al.*, *Spin-wave measurements on hexagonal MnTe of NiAs-type structure by inelastic neutron scattering*, Phys.

Rev. B **73**, 104403 (2006).

[50] S. M. Durbin, J. Han, Sungki O, M. Kobayashi *et al.*, *Zinc-blende MnTe: Epilayers and quatumn well structure*, Appl. Phys. Lett. **55**, 2067 (1989).

[51] B. Hennion, W. Szuszkiewicz, E. Dynowska *et al.*, *Spin-wave measurements on MBE-grown zinc-blende structure MnTe by inelastic neutron scattering*,Phys. Rev. B **66**, 224426 (2002).

[52] Landolt-Bornstein New Series III **19c**, 14-21 (1988).

[53] Y. D. Park, A. Wilson, A. T. Hanbicki *et al.*, *Magnetoresistance of Mn:Ge ferromagnetic nanoclusters in a diluted magnetic semiconductor matrix*, Appl. Phys. Lett. **78**, 2739 (2001).

[54] J. Kondo, *Resistance Minimum in Dilute Magnetic Alloys*, Prog. Theor. Phys. **32**, 37 (1964).

[55] B. Coqblin, in *Magnetism of metals and alloys* (1982) 295, M. Cyrot Ed., North Holland Publ., Amsterdam.

[56] E. Bauer, *Anomalous properties of Ce-Cu- and Yb-Cu-based compounds*, Adv. Phys. **40**, 417 (1991).

[57] H. T. He, C. L. Yang, W. K. Ge *et al.*, *Resistivity minima and Kondo effect in ferromagnetic GaMnAs films*, Appl. Phys. Lett. **87**, 162506 (2005).

[58] D. Neumaier, M. Schlapps, U. Wurstbauer *et al.*, *Electron-electron interaction in one- and two-dimensional ferromagnetic (Ga,Mn)As*, Phys. Rev. B **77**, 041306(R) (2008).

[59] C. L. Chien and C. R. Westgate (ed.), *The Hall Effect and Its Applications*, (Plenum, New York, 1979).

[60] S. H. Chun, Y. S. Kim, H. K. Choi *et al.*, *Interplay between Carrier and Impurity Concentrations in Annealed* $Ga_{1-x}Mn_xAs$*: Intrinsic Anomalous Hall Effect*, Phys. Rev. Lett. **98**, 026601 (2007)

[61] A. Dyrdal, V. K. Dugaev and J. Barnas, *Anomalous Hall effect in IV-VI magnetic semiconductors*, Phys. Rev. B **78**, 245208 (2008).

[62] H. S. Hsu, C. P. Lin, S. J. Sun *et al.*, *The role of anomalous Hall effect in diluted magnetic semiconductors and oxides*, Appl. Phys. Lett. **96**, 242507 (2010).

[63] S. R. Shinde, S. B. Ogale, J. S. Higgins *et al.*, *Co-occurrence of Superparamagnetism and Anomalous Hall Effect in Highly Reduced Cobalt-Doped Rutile* $TiO_{2-\delta}$ *Films*, Phys. Rev. Lett. **92**, 166601 (2004).

[64] L. Berger, *Side-Jump Mechanism for the Hall Effect of Ferromagnets*, Phys. Rev. B **2**, 4559 (1970).

[65] J. Smit, *The spontaneous hall effect in ferromagnetics II*, Physica (Amsterdam)

24, 39 (1958).

[66] Y. Taguchi, Y. Oohara, H. Yoshizawa *et al.*, *Spin Chirality, Berry Phase, and Anomalous Hall Effect in a Frustrated Ferromagnet*, Science **291**, 2573 (2001).

[67] T. Jungwirth, Q. Niu, and A. H. MacDonald, *Anomalous Hall Effect in Ferromagnetic Semiconductors*, Phys. Rev. Lett. **88**, 207208 (2002).

[68] D. Culcer, J. Sinova, N. A. Sinitsyn *et al.*, *Semiclassical Spin Transport in Spin-Orbit-Coupled Bands*, Phys. Rev. Lett. **93**, 046602 (2004).

[69] G. Bergmann, *Weak Localization in thin films a time-of-flight experiment with conduction electrons*, Phys. Rep. **107**, 1-58 (1984).

[70] B. L. Altshuler and A. G. Aronov, in *Electron-Electron Interactions in Disordered Systems*, ed. A. L. Efros and M. Pollak (North-Holland, Amsterdam, 1985) p. 1.

[71] P. A. Lee and T. V. Ramakrishnan, *Disordered electronic systems*, Rev. Mod. Phys. **57**, 287 (1985).

[72] T. Dietl, *Interplay between Carrier Localization and Magnetism in Diluted Magnetic and Ferromagnetic Semiconductors*, J. Phys. Soc. Jpn. **77**, 031005 (2008).

[73] J. Jaroszyński, T. Andrearczyk, G. Karczewski *et al.*, *Intermediate phase at the metal-insulator boundary in a magnetically doped two-dimensional electron system*, Phys. Rev. B **76** 045322 (2007).

[74] M. Sawicki, T. Dietl, J. Kossut *at al.*, *Influence of s-d Exchange Interaction on the Conductivity of $Cd_{1-x}Mn_xSe$:In in the Weakly Localized Regime*, Phys. Rev. Lett. **56**, 508 (1986).

[75] T. Andrearczyk, J. Jaroszyński, G. Grabecki *et al.*, *Spin-related magnetoresistance of n-type ZnO:Al and $Zn_{1-x}Mn_xO$:Al thin films*, Phys. Rev. B **72**, 121309(R) (2005).

[76] F. Matsukura, M. Sawicki, T. Dietl *et al.*, *Magnetotransport properties of metallic (Ga,Mn)As films with compressive and tensile strain*, Physica E **21**, 1032 (2004).

[77] Ion Garate, Jairo Sinova, T. Jungwirth *et al.*, *Theory of weak localization in ferromagnetic (Ga,Mn)As*, Phys. Rev. B **79**, 155207 (2009).

[78] D. Neumaier, K. Wagner, S. Geißler *et al.*, *Weak Localization in Ferromagnetic (Ga,Mn)As Nanostructures*, Phys. Rev. Lett. **99**, 116803 (2007).

[79] T. Dietl, T. Andrearczyk, A. LipinÅLska *et al.*, *Origin of ferromagnetism in $Zn_{1-x}Co_xO$ from magnetization and spin-dependent magnetoresistance measurements*, Phys. Rev. B **76**, 155312 (2007).

[80] A. Prinz, G. Brunthaler, Y. Ueta *et al.*, *Electron localization in n-$Pb_{1-x}Eu_xTe$*,

Phys. Rev. B **59**, 12983 (1999).

[81] Marcelos L. Peres, V. A. Chitta, and Nei F. Oliveira, Jr *et al.*, *Antilocalization of hole carriers in* $Pb_{1-x}Eu_xTe$ *alloys in the metallic regime*, Phys. Rev. B **79**, 085309 (2009).

[82] W.H. Meiklejohn, C.P. Bean, *New Magnetic Anisotropy*, Phys. Rev. **102**, 1413 (1956).

[83] J. Nogués, I. K. Schuller, *Exchange bias*, J. Magn. Magn. Mater. **192**, 203 (1999).

[84] J. K. Furdyna, X. Liu, Y. Sasaki, S. J. Potashnik and P. Schiffer, *Ferromagnetic III–Mn–V semiconductor multilayers: Manipulation of magnetic properties by proximity effects and interface design (invited)*, J. Appl. Phys. **91**, 7490 (2002).

[85] W.H. Meiklejohn, *Exchange Anisotropy - A Review*, J. Appl. Phys. **33**, 1328 (1962).

[86] K. F. Eid, M. B. Stone, K. C. Ku, O. Maksimov, P. Schiffer, N. Samarth, T. C. Shih and C. J. Palmstrøm, *Exchange biasing of the ferromagnetic semiconductor* $Ga_{1-x}Mn_xAs$, Appl. Phys. Lett. **85**, 1556 (2004).

[87] K. F. Eid, M. B. Stone, O. Maksimov, T. C. Shih, K. C. Ku, W. Fadgen, C. J. Palmstrøm, P. Schiffer and N. Samarth, *Exchange biasing of the ferromagnetic semiconductor (Ga,Mn)As by MnO (invited)*, J. Appl. Phys. **97**, 10D304 (2005).

[88] H. X. Liu, Stephen Y. Wu, R. K. Singh, and N. Newman, J. Appl. Phys. **98**, 046106 (2005).

[89] Po-Hsiang Huang, Hsin-Hung Huang, and Chih-Huang Lai, *Exchange biasing of ferromagnetic Cr-doped GaN using a MnO overlayer*, Appl. Phys. Lett. **90**, 062509 (2007).

[90] R. T. Lechner, G. Springholz, M. Hassan, H. Groiss, R. Kirchschlager, J. Stangl, N. Hrauda, and G. Bauer, *Phase separation and exchange biasing in the ferromagnetic IV-VI semiconductor* $Ge_{1-x}Mn_xTe$, Appl. Phys. Lett. **97**, 023101 (2010).

[91] T. Dietl, *Spin order manipulations in nanostructures of II–VI ferromagnetic semiconductors*, J. Magn. Magn. Mater. **272–276**, 1969 (2004).

[92] T. Dietl, A. Haury, Y. Merle d'Aubignè, *Free carrier-induced ferromagnetism in structures of diluted magnetic semiconductors*,Phys. Rev. B **55**, R3347 (1997).

[93] A. Haury, A. Wasiela, A. Arnoult *et al.*, *Observation of a Ferromagnetic Transition Induced by Two-Dimensional Hole Gas in Modulation-Doped CdMnTe Quantum Wells*, Phys. Rev. Lett. **79**, 511 (1997).

[94] H. Boukari, P. Kossacki, M. Bertolini *et al.*, *Light and Electric Field Control of*

Ferromagnetism in Magnetic Quantum Structures, Phys. Rev. Lett. **88**, 207204 (2002).

[95] D. Ferrand, J. Cibert, A. Wasiela *et al.*, *Carrier-induced ferromagnetism in p-*$Zn_{1-x}Mn_xTe$, Phys. Rev. B **63**, 085201 (2001).

[96] T. Andrearczyk, J. Jaroszyński, M. Sawicki *et al.*, in: N. Miura, T. Ando (Eds.), Proceedings of the 25th International Conference on Physics of Semiconductors, Osaka, Japan, 2000, Springer, Berlin, p. 235 (2001),

[97] M. Sawicki, Le Van Khoi, L. Hansen *et al.*, *Magnetic Characterisation of Highly Doped MBE Grown* $Be_{1-x}Mn_xTe$ *and Bulk* $Zn_{1-x}Mn_xTe$, Phys. Stat. Sol. (b) **229**, 717 (2002).

[98] L. Hansen, D. Ferrand, G. Richter *et al.*, *Epitaxy and magnetotransport properties of the diluted magnetic semiconductor p-BeMnTe*, Appl. Phys. Lett. **79**, 3125 (2001).

[99] G. Karczewski, M. Sawicki, V. Ivanov et al., *Ferromagnetism in (Zn,Cr)Se Layers Grown by Molecular Beam Epitaxy*, J. Supercond. Novel Magn. **16,** 55 (2003).

[100] H. Saito, V. Zayets, S. Yamagata *et al.*, *Room-Temperature Ferromagnetism in a II-VI Diluted Magnetic Semiconductor* $Zn_{1-x}Cr_xTe$, Phys. Rev. Lett. **90**, 207202 (2003).

[101] Y. J. Zhao and A. Zunger, *Zinc-blende half-metallic ferromagnets are rarely stabilized by coherent epitaxy*, Phys. Rev. B **71**, 132403 (2005).

[102] S. Ohta, T. Kanomata, T. Kaneko *et al.*, *Pressure effect on the Curie temperature and thermal expansion of CrTe*, J. Phys.: Condens. Matter **5**, 2759 (1993).

[103] F. Matsukura, H. Ohno, A. Shen *et al.*, *Transport properties and origin of ferromagnetism in (Ga,Mn)As*, Phys. Rev. B **57,** R2037 (1998).

[104] K. M. Yu, W. Walukiewicz, T. Wojtowicz *et al.*, *Effect of the location of Mn sites in ferromagnetic* $Ga_{1–x}Mn_xAs$ *on its Curie temperature*, Phys. Rev. B **65,** 201303 (2002).

[105] T. Jungwirth, J. Sinova, J. Mašek *et al.*, *Theory of ferromagnetic (III,Mn)V semiconductors*, Rev. Mod. Phys. **78**, 809 (2006).

[106] L. Chen, S. Yan, P. F. Xu *et al.*, *Low-temperature magnetotransport behaviors of heavily Mn-doped (Ga, Mn)As films with high ferromagnetic transition temperature*, Appl. Phys. Lett. **95**, 182505 (2009).

[107] L. Chen, X. Yang, F. Yang *et al.*, *Enhancing the Curie Temperature of Ferromagnetic Semiconducto (Ga, Mn)As to 200 K via Nanostructure Engineering*, Nano Lett. **11**, 2584 (2011).

[108] D. Chiba, M. Yamanouchi, F. Matsukura *et al.*, *Electrical Manipulation of Magnetization Reversal in a Ferromagnetic Semiconductor*, Science **301**, 943 (2003).

[109] M. Yamanouchi, D. Chiba, F. Matsukura *et al.*, *Current-induced domain-wall switching in a ferromagnetic semiconductor structure*, Nature **428**, 539 (2004).

[110] R. Fiderling, M. Keim, G. Reuscher *et al.*, *Injection and detection of a spin-polarized current in a light-emitting diode*, Nature **402**, 787 (1999).

[111] Y. Ohno, D. K. Young, B. Beschoten *et al.*, *Electrical spin injection in a ferromagnetic semiconductor heterostructure*, Nature **402**, 790 (1999).

[112] Y. D. Park, A. T. Hanbicki, S. C. Erwin *et al.*, *A Group-IV Ferromagnetic Semiconductor: Mn_xGe_{1-x}*, Science **295**, 651 (2002).

[113] I. Zutic, J. Fabian and S. C. Erwin, *Spin Injection and Detection in Silicon*, Phys. Rev. Lett. **97**, 026602 (2006).

[114] Y. D. Park, A. Wilson, A. T. Hanbicki *et al.*, *Magnetoresistance of Mn:Ge ferromagnetic nanoclusters in a diluted magnetic semiconductor matrix*, Appl. Phys. Lett. **78**, 2739 (2001).

[115] C. Bihler, C. Jaeger, T. Vallaitis *et al.*, *Structural and magnetic properties of Mn_5Ge_3 clusters in a dilute magnetic germanium matrix*, Appl. Phys. Lett. **88**, 112506 (2006).

[116] M. Passacantando, L. Ottaviano, F.D. Orazio *et al.*, *Growth of ferromagnetic nanoparticles in a diluted magnetic semiconductor obtained by Mn^+ implantation on Ge single crystals*, Phys. Rev. B **73**, 195207 (2006).

[117] J. S. Kang, G. Kim, S. C. Wi *et al.*, *Spatial Chemical Inhomogeneity and Local Electronic Structure of Mn-Doped Ge Ferromagnetic Semiconductors*, Phys. Rev. Lett. **94**, 147202 (2005).

[118] H. M. Kim, N. M. Kim, C. S. Park *et al.*, *Growth of Ferromagnetic Semiconducting Si:Mn Film by Vacuum Evaporation Method*, Chem. Mater. **15**, 3964 (2003).

[119] F. M. Zhang, X. C. Liu, J. Gao *et al.*, *Investigation on the magnetic and electrical properties of crystalline $Mn_{0.05}Si_{0.95}$ films*, Appl. Phys. Lett. **85**, 786 (2004).

[120] S. Zhou, K. Potzger, G. Zhang *et al.*, *Structural and magnetic properties of Mn-implanted Si*, Phys. Rev. B **75**, 085203 (2007).

[121] M. Górska and J. R. Anderson, *Magnetic susceptibility and exchange in IV-VI compound diluted magnetic semiconductors*, Phys. Rev. B **38**, 9120 (1988).

[122] S. J. E. A. Eltink, H. J. M. Swagten, N. M. J. Stoffels *et al.*, *Correlation between electronic and magnetic properties in the IV-VI group diluted magnetic semiconductor SnMnTe*, J. Magn. Magn. Mater. **83**, 483 (1990).

[123] T. Story, R. R. Calazka, R. B. Frankel *et al.*, *Carrier-concentration induced ferromagnetism in PbSnMnTe,* Phys. Rev. Lett. **56**, 777, (1986).

[124] A. J. Nadolny, J. Sadowski, B. Taliashvili *et al.*, *Carrier induced ferromagnetism in epitaxial* $Sn_{1-x}Mn_xTe$ *layers*, J. Magn. Magn. Mater. **248,** 134 (2002).

[125] Y. Fukuma, H. Asada, J. Miyashita *et al.*, *Magnetic properties of IV–VI compound GeTe based diluted magnetic semiconductors,* J. Appl. Phys. **93**, 7667 (2003).

[126] M. L. Reed, N. A. El-Masry, H. H. Stadelmaier *et al.*, *Room temperature ferromagnetic properties of (Ga, Mn)N*, Appl. Phys. Lett., **79**, 3473 (2001).

[127] S. E. Park, H. J. Lee, Y. C. Cho *et al.*, *Room-temperature ferromagnetism in Cr-doped GaN single crystals*, Appl. Phys. Lett., **80**, 4187 (2002).

[128] Y. Matsumoto, M. Murakami, T. Shono *et al.*, *Room-temperature ferromagnetism in transparent transition metal-doped titanium dioxide*, Science **291**, 854 (2001).

[129] K. Ueda, H. Tabata, and T. Kawai, *Magnetic and electric properties of transition-metal-doped ZnO films*, Appl. Phys. Lett. **79**, 988 (2001).

[130] P. Sharma, A. Gupta, K.V. Rao *et al.,Ferromagnetism above room temperature in bulk and transparent thin films of Mn-doped ZnO*, Nat. Mater. **2**, 673 (2003).

[131] H. Katayama-Yoshida, K. Sato, T. Fukushima *et al.*, *Theory of ferromagnetic semiconductors*, Phys. Status Solidi A **204,** 15–32 (2007).

[132] H. Pan, J. B. Yi, L. Shen *et al.*, *Room-Temperature Ferromagnetism in Carbon-Doped ZnO*, Phys. Rev. Lett. **99**, 127201 (2007).

[133] M. D. McCluskey and S. J. Jokela, *Defects in ZnO*, J. Appl. Phys. **106**, 071101 (2009).

[134] W. D. Johnston and D. E. Sestrich, *The MnTe-GeTe Phase Diagram***,** J. Inorg. Nucl. Chem., **19**, 229 (1961).

[135] Y. Fukuma, T. Murakami, H. Asada *et al.*, *Film growth of* $Ge_{1-x}Mn_xTe$ *using ionized-cluster beam technique*, Physica E **10,** 273 (2001).

[136] Y. Fukuma, M. Arifuku, H. Asada *et al.* , *Correlation between magnetic properties and carrier concentration in* $Ge_{1-x}Mn_xTe$, J. Appl. Phys. **91**, 7502 (2002).

[137] W. Q. Chen, K. L. Teo, M. B. A. Jalil *et al.*, *Compositional dependencies of ferromagnetic* $Ge_{1−x}Mn_xTe$ *grown by solid-source molecular-beam epitaxy,* J. Appl. Phys. **99**, 08D515 (2006).

[138] Y. Fukuma, K. Goto, S. Senba *et al.*, *IV-VI diluted magnetic semiconductor* $Ge_{1−x}Mn_xTe$ *epilayer grown by molecular beam epitaxy*, J. Appl. Phys. **103**, 053904 (2008).

[139] Y. Fukuma, H. Asada, S. Miyawaki *et al.*, *Carrier-induced ferromagnetism in $Ge_{0.92}Mn_{0.08}Te$ epilayers with a Curie temperature up to 190 K*, Appl. Phys. Lett. **93**, 252502 (2008).

[140] W. Q. Chen, K. L. Teo, S. T. Lim *et al.*, *Magnetic and transport behaviors in $Ge_{1-x}Mn_xTe$ with high Mn composition*, Appl. Phys. Lett. **90**, 142514 (2007).

[141] W. Q. Chen, S. T. Lim, C. H. Sim *et al.*, *Optical, magnetic, and transport behaviors of $Ge_{1-x}Mn_xTe$ ferromagnetic semiconductors grown by molecular-beam epitaxy*, J. Appl. Phys. **104**, 063912 (2008).

[142] M. Hassan, G. Springholz, R. T. Lechner *et al.*, *Molecular beam epitaxy of single phase GeMnTe with high ferromagnetic transition temperature*, J. Cryst. Growth **323**, 363 (2011).

[143] H. Sato, K. Fujimoto, Y. Fukuma *et al.*, *Mn 3d states in ferromagnetic semiconductor $Ge_{1-x}Mn_xTe$ investigated by Mn 2p-3d soft X-ray magnetic circular dichroism spectroscopy*, J. of Elec. Spectroscopy and Related Phenomena, **144–147**, 727 (2005).

[144] Y. Fukuma, H. Sato, K. Fujimoto *et al.*, *Local environment of Mn atoms in IV-VI ferromagnetic semiconductor $Ge_{1-x}Mn_xTe$*, J. Appl. Phys., **99**, 08D510 (2006).

[145] Z. Xie, W. D Cheng, D. S. Wu *et al.*, *Ab initio study of ferromagnetic semiconductor $Ge_{1-x}Mn_xTe$*, J. Phys.: Condens. Matter, **18,** 7171 (2006).

[146] A. Ciucivara, B. R. Sahu and L. Kleinman, *Density functional study of $Ge_{1-x}Mn_xTe$*, Phys. Rev. B, **75**, 241201(R) (2007).

[147] Y. H. Zhao and B. G. Liu, *High spin polarization in ternary Ge–Mn–Te compounds based on rocksalt semiconducting GeTe*, J. Phys.: Condens. Matter **20**, 135225 (2008).

CHAPTER 3

3. EXPERIMENTAL DETAILS ON THE GROWTH AND CHARACTERIZATIONS

The molecular-beam expitaxy (MBE) system was used to synthesize the samples that were discussed in this thesis. It is equipped with an *in situ* reflection high energy electron diffraction (RHEED) system to monitor the growth mode and surface reconstruction. Subsequently, various characterization methods were used to study the structural, magnetic and electrical properties of the samples. The structural properties were characterized by atomic force microscopy (AFM), X-ray diffraction (XRD), X-ray photoelectron spectroscopy (XPS) and transmission electron microscopy (TEM). The magnetic properties were characterized mainly by the superconducting quantum interference device (SQUID) magnetometer. For the electrical properties, the magnetotransport experiments were carried using a low temperature cryostat which is also customized for hydrostatic pressure experiments using a pressure cell. The main objectives of these characterizations were to investigate the magnetic properties, such as magnetization and T_c, and their correlation with the structural and electrical properties so as to provide a better understanding of the material, $Ge_{1-x}Mn_xTe$.

3.1 Epitaxial Growth using the Molecular Beam Epitaxy (MBE) System

The MBE is an ultrahigh vacuum (UHV) evaporation technique for growth of epitaxial layers from constituents of directed thermal energy atomic or molecular beams. The notion of epitaxy can be inferred as the orderly arrangement of atoms upon each other. Typically, for epitaxial thin film growth, the lattice mismatch is less than 5 %. The UHV ensures that highly directional atoms or molecules beam is directed onto the substrate without having scattered by residual gas molecules. However, the growth is essentially kinetically limited and it is governed by the arrival rates and surface lifetimes of the impinging species.

The model of the MBE system used is ULVAC MBC-1000-2C which comprises of a preparation chamber and a growth chamber. These are stainless steel chambers connected to a turbomolecular pump and a rotary pump. In addition, the growth chamber is equipped with titanium getter pump and sputter ion pump to achieve a pressure of ~ 10^{-10} Torr when cooled with liquid nitrogen. A schematic diagram of the system is shown in Figure 3.1. The preparation chamber is separated from the growth chamber by a load-lock valve where the substrates, BaF_2 and GaAs, are degassed at $T = 250$ ˚C prior to actual deposition in the growth chamber. The epi-ready square (~ 16 mm) GaAs or the circular (~ 25.4 mm) BaF_2 substrates are placed on a custom-made hollow substrate holder made of Molybdenum. A total of four substrates can be loaded at the same time into the preparation chamber. The growth chamber consists of eight effusion cells with individual mechanical shutter. The compound GeTe and elemental Mn, Zn and Te (valved cracker) were used for this research work.

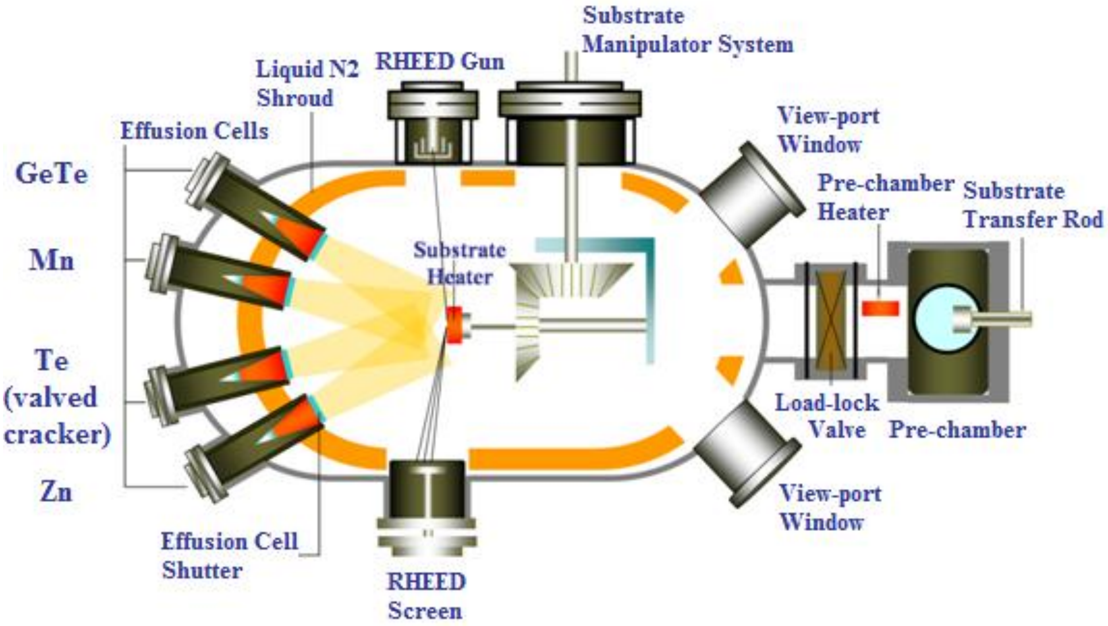

Figure 3.1 A schematic diagram of the MBE system.

These effusion cells are independently heated until the respective desired material's beam equivalent pressure (BEP) has been met. Prior to raising the cell temperature, a good background pressure (~ 1×10^{-9} Torr) is ensured with continuous inflow of liquid nitrogen to allow accurate calibration of the BEP. The BEP varies linearly with temperature and the typical range of BEP used for GeTe, Mn and Zn are 1×10^{-6}, 5×10^{-8} and 1×10^{-7} Torr at 340, 670, 210 ˚C, respectively. The Te source is controlled using a valved cracker (EPI-200V-Te) via dual heater at the bulk and cracker zones. The temperatures at the bulk and cracker zones are set at 330 ˚C and 650 ˚C, respectively to achieve a BEP of 1×10^{-7} Torr. At sufficient high temperature ~ 650 ˚C at the cracker zone, the Te molecules form Te_2 which have higher sticking coefficients than that of the uncracked counterparts. Additionally, the Te opening is controlled automatically by a servo motor controller (SMC) which allows a more accurate control of the Te flux. The BEP is related the flux (J) of species which then affects the composition and growth rate of the sample. The following equation has been use as a guideline to determine the desired BEP and hence the flux ratio [1].

$$\frac{J_x}{J_y}=\frac{BEP_x}{BEP_y}\cdot\frac{\eta_y}{\eta_x}\cdot\frac{\sqrt{T_x\cdot M_y}}{\sqrt{T_y\cdot M_x}} \tag{3.1}$$

where $\eta_i=\left[(0.4Z/14)+0.6\right]\eta_{N2}$ is the ionization efficiency in relation to N_2 and Z is the atomic number, T_i and M_i, are the cell temperature and molar mass of species i, respectively. The substrate is being transferred from the preparation chamber to the growth chamber via the transfer rod. The substrate manipulation system allows the substrate to be rotated during growth to increase the uniformity of the film. Prior to growth, a deoxidation process is carried out at T_s ~ 350 and 580 ˚C for BaF_2 and GaAs substrates, respectively, together with Te exchange for about 5 – 10 mins. Overall, the operation of shutters, cell and substrate temperatures, and rotation speed can be manipulated through the touch panel control as well as computer automation.

The MBE is equipped with an *in situ* RHEED system to monitor the growth mode and surface reconstruction. Typical growth modes are Frank-van der Merwe, Volmer-Weber (VW) and Stranski-Krastanow (SK). The first mode refers to the preferential attachment of adatoms to surface sites resulting in 2D atomically smooth layers. While the VW mode leads to 3D clusters and SK mode is characterized by both 2D and 3D island growth. These are due to adatom-adatom interactions being stronger than those of the adatom with the surface.

The RHEED system directs an electron beam of 20 keV at a glancing angle of < 3 ° to the sample surface and allows it to scatter onto a fluorescent screen. Some of these electrons interfere constructively as they pass through the crystal lattice forming diffraction patterns. The conditions for constructive interference of the elastically scattered electrons may be inferred using the Ewald construction in the reciprocal lattice. In the case where the interaction of the electron beam is essentially with a two dimensional atomic net, the reciprocal lattice is composed of rods in reciprocal space in a direction normal to the real surface. As such, the RHEED patterns can provide information of the film surface, crystal orientation and indications of surface roughness. Typically, streaky lines, spotty, ring and diffused patterns are observed and they indicate layer-by-layer (2D), island growth (3D), polycrystalline and amorphous surface, respectively [2].

3.2 Characterization of Structural Properties

The structural properties were characterized by AFM, XRD, XPS and TEM. The AFM and XRD are used to study the surface morphology and the crystal structures and orientations, respectively. The XPS is used to examine the chemical state of the elements in the film and thereby determine the chemical composition and depth profile. In order to image the sample with atomic resolution the TEM is necessary. It not only shows the crystal structure and the interface quality of each layer, but capable of determining the chemical composition of specific region when equipped with an energy-dispersive X-ray spectroscopy (EDS) system. These techniques are indispensable in FMS materials research.

3.2.1 Atomic Force Microscopy (AFM)

The AFM is a useful tool for measuring roughness and imaging the topography of surfaces. The system used in this work is the Digital Instruments Nanoscope III (DI-3100) multimode scanning force microscope. It can operate in three modes, namely contact, non-contact and tapping modes. They differ by the way the cantilever with a probe at its end traverse across the surface. Nevertheless, the basic working principle is similar. The tapping mode has been used in this case. In this mode, the cantilever oscillates near the resonant frequency at a particular height as it traverses across the surface. The probe interacts with the surface by means of van der Waals forces. With a different surface topography, the cantilever's deflection changes and this is monitored by optical means. The laser which is directed on to the cantilever is reflected onto a position-sensitive photodiode. This signals the piezoelectric crystal to adjust the tapping height back to its relative distance from the surface. Thus, the changes in the height information can be used to map the topography of the surface [3].

3.2.2 X-ray Diffraction (XRD)

The XRD is a non-destructive analytical technique capable of identifying the possible phases of compounds and verifying crystallographic quality and orientation of the films [4]. The Philips X'PERT MRD high resolution X-ray diffractometer was used in this work. The measured XRD patterns are compared with an internationally recognized database containing reference patterns for more than 70,000 phases.

The diffraction patterns are formed when the reflected X-rays from atoms of different crystal planes interfere with each other. These reflected rays are emitted from atoms when the incident X-rays interact with the electrons in the crystal causing them to oscillate in the same frequency. The X-ray source is predominately Cu $K_{\alpha 1}$ X-ray with a wavelength of 1.54056 Å, although traces of $K_{\alpha 2}$ (1.54402 Å) and K_{β} (1.39208 Å) are detected as well. When a monochromatic X-ray with wavelength (λ) is incident at an angle (θ) on lattice planes with inter-plane distance (d), contructive interference (peaks) occurs when the distance travelled by X-rays reflected from successive phases differs by an integer number (n) of λ . This is governed by the Bragg's law.

$$2d\sin\theta = n\lambda \tag{3.2}$$

The system mainly comprises of the source, sample stage and detector. These are aligned along the circumference of the focusing circle. The angle forms between the plane of the stage and the source is θ, while the angle between the projection of the source and detector is 2θ . Thus the diffraction patterns measured with such geometry are often known as $\theta - 2\theta$ scan. By using appropriate equations for d depending on the type of crystal structure, the Miller index and hence the crystal orientation can be determined. Lastly, the shift in the peak angles with the addition of dopants in the host can provide an estimate on the composition of substitutional dopants in the lattice. For $Ge_{1-x}Mn_xTe$, the addition of Mn into GeTe is found to shift the 2θ peak to higher angles which correspond to a decrease in the lattice constant [5].

3.2.3 X-ray Photoelectron Spectroscopy (XPS)

The XPS system (PHI Quantum 2000: Scanning ESCA Microprobe) was used to examine the chemical state of the elements present in the film and thereby determine the film's chemical composition and depth profile. It consists of mainly an Al anode X-ray source, an electron energy analyzer, a low energy electron flood gun for reducing the charging effect in insulating sample and an Ar ion source for sputtering. This technique involves the measurement of the kinetic energy (*KE*) of photoelectrons ejected from sample surface when excited by a monochromatic soft X-ray. The photoemission effect is illustrated in Figure 3.2. The binding energy (*BE*) of the photoelectron can thus be calculated as,

$$BE = hv - KE - \phi + \delta \tag{3.3}$$

where hv is the excitation X-ray energy, ϕ is the electron spectrometer work function and δ is the net surface charge. Since each element has a unique spectrum of number of electrons per energy interval versus their *KE*, they can be identified quantitatively by their exact peak position and relative peak height.

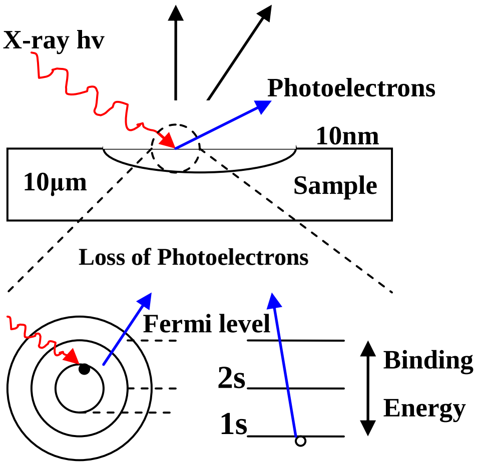

Figure 3.2 An illustration of the photoemission effect.

For a depth profile analysis, sputtering is used to etch the sample surface and specific element's chemical states are analyzed at each interval. The chemical state of the desired element must be selected carefully so as not to have peak position that overlaps with that of other elements. In this work, the chemical states of the relevant elements were chosen as Ge ($2p_{3/2}$), Te ($3d_{5/2}$), Mn ($2p_{3/2}$), Zn ($2p_{3/2}$), Ga ($2p_{3/2}$), As ($2p_{3/2}$), Ba ($3d_{5/2}$) and F (1s).

3.2.4 Transmission Electron Microscopy (TEM)

The TEM allows the imaging of the crystallographic structure of a sample at an atomic scale [6]. The working principle of TEM is similar to that of a light microscope except that electron is used instead of light to achieve atomic resolution. An accelerated beam of electron transmits through the thin specimen to form an image which is magnified and displayed on fluorescent screen or detected using a CCD camera. The transmitted electrons undergo elastic and inelastic scattering which provide crystallographic information such as diffraction patterns and spatial variation in intensity which differentiates crystal defects and secondary phases, respectively.

In order to determine the crystal structure of each layer the selective-area electron diffraction (SAED) patterns can be analyzed. Electron diffraction patterns can be equated with reciprocal lattice patterns. It is often possible to index an electron diffraction pattern by noting its symmetry. A reciprocal lattice has the same symmetry as its real lattice. The

TEM system (JEOL 2300) used was also equipped with EDS which allows elemental analysis. It detects the X-ray emitted when an electron from a higher energy shell fills a lower energy empty shell whose electron has been excited by the incident electron beam. Similar to XPS, it creates spectral lines that are specific to individual elements and thus capable of determining chemical composition and elemental mapping of specific regions.

3.3 Characterization of Physical Properties

The physical properties, such as the magnetic and electrical properties, were characterized using the SQUID and low temperature cryostat, respectively. Often, the magnetization as a function of temperature is measured to determine the T_c of $Ge_{1-x}Mn_xTe$ samples. Additionally, hysteresis loops also provides information on coercivity, remanent and saturation magnetization. Owing to the low T_c exhibited by the samples, electrical measurements had to be carried out at low temperature to investigate the effects of FM on the charge transport. Typically, magnetoresistance and Hall resistivity were measured. The low temperature cryostat is also customized for pressure cell measurement. The cell allows hydrostatic pressure to be exerted onto the sample and performing electrical measurements at the same time.

3.3.1 Superconducting Quantum Interference Device (SQUID) magnetometry

The Quantum Design Magnetic Property Measurement System (MPMS-7XL) was used to study the magnetic properties of the grown samples over a range of temperatures (2 – 400 K) and magnetic fields (± 7 T). The Josephson Effect is used in the detection of magnetization by monitoring the change in the current across a very narrow insulating gap between two superconductors. The SQUID comprises of two (dc) and one (rf) Josephson junctions within the loop of the superconducting materials. The high sensitivity of this device to changes in the current renders the SQUID effective in detecting small magnetic flux.

The sample of ~ 6.5×6.5 mm^2 is suspended on a rod and placed within the superconducting pick-up coil that is surrounded by the superconducting magnet. As the sample traverse along the coil in the presence of magnetic field, the sample magnetic flux induces a change in the current that is proportional to it. The pick-up coil being coupled to the sensor allows any variation to the current in the coil to be detected. Consequently, the sample's magnetic moment can be determined. The sequence of actions to be executed can be programmed. For instance, a zero field-cooled (field-cooled) measurement requires the sample to be cooled from 300 K to 5 K without (with) magnetic field and the sample's magnetization is subsequently measured with applied field as a function of temperature.

3.3.2 Pressure and Transport measurement using the Oxford Cryostat

The magnetic field and temperature dependence of resistivity were performed using the low temperature Oxford cryostat (Spectromag SM4000). The schematic of the transport measurement setup is shown in Figure 3.3. The setup was constructed by this Ph.D. candidate and the respective meters and controllers were interfaced with the PC's Labview program written by him via the General Purpose Interface Bus (GPIB).

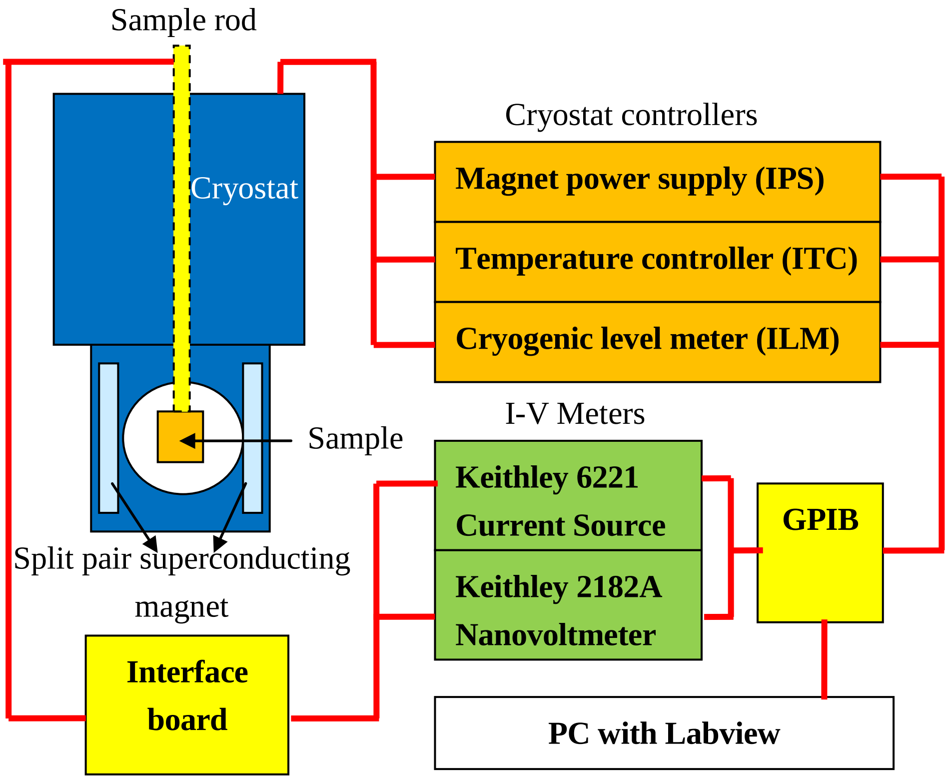

Figure 3.3 A schematic diagram of the transport measurement setup.

The sample was placed in between the split pair of superconducting magnets via a sample rod. Two pairs of temperature sensor and heater situated near the top and bottom of the sample were controlled by the ITC to regulate the sample space temperature (1.2 – 200

K). The superconducting magnet was controlled by the IPS which generate magnetic field ($\pm 10\,\mathrm{T}$) with various sweep rate. The Keithley model 6221/2182A current source and nanovoltmeter were use in synchronization to eliminate power line related noise. These meters were connected the sample rod using triax cables to further reduce noise. Prior to measurements, Cr-Au metal (ohmic) contacts were deposited onto the sample with either linear four point or van der Pauw configurations at room temperature using an evaporator. Subsequently, indium wires are soldered onto the sample's and the sample rod's contacts to form close circuit.

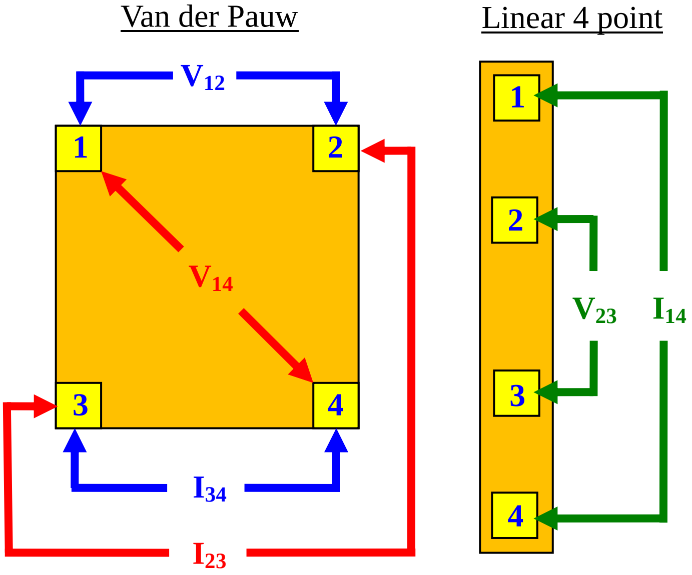

Figure 3.4 A schematic diagram of van der Pauw and linear four point contacts configurations for resistivity measurements.

For the van der Pauw geometry, the resistivity (ρ) can be obtained as

$$\rho = \frac{\pi}{\ln 2}\left(\frac{V_{12}}{I_{34}} + \frac{V_{31}}{I_{42}}\right)t \tag{3.4}$$

where t is the sample thickness, V_{12} (V_{31}) is the potential difference across contacts1 (3) and 2 (1); and I_{34} (I_{42}) indicates the current enters the sample through contact 3 (4) and leaves through contact 4 (2), respectively. The Hall resistance was obtained by having the current and voltage orthogonal to each other and the magnetic field applied normal to the sample surface plane. That is applying I_{23} and measuring V_{14} as shown in Figure 3.4. For magnetoresistance (MR) measurement, the linear four point geometry can be used by applying I_{14} and measuring V_{23} as also depicted in Figure 3.4. In this case, the magnetic field can be applied either perpendicular or parallel to the sample plane. The MR is defined as

$$\mathrm{MR} = \frac{\mathrm{R}(\mathrm{H}) - \mathrm{R}(0)}{\mathrm{R}(0)} \tag{3.5}$$

where $\mathrm{R}(\mathrm{H})$ and $\mathrm{R}(0)$ denote the resistances at with and without applied field, respectively.

The hydrostatic pressure experiments were carried out using a pressure cell (easyCell 30). It is a doubled wall cylinder made of BeCu alloy, capable of withstanding a maximum pressure of 2.5 GPa and customized to fit into the cryostat sample space. The sample ~ $3 \times 3\ \mathrm{mm}^2$ was attached to the electrical feedthroughs by four contact points in a van der Pauw geometry using indium as the ohmic contact metal. It was immersed in the pentane mixture transmitting medium so that the applied pressure is exert onto the whole sample. The feedthroughs together with the sample were then fitted into the pressure cell. Figure 3.5 shows the setup of the pressure cell which can be mounted onto the cryostat sample rod.

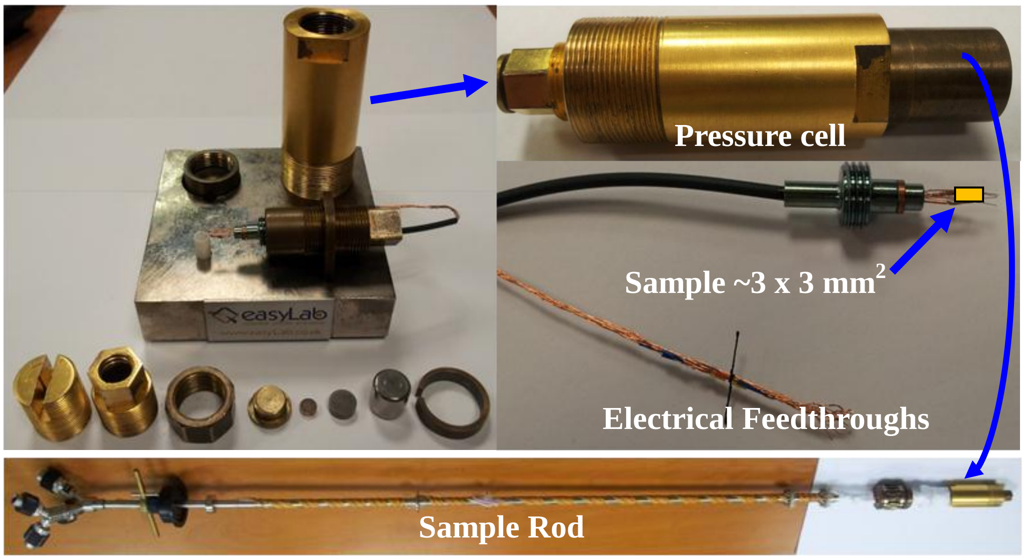

Figure 3.5 The pressure cell assembly and the placement of the sample on the electrical feedthrough. The pressure cell is mounted onto the sample rod for magnetotransport measurement.

A hydraulic press system was used to increase the pressure subjected onto the sample and the sample's actual pressure was monitored by the resistance of the manganin manometer situated underneath the sample. After the pressure was applied, the cell was mounted onto the customized sample rod for magnetotransport measurement in the cryostat. After each pressure measurement, the pressure cell is removed from the cryostat and mounted onto the hydraulic press system to increase the applied pressure to the next value.

Chapter 3 References

[1] E.H.C. Parker (ed.), *The technology and physics of molecular beam epitaxy*, (Plenum Press, New York) (1985).

[2] W. Braun, *Applied RHEED : Reflection high-energy electron diffraction during crystal growth*, (Springer, New York) (1999).

[3] D. Sarid, *Scanning force microscopy : with applications to electric, magnetic, and atomic forces,* (Oxford University Press, New York), 181 (1994).

[4] B. D. Cullity, and S.R. Stock, *Elements of X-ray diffraction*, (Prentice-Hall International, London) (2001).

[5] J. F. Bi and K. L. Teo, *Nanoscale* $Ge_{1-x}Mn_xTe$ *ferromagnetic semiconductors*, in The Oxford Handbook of Nanoscience and Technology (Materials, Structures, Properties and Characterization Techniques, ed. By A. V. Narlikar and Y. Y. Fu, vol. II page 632 (2010).

[6] B. Fultz and J. Howe, *Transmission electron microscopy and diffractometry of materials,* (Springer, New York) (2002).

CHAPTER 4

4. OPTIMIZATION OF GROWTH FOR $Ge_{1-x}Mn_xTe$ ON BaF_2 AND GaAs SUBSTRATES

This Chapter presents the MBE growth of $Ge_{1-x}Mn_xTe$ on BaF_2 and GaAs substrates. We are the first to use MBE to grow $Ge_{1-x}Mn_xTe$. The effects of various growth conditions, such as GeTe, Mn, Te fluxes and substrate temperatures on the structural and physical properties of $Ge_{1-x}Mn_xTe$ will be discussed. While BaF_2 has been widely used to grow $Ge_{1-x}Mn_xTe$ layer, so far no one has reported the growth of $Ge_{1-x}Mn_xTe$ on GaAs. Compared to BaF_2, GaAs is more commercially viable.

4.1 Introduction and Motivation

It is well known that the growth conditions of FMS have tremendous effect on its structural and magnetic properties. Recently relatively high Mn composition of 20 % had been reported in $Ga_{1-x}Mn_xAs$ by post-growth annealing resulting in T_c approaching 200 ˚C [1]. The annealing process has effectively reduced interstitial Mn which compensates the overall ferromagnetism in $Ga_{1-x}Mn_xAs$. For $Ge_{1-x}Mn_xTe$, the substrate temperature (T_s) and excess Te flux were reported to affect the crystal quality and hole concentrations (p) [2]. While higher $T_s \sim 350$ ˚C with sufficient Te flux prevents the formation of nonstoichiometric defects, it lowers p. On the other hand, low T_s ~ 250 ˚C degrades the crystal quality, yet increases p. Since the ferromagnetism in $Ge_{1-x}Mn_xTe$ is mediated by carriers via RKKY interactions, a higher p is preferred. Additionally, with T_s ~ 260 ˚C and $T_s \geq$ 330 ˚C, there seems to be a tendency for zinc-blende and hexagonal MnTe to be formed, respectively [3].

In this Chapter, we explore the effects of the GeTe, Mn and Te source fluxes and substrate temperatures on $Ge_{1-x}Mn_xTe$ grown on BaF_2 and GaAs substrates. The results demonstrate that homogenous $Ge_{1-x}Mn_xTe$ (T_c ~ 130 K, x ~ 0.3) can be grown on BaF_2 at T_s = 250 ˚C under suitable growth conditions without the occurrence of other phases. On the other hand, the growth of $Ge_{1-x}Mn_xTe$ on GaAs substrate is more challenging due to the large lattice mismatched between them. The lattice constants (a) of zinc-blende GaAs is 5.65 Å, while as that for rock-salt GeTe is 5.98 Å. We had selected zinc-blende ZnTe (a = 6.10 Å) as a buffer layer to reduce the lattice mismatch, since it grows well on GaAs. A lower T_s = 180 ˚C is found to promote the surface adsorption of Ge atoms and also a more homogenous $Ge_{1-x}Mn_xTe$ layer.

4.2 Experimental Details

A total of 16 samples were grown by the MBE system in this study. Six of which were grown directly on BaF_2 substrates and the rest were grown on GaAs substrates with ZnTe buffer layer. The ZnTe layers were grown directly on GaAs at T_s = 180 ˚C for 1 hr and all of the $Ge_{1-x}Mn_xTe$ layers were grown for 2 hrs. The source flux and substrate temperatures were varied systematically for each sample. During the growth process the surface quality of the samples was monitored by *in situ* RHEED. The crystal structures and quality of the films were studied by Cu *K*α high-resolution XRD as well as the TEM. The XPS was used to determine the depth profile of the samples and provide estimate of the Mn composition (x) in the $Ge_{1-x}Mn_xTe$ layer. The surface roughness was measured using the AFM. The magnetic properties were investigated by the SQUID magnetometer.

4.3 Results and Discussion

4.3.1 Growth parameters influencing the physical and structural properties of $Ge_{1-x}Mn_xTe$ grown on BaF_2.

The growth conditions used to fabricate the samples A to F are as shown in Table 4.1. The fluxes of each source were varied systematically to understand their effects on the structural and magnetic properties of the grown $Ge_{1-x}Mn_xTe$. The use of compound GeTe instead of elemental Ge sources reduces the probability of forming GeMn compounds. All samples were grown at T_s ~ 250 ˚C except for Sample F which was grown at 300 ˚C to study the effect of having higher T_s.

Table 4.1 Substrate temperatures and BEP of sources used for samples A to F, and their respective Mn compositions (x).

Sample	T_s / ˚C	GeTe/ 10^{-6} Torr	Mn/ 10^{-8} Torr	Te/ 10^{-7} Torr	x
A	250	4.0	14.0	8.2	0.10
B	250	4.0	14.0	5.0	0.12
C	250	2.6	5.2	5.0	0.90
D	250	2.6	5.2	1.4	0.30
E	250	2.6	11.0	1.4	0.80
F	300	2.6	5.2	1.4	0.97

The RHEED pattern of BaF_2 after deoxidation at 350 ˚C for 10 mins followed by Te exchange for 5 mins is shown in Figure 4.1. These are typical patterns for rock-salt structure at the azimuth of [110] and [100]. Figure 4.1 also shows the RHEED patterns of samples A to F after 2 hrs of growth.

Sample A and B were grown with relatively high Te flux. As the sources shutters were opened simultaneously the bright RHEED spots of BaF_2 lengthened and streaky pattern were observed after 2 mins of growth. Subsequently, reconstruction lines began to form at the [100] direction suggesting the good crystalline quality of the layer. Bright streaky RHEED patterns were then observed and persisted throughout the 2 hours growth.

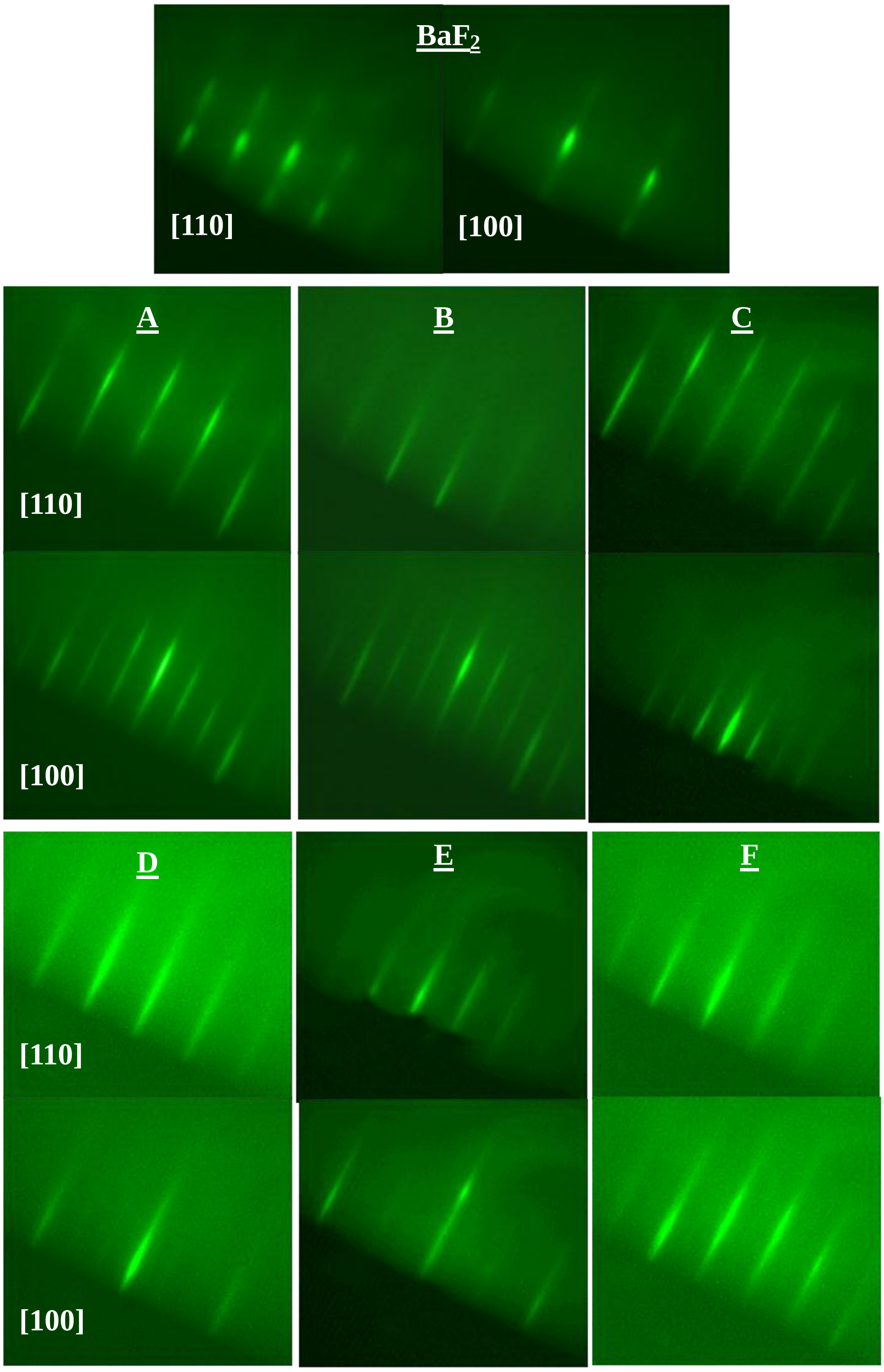

Figure 4.1 The RHEED patterns of BaF_2 after deoxidation and Te exchange as well as those of samples A to F after 2 hrs of growth at azimuth [110] and [100].

The XPS profile shown in Figure 4.2 reveals a $Ge_{1-x}Mn_xTe$ thickness of ~ 420 nm and the Mn compositions can be determined to be 0.10 and 0.12 for Sample A and B, respectively. It can be said that the excess Te flux is mainly used to facilitate the crystalline growth of the $Ge_{1-x}Mn_xTe$. Additionally, comparing Samples B and C, although the GeTe and Mn fluxes were lower for Sample C (x ~ 0.9), the RHEED patterns during the growth were very similar to Sample B.

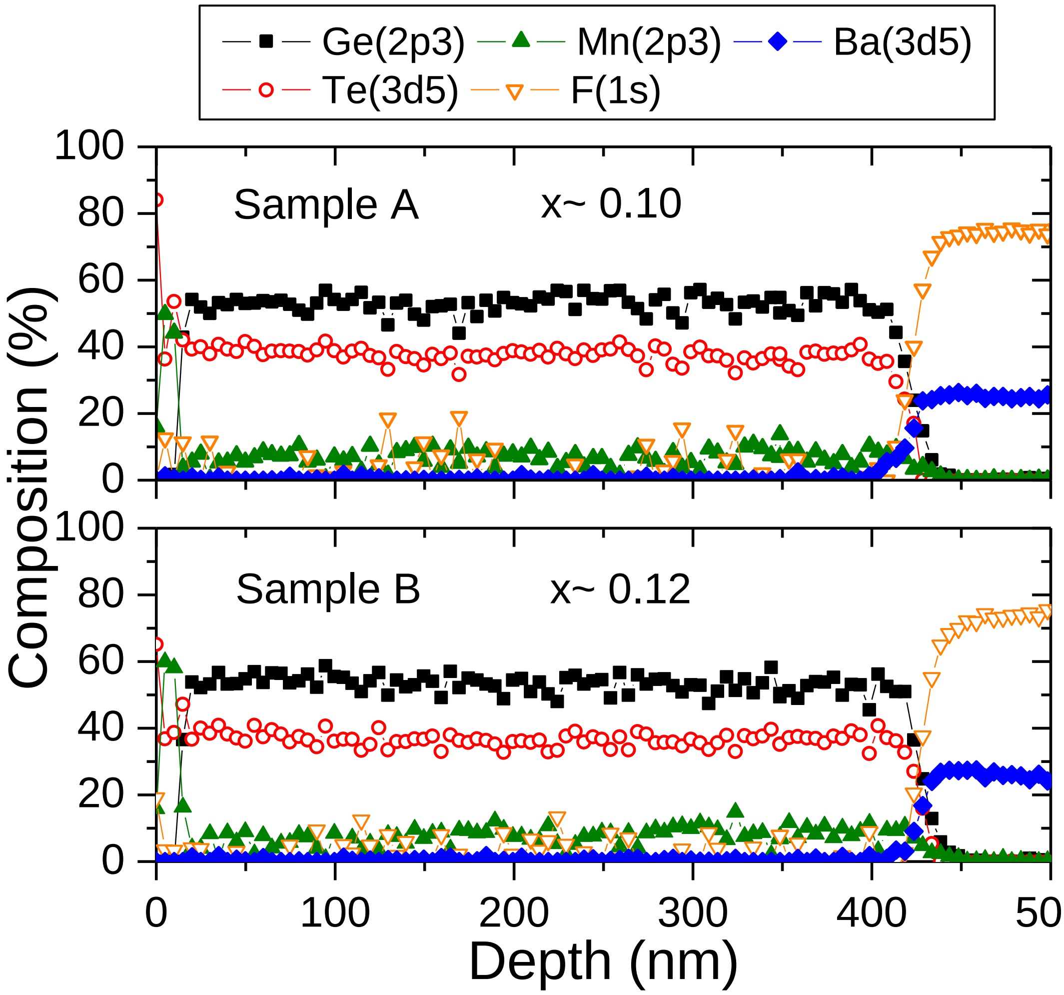

Figure 4.2 The XPS depth pofile of Sample A and B with Mn composition (x) of 0.10 and 0.12, respectively.

Owing to the high excess Te flux, Sample A, B and C had similar structure as shown by the XRD results in Figure 4.3. The high intensity rock-salt GeTe (222) and $Ge_{1-x}Mn_xTe$ (222) peaks, close to that of BaF_2 (222) peak, indicates good quality of the film is achieved. However, the presence of both GeTe and $Ge_{1-x}Mn_xTe$ peaks could suggest the occurrence of these two phases within the samples.

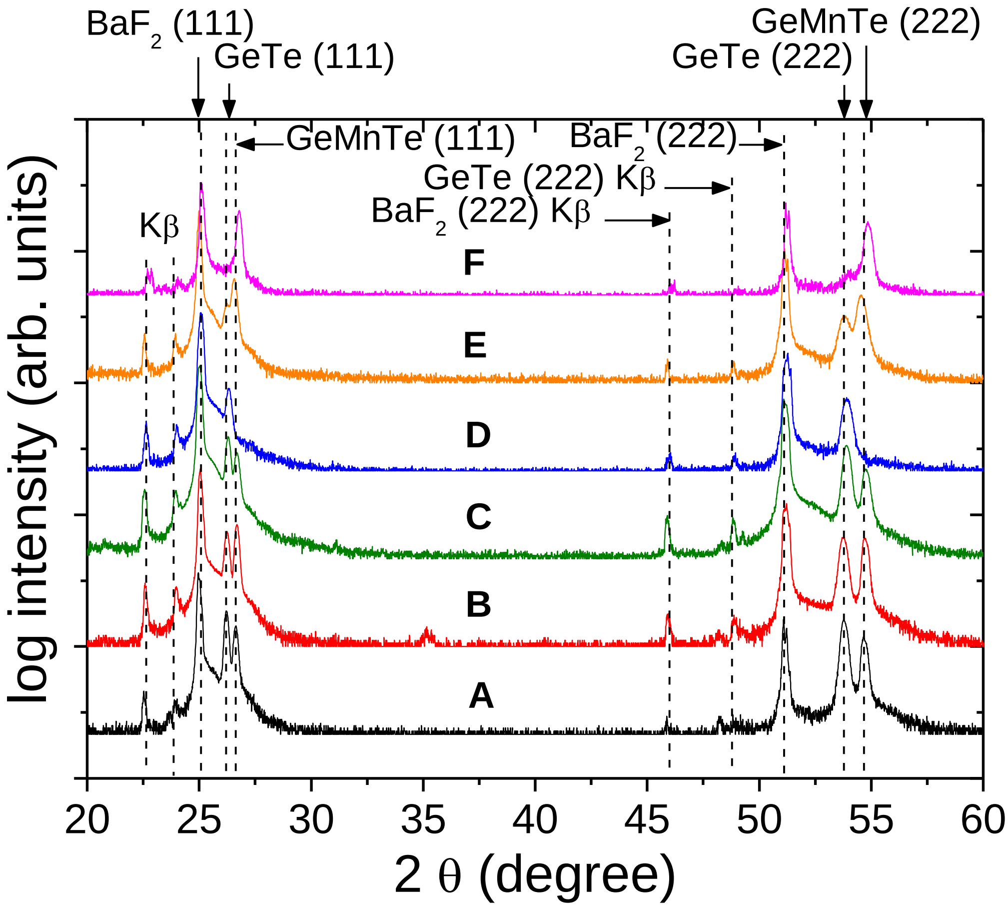

Figure 4.3 The XRD 2θ patterns of samples A to F.

Sample D was grown with a lower Te flux compared to Sample C. It took about 3 mins after the sources shutters were opened, before a clear streaky RHEED pattern was observed. During the growth a streaky 1×3 surface reconstruction was observed and it maintained throughout the 2 hours growth as shown in Figure 4.1. This suggests the good crystalline quality of the layer is obtained. The XRD peak near 54 ° is likely to correspond to $Ge_{1-x}Mn_xTe$ (222) instead of GeTe (222) due to its strong magnetic signals as shown in Figure 4.5. The single $Ge_{1-x}Mn_xTe$ (222) XRD peak which shows no segregation from GeTe (222) further indicates that the film is homogeneous.This suggests that excessive Te flux also results in separate phases of GeTe and $Ge_{1-x}Mn_xTe$. By introducing higher Mn flux as in Sample E, a streaky RHEED of 1×2 surface reconstruction is observed, as shown in Figure 4.1. This indicates a poorer crystal quality compared to Sample D. Additionally, from the XRD results shown in Figure 4.3, both GeTe (222) and $Ge_{1-x}Mn_xTe$ (222) are observed and this is likely due to a higher Mn content (x ~0.8) which separate $Ge_{1-x}Mn_xTe$ from GeTe phase.

Higher T_s usually promotes a better crystalline growth as adatoms have sufficient mobility to rearrange themselves on the surface. Sample F was grown with similar condition as Sample D except for a higher T_s ~ 300 ˚C. The RHEED acquired similar patterns as that of Sample D for the first 5 mins of growth. However, the patterns changes to that observed in Figure 4.1, with both direction having similar streaky lines. This indicates good crystalline quality but the crystal structure differs from that of BaF_2 substrates. Figure 4.3 also shows the XRD pattern of Sample F which depicts a $Ge_{1-x}Mn_xTe$ (222) peak at a higher 2θ position than the rest of the samples. It is known that $Ge_{1-x}Mn_xTe$ with higher Mn composition shifts the 2θ position to a higher angle [4]. This means that the sample has a smaller lattice constant. This is confirmed with the XPS depth profile of Sample F as shown in Figure 4.4. The Mn composition of Sample D and F are estimated to be 0.30 and 0.97, respectively. The relatively high T_s value has greatly reduced the Ge composition leading to a high Mn composition and also a thinner sample. Thus the RHEED and XRD patterns of Sample F can be attributed to the Mn rich $Ge_{1-x}Mn_xTe$.

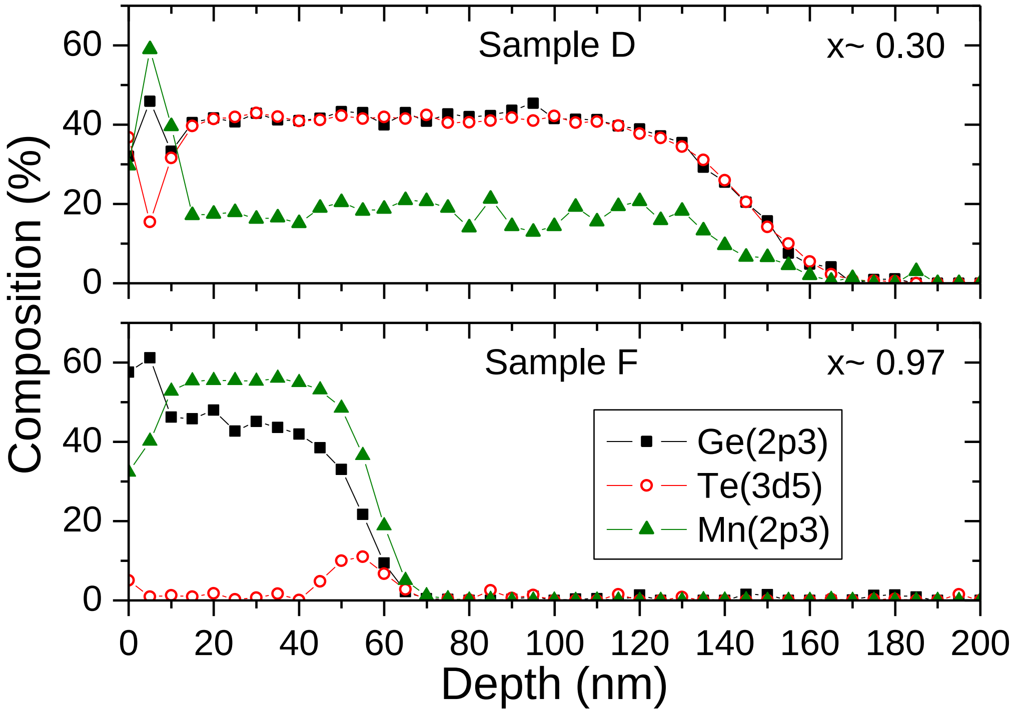

Figure 4.4 The XPS depth profile of Sample D and F with Mn composition (x) of 0.30 and 0.97, respectively.

Figure 4.5 shows the temperature dependence of field cooled magnetization (FC *M*-*T*) at 100 Oe for Sample A to F. Those samples with higher Mn composition, namely Sample C (x ~ 0.9), E (x ~ 0.8) and F (x ~ 0.97), show lower magnetization values and attain T_c ~ 90 K, 80 K and 100 K, respectively. This is likely to be attributed to antiferromagnetic superexchange between Mn ions which lowers T_c. An overview of the results is shown in Table 4.2. Further discussion of the exchange interaction in $Ge_{1-x}Mn_xTe$ will be discussed in Chapter 7.

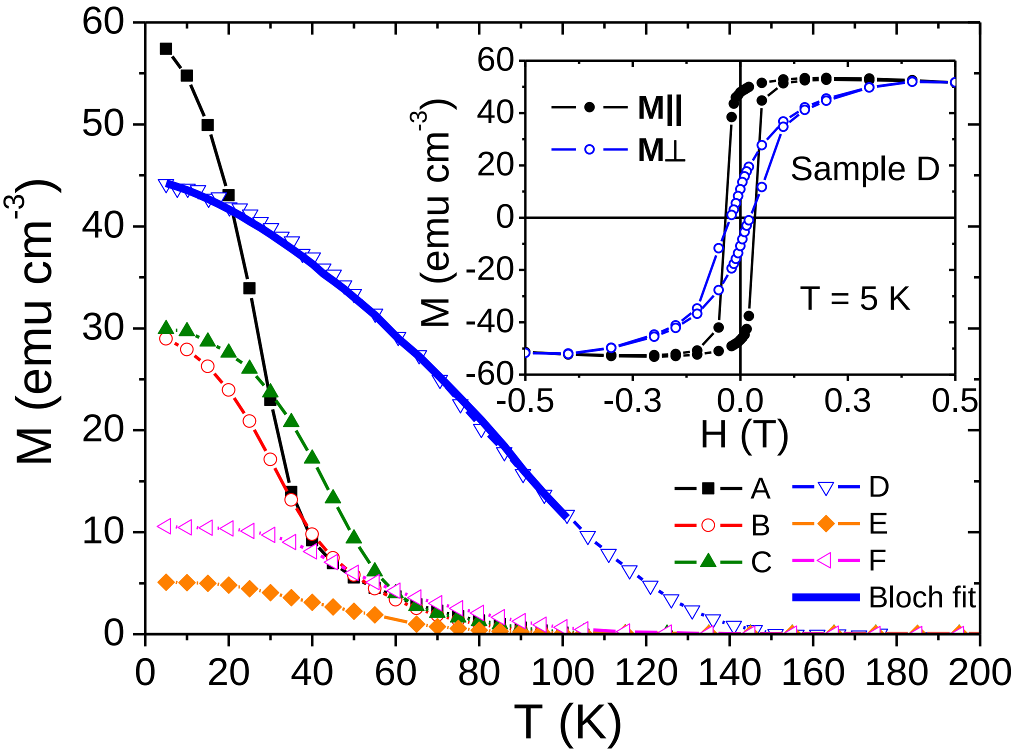

Figure 4.5 The temperature dependence of field cooled magnetization at 100 Oe for Sample A to F. The solid line is fitted to Bloch's law ($M \propto T^{3/2}$). The inset shows the hysteresis loops measured in-plane ($M_{\parallel}$) and out of plane ($M_{\perp}$) to the Sample D at 5 K.

Table 4.2 The T_c and saturation magnetization (M_s) of sample A to F, and their respective Mn compositions (x).

Sample	x	T_c/ K	M_s/ emu cm^{-3}
A	0.10	95	57.4
B	0.12	95	29.0
C	0.90	90	29.9
D	0.30	130	44.2
E	0.80	80	5.1
F	0.97	100	10.6

Similarly, those with low Mn composition, that is Sample A (x ~ 0.1) and B (x ~ 0.12), also give low T_c ~ 95 K. The FC M-T of Sample A is more of a concave trend. It was believed that this was due to disordering and also the presence of short and long range ferromagnetic phases in the sample. These will be further discussed in Chapter 5. The highest T_c ~ 130 K is attained for Sample D (x ~ 0.3). This T_c dependence of x is in agreement with those reported in Ref. [5], where the highest T_c is expected for x ~ 0.5. The FC M-T of Sample D can be fitted with the Bloch's law ($M \propto T^{3/2}$), which is usually expected for homogenous FMS. A clear magnetic anisotropy is shown in the inset of Figure 4.5 and the in-plane direction displays the easy magnetization axis.

4.3.2 Growth parameters influencing the physical and structural properties of $Ge_{1-x}Mn_xTe$ grown on GaAs.

In order to determine an optimum T_s for $Ge_{1-x}Mn_xTe$ on GaAs, a set of samples were grown at various T_s, ranging from 250 to 150 ˚C. The sources BEP, GeTe, Mn and Te were kept similar at 2.1×10^{-6}, 5.9×10^{-8} and 1.8×10^{-7} Torr, respectively. Figure 4.6 shows the RHEED patterns of GaAs after deoxidation at 580 ˚C and Te exchange, ZnTe after 1 hour of growth and samples after 2 hrs of growth at various substrate temperatures at azimuth $[0\bar{1}1]$ and [011]. Streaky RHEED patterns of GaAs were allowed to form before the ZnTe buffer layer was grown at 250 ˚C. A streaky RHEED of 1×2 surface reconstruction is observed for ZnTe which indicates good crystalline quality of the film. The zinc-blende structure of ZnTe with lattice constant ~ 6.0956 Å is confirmed by the XRD results as shown in Figure 4.7. The first sample was grown at T_s = 250 ˚C, following similar conditions as that for BaF_2 substrates. At the end of the growth, little changes were observed to the RHEED pattern except for a brighter spot patterns, indicating roughing of the surface, and a diminished intensity in the $[0\bar{1}1]$ and [011] direction, respectively. Additionally, the RHEED pattern differs from that observed for $Ge_{1-x}Mn_xTe$ grown on BaF_2.

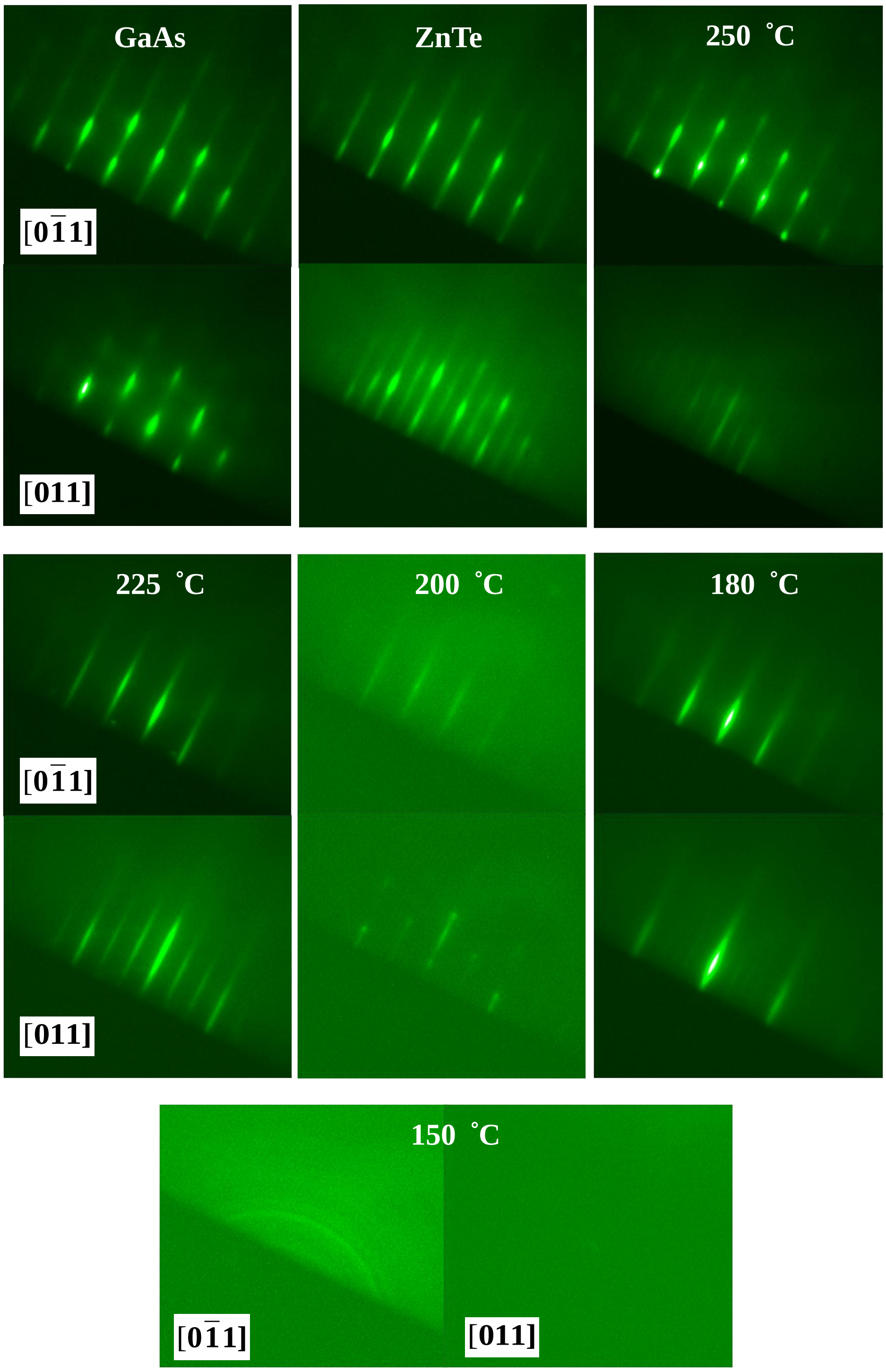

Figure 4.6 The RHEED patterns of GaAs after deoxidation and Te exchange, ZnTe after 1 hour of growth and samples after 2 hrs of growth at various substrate temperatures at azimuth $[0\bar{1}1]$ and [011].

These suggest that the grown film might not be $Ge_{1-x}Mn_xTe$. Subsequent samples were grown at lower temperatures and the RHEED patterns of those grown at T_s = 200 ˚C and T_s = 180 ˚C gave streaky lines similar to those $Ge_{1-x}Mn_xTe$ grown on BaF_2. Moreover, the 1×3 surface reconstruction for T_s = 180 ˚C suggests that the optimum T_s for good crystalline quality $Ge_{1-x}Mn_xTe$ growth on GaAs occurs at that temperature. Upon lowering the T_s to 150 ˚C, a diffuse ring RHEED pattern was observed and this indicates an amorphous film. Further structural analysis was carried out using the XRD 2θ scan.

Figure 4.7 shows the XRD 2θ patterns of the samples grown at T_s = 180 to 250 ˚C. The peaks corresponding to rock-salt GeTe (111) and GeTe (200) should occur at 25.78 ˚ and 29.86 ˚, respectively. As such, we would expect the peaks of rock-salt $Ge_{1-x}Mn_xTe$ to occur near these angles. At T_s = 225 and 250 ˚C, there are no obvious peaks corresponding to $Ge_{1-x}Mn_xTe$ and mainly hexagonal MnTe (002) and MnTe (101) peak are observed, respectively. These relatively high T_s do not seem to promote the surface adsorption of Ge. At a lower T_s = 200 ˚C, phases related to rock-salt $Ge_{1-x}Mn_xTe$ (111), hexagonal MnTe (002) and zinc-blende MnTe (200) can be observed.

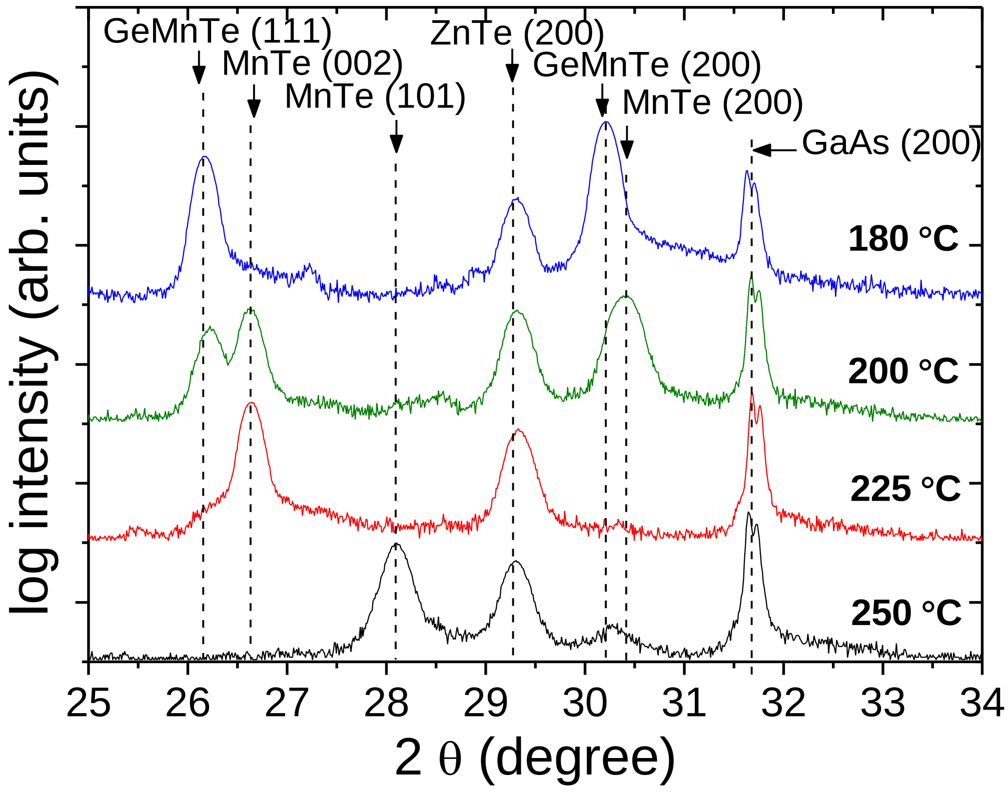

Figure 4.7 The XRD 2θ patterns of samples grown on GaAs at various T_s.

The occurrence of these phases is likely to result in the non-streaky and faint RHEED patterns seen in Figure 4.6. When T_s is lowered to 180 ˚C, only peaks corresponding to rock-salt $Ge_{1-x}Mn_xTe$ (111) and $Ge_{1-x}Mn_xTe$ (200) are observed. These relatively high peak intensity compared to that of substrate GaAs (200) also indicates a good crystalline film quality.

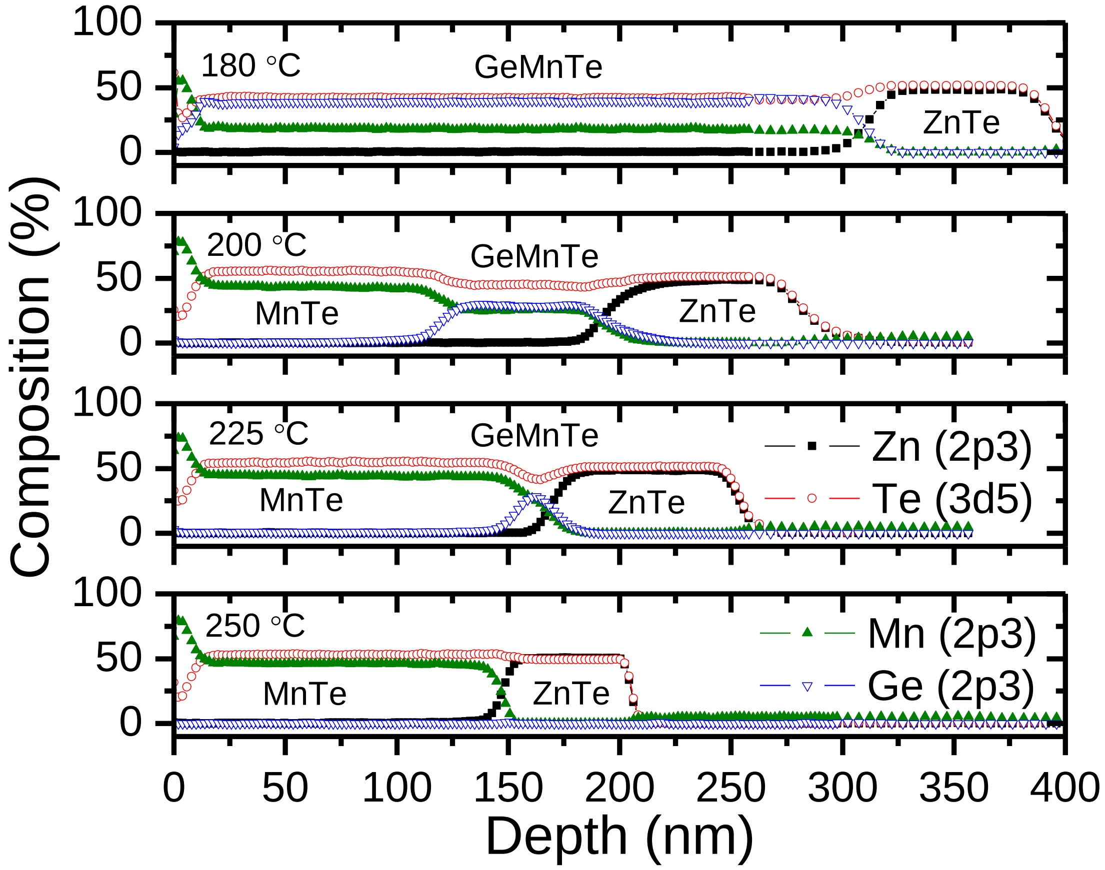

Figure 4.8 The XPS depth profile of samples grown on GaAs at various T_s.

Figure 4.8 shows the XPS depth profile of the samples grown at T_s = 180 to 250 ˚C. The results were consistent with those observed from XRD. The depth profile of the sample grown at T_s = 250 ˚C shows no Ge present in the film As T_s is reduced, Ge starts to adsorb and a thin layer of $Ge_{1-x}Mn_xTe$, not detectable by XRD, is observed for T_s = 225 ˚C. At T_s = 200 ˚C, two layers of MnTe and $Ge_{1-x}Mn_xTe$ is observed and can be distinguished from the XRD results. Further reduction in T_s to 180 ˚C promotes the formation of single $Ge_{1-x}Mn_xTe$ layer, albeit a two different crystallographic orientation. Thus, it can be concluded that T_s = 180 ˚C is suitable for $Ge_{1-x}Mn_xTe$ growth on GaAs. However further optimization of growth conditions is required to achieve single $Ge_{1-x}Mn_xTe$ with uniform crystallographic orientation.

Table 4.3 The Mn composition (x), root mean square (RMS) roughness and BEP of sources used for Samples G to L grown at T_s = 180 ˚C.

Sample	x	RMS (nm)	GeTe/ 10^{-6} Torr	Mn/ 10^{-8} Torr	Te/ 10^{-7} Torr
G	0.33	15.117	2.1	5.9	1.8
H	0.39	10.46	1	6.2	1.8
I	0.48	3.13	0.5	6.2	1.8
J	0.42	52.78	2.1	15	1.8
K	0.39	11.065	2.1	3.2	1.8
L	0.35	2.348	1	3.3	3

Six samples were grown at various GeTe, Te and Mn BEP at T_s = 180 ˚C. Table 4.3 shows the x, root mean square (RMS) roughness and BEP of sources used for these samples. The x and surface roughness ($10\,\mu\text{m} \times 10\,\mu\text{m}$) were determined using the XPS and AFM, respectively. Samples G, H and I were grown with decreasing GeTe flux, while as for samples K, G and J, an increasing Mn flux had been used to investigate the effects of GeTe and Mn flux, respectively.

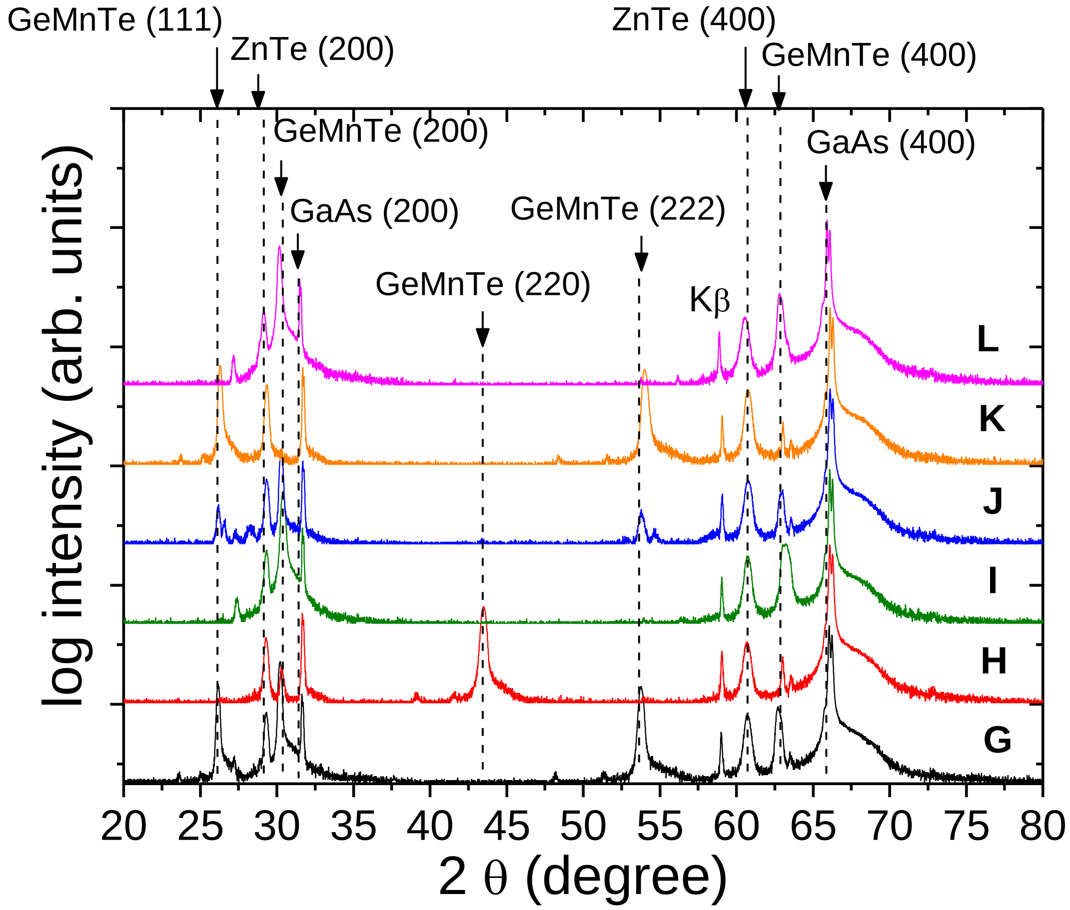

Figure 4.9 The XRD 2θ patterns of samples G to L.

Figure 4.9 shows the XRD results of these samples. The XRD peaks correspond to the layers of $Ge_{1-x}Mn_xTe$, ZnTe and GaAs. It can be observed that as GeTe flux decreases from Sample G to I, the crystallographic orientation of $Ge_{1-x}Mn_xTe$ changes from co-occurrence of rock-salt {111} and {200} planes (in Sample G), to {200} and{220} (in Sample H) and to a preferential {200} (in Sample I). This is due to the relative increase in Mn to Ge concentration in $Ge_{1-x}Mn_xTe$. Since MnTe would prefer a {200} orientation along GaAs {200}, a higher Mn concentrations promotes $Ge_{1-x}Mn_xTe$ {200} plane. On the other hand, as Mn flux decreases, the peaks of

$Ge_{1-x}Mn_xTe$ {111} becomes prominent (in Sample K and G), and eventually dominates over the {200} orientation (in Sample K). Thus, the XRD result of Sample K only shows peaks corresponding to $Ge_{1-x}Mn_xTe$ {111} plane.

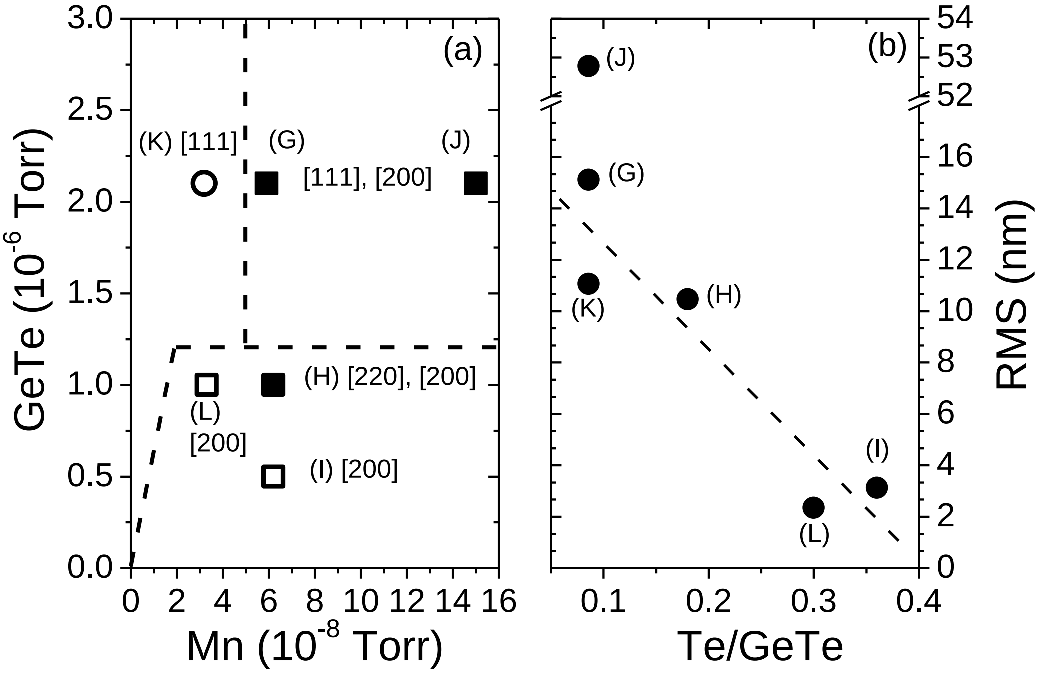

Figure 4.10 (a) The crystallographic orientations of $Ge_{1-x}Mn_xTe$ at various GeTe and Mn BEP. The open circle and square symbols indicate single phase of [111] and [200], respectively, while the solid symbols indicate the occurrence of multi-phases and (b) The RMS roughness as a function of Te/ GeTe ratio.

The dependence of $Ge_{1-x}Mn_xTe$ crystallographic orientation on GeTe and Mn fluxes is shown in Figure 4.10 (a). Essentially, a relatively low GeTe or Mn flux leads to single orientation of {200} or {111}, respectively. On the contrary, relatively high GeTe and Mn fluxes promote the formation of multi-phases. The effect of excess Te with respect to GeTe on the film surface roughness is shown in Figure 4.10 (b). A higher Te/GeTe ratio is found to give a smaller RMS value, which is important for multilayer growth involving $Ge_{1-x}Mn_xTe$. The excess Te flux provides a rich Te condition that ensures a zero net desorption of Te atoms from the $Ge_{1-x}Mn_xTe$ layer during growth. This smoothen the film surface. The RMS value of Sample J is large, probably due the use of high Mn flux under low excess Te flux condition.

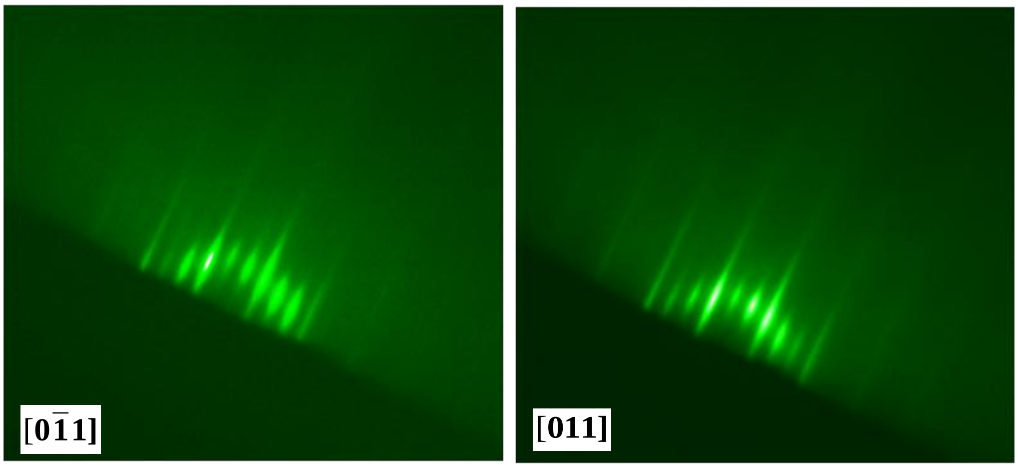

Figure 4.11 The 3×3 RHEED patterns of Sample L after 2 hrs of growth at T_s = 180 °C at azimuth $[0\bar{1}1]$ and [011].

Another sample (Sample L) was grown at low GeTe and Mn fluxes under high excess Te flux condition to induce a homogeneous film with low roughness. Figure 4.11 shows the streaky RHEED pattern of Sample L. The 3×3 surface reconstruction was maintained throughout the growth of the $Ge_{1-x}Mn_xTe$ indicating the good crystalline quality of the layer.

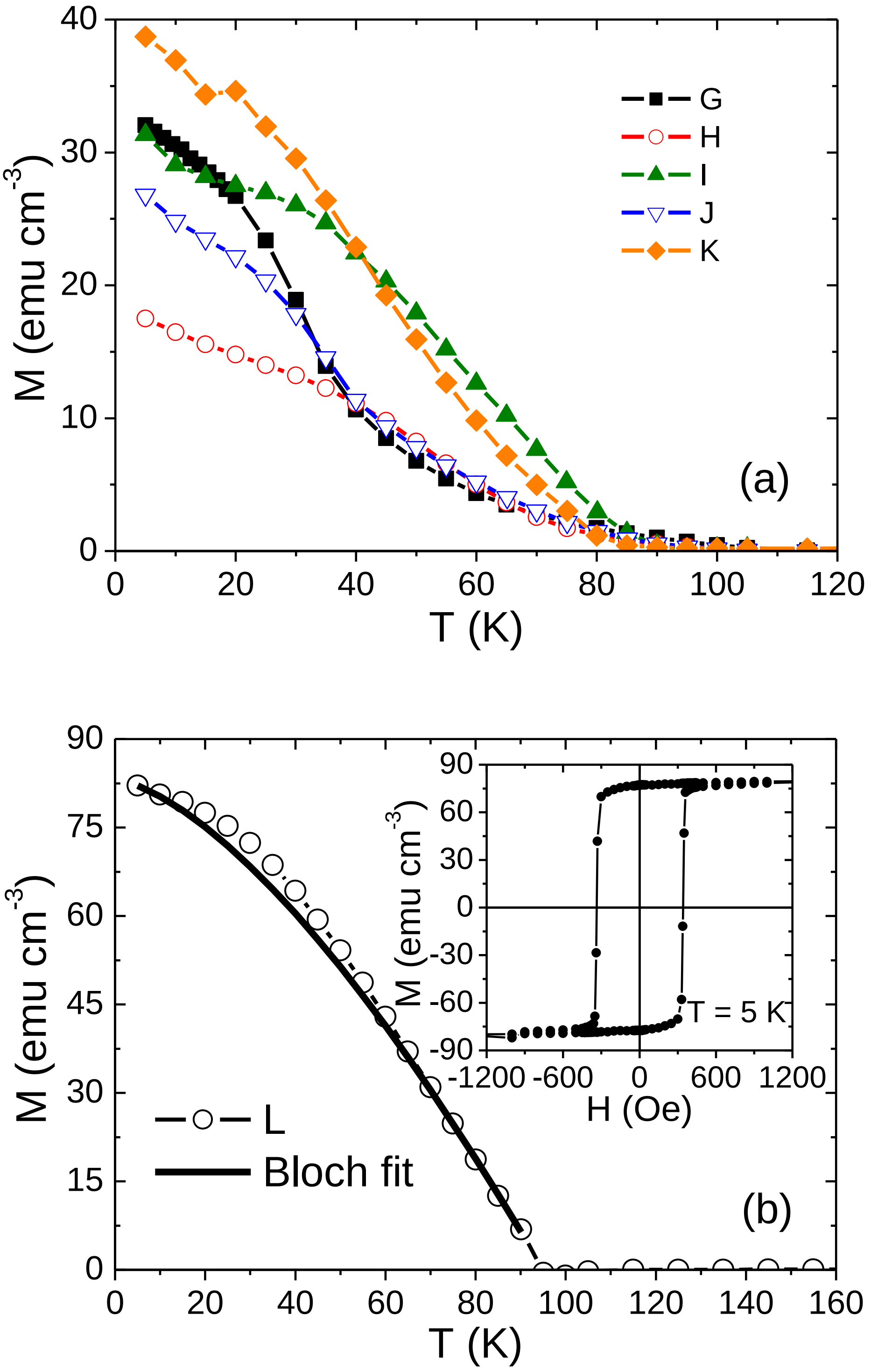

Figure 4.12 (a) The temperature dependence of remanent magnetization (M_r-T) of Sample G to K. (b) The M_r-T of Sample L. The solid line is fitted to Bloch's law ($M \propto T^{3/2}$). The inset shows the hysteresis loop measured in-plane to the Sample L at 5 K.

From the XRD result shown in Figure 4.9, Sample L consists of mainly peaks from $Ge_{1-x}Mn_xTe$ {200} and a low RMS value of 2.348 nm was achieved for this sample. A comparison of the samples remanent magnetization (M_r) as a function of temperature is shown in Figure 4.12.

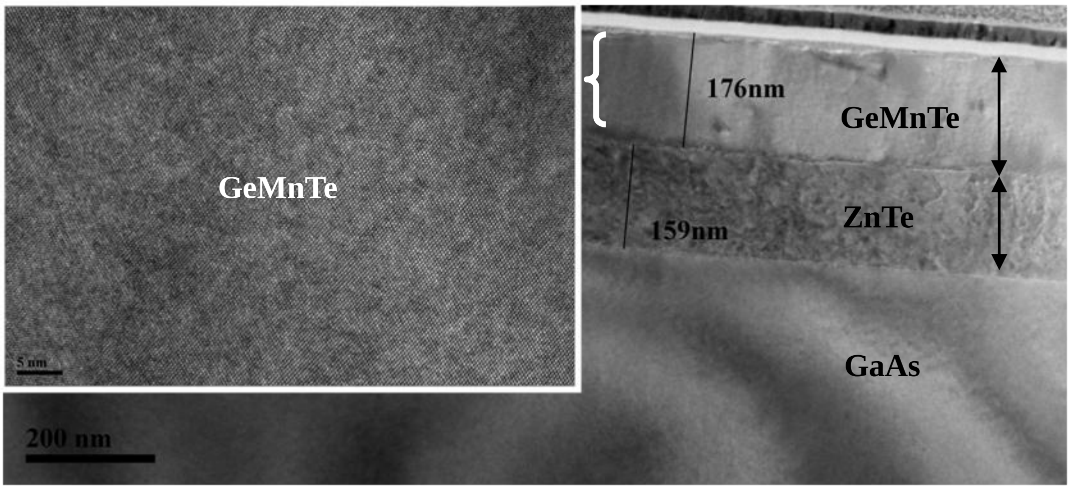

Figure 4.13 The cross-sectional TEM image of Sample L. The inset shows the magnified image of the $Ge_{1-x}Mn_xTe$ layer.

Owing to the similar x values of the samples, the T_c values are about $90 \pm 5\,\mathrm{K}$ and the highest M_r is attained for Sample L (T_c = 95 K). An overview of the results is shown in

Table **4.4**Table **4.2**.

Table 4.4 The T_c and saturation magnetization (M_s) of sample G to L and their respective Mn compositions (x).

Sample	x	T_c/ K	M_s/ emu cm^{-3}
G	0.33	95	32.0
H	0.39	95	26.8
I	0.48	90	31.3
J	0.42	95	26.8
K	0.39	85	38.7
L	0.35	95	82.1

The solid line in Figure 4.12 shows the good fit of Sample L M_r-T with the Bloch's law indicating a homogenous FMS. The hysteresis of Sample L measured at 5 K is shown in the inset of Figure 4.12. The homogeneity of the film and excess Te flux which promotes Ge vacancy leading to more hole carriers are likely to contribute to the high magnetization value. The good crystalline quality of Sample L is verified with TEM image as shown in Figure 4.13. The inset of Figure 4.13 shows the magnified image of the $Ge_{1-x}Mn_xTe$ layer. The interface between each layers are sharp and no other phases are observed from the TEM image.

4.4 Summary

The effects of various growth conditions, such as GeTe, Mn, Te fluxes and substrate temperatures on the physical properties of $Ge_{1-x}Mn_xTe$ grown using MBE on BaF_2 and GaAs substrates are discussed in this Chapter. While T_s of 250 ˚C is sufficiently low to grow $Ge_{1-x}Mn_xTe$ on BaF_2 substrates, lower T_s of 180 ˚C is preferred in the case of GaAs substrate so as to promote surface adsorption of Ge atoms. Under appropriate growth conditions homogeneous $Ge_{1-x}Mn_xTe$ has been achieved in both BaF_2 and GaAs substrates. Although excess Te flux improves the surface roughness and crystal quality of the film, excessive Te flux also results in separate phases of GeTe and $Ge_{1-x}Mn_xTe$. For films grown on GaAs, the use of a relatively low GeTe or Mn flux results in single crystallographic orientation of {200} or {111}, respectively. Collective evidences from streaky RHEED patterns, XRD peaks resulting only from uniformly oriented $Ge_{1-x}Mn_xTe$ planes, composition verification from XPS depth profile, good fitting of temperature dependence of magnetization to the Bloch's law as well as good film crystalline quality perceived from TEM imaging, are suggestive of the homogeneous $Ge_{1-x}Mn_xTe$ film grown in the absence of other phases.

Chapter 4 References

[1] L. Chen, S. Yan, P. F. Xu *et al.*, *Low-temperature magnetotransport behaviors of heavily Mn-doped (Ga, Mn)As films with high ferromagnetic transition temperature*, Appl. Phys. Lett. **95**, 182505 (2009).

[2] Y. Fukuma, H. Asada, S. Miyawaki *et al.*, *Carrier-induced ferromagnetism in* $Ge_{0.92}Mn_{0.08}Te$ *epilayers with a Curie temperature up to 190 K*, Appl. Phys. Lett. **93**, 252502 (2008).

[3] M. Hassan, G. Springholz, R. T. Lechner *et al.*, *Molecular beam epitaxy of single phase GeMnTe with high ferromagnetic transition temperature*, J. Cryst. Growth **323**, 363 (2011).

[4] J. F. Bi and K. L. Teo, *Nanoscale* $Ge_{1-x}Mn_xTe$ *ferromagnetic semiconductors*, in The Oxford Handbook of Nanoscience and Technology (Materials, Structures, Properties and Characterization Techniques, ed. By A. V. Narlikar and Y. Y. Fu, vol. II page 632 (2010).

[5] W. Q. Chen, K. L. Teo, M. B. A. Jalil *et al.*, *Compositional dependencies of ferromagnetic* $Ge_{1-x}Mn_xTe$ *grown by solid-source molecular-beam epitaxy*, J. Appl. Phys. **99**, 08D515 (2006).

CHAPTER 5

5. MAGNETISM AND MAGNETOTRANSPORT STUDIES IN $Ge_{1-x}Mn_xTe$

The previous Chapter focuses on the study of the effects of various growth conditions on the physical properties of $Ge_{1-x}Mn_xTe$ grown using the MBE system. The *M-T* curve of Sample A (see Figure 4.5) is not a Bloch-type, which is likely due to disordering and also presence of short and long range ferromagnetic phases in the sample. In this Chapter, we study the correlation between the magnetic and the transport properties in $Ge_{1-x}Mn_xTe$ ($x = 0.1$) (Sample A), which displays a concave *M-T* behavior. Our results show that the sample exhibits two ferromagnetic transition temperature at T_c = 34 K and T_c^* =100 K. We infer that T_c is a long range ferromagnetic ordering in view of sufficient carriers generating uniform ferromagnetism while T_c^* is a short range ferromagnetic ordering due to ferromagnetic clusters. The temperature dependence of the resistivity $\rho(T)$ curve exhibits a shallow minimum near T_c. The upturn of $\rho(T)$ towards the low temperature $(T < T_c)$ is well described by a weak-localization model while in the high temperature regime $(T > T_c)$, the phonon scattering dominates.

5.1 Introduction and Motivation

It has been a challenge to grow homogeneous ferromagnetic semiconductors epilayers and with high T_c. In widely studied $Ga_{1-x}Mn_xAs$, the nominal Mn concentration has been below 8% as higher concentration can lead to clusters and increase in interstitial Mn which suppress magnetization [1]. The formation clusters is often observed in semiconductors doped with transition metals, such as $Zn_{1-x}Cr_xTe$, $Zn_{1-x}Co_xO$ and $Ge_{1-x}Mn_x$. A recent review by Bonanni and Dietl, gives a comprehensive study of these condensed magnetic semiconductors in the host matrix which can give high spin order temperature [2]. These condensed magnetic semiconductors or clusters can be in the form of observable secondary phases or regions of subtle spinodal decomposition. The high quality of these epilayers is highly dependent on the growth conditions. In IV-VI ferromagnetic semiconductor such as $Ge_{1-x}Mn_xTe$, two different growth conditions with the same Mn concentration of 8% can lead to different magnetic properties and Curie temperatures [3]. The temperature dependence of magnetization (M-T) had shown one with concave and other with convex behavior, which was suggested to have a short range and long range ferromagnetism, respectively.

In this Chapter, we investigate the ferromagnetism and transport properties in degenerate $Ge_{1-x}Mn_xTe$ (x = 0.1) with a concave M-T behavior. Two magnetic transition temperature T_c and T_c^* have been observed in our sample. We explained our results based on the detailed analysis of the temperature dependence of the resistivity curve, ac susceptibility measurement, magnetization curve and anomalous Hall effect.

5.2 Results and Discussion

5.2.1 Structural, magnetic and transport properties of $Ge_{0.9}Mn_{0.1}Te$.

The RHEED pattern during the growth of $Ge_{0.9}Mn_{0.1}Te$ (Sample A) is shown in Figure 5.1 (a). The spotty pattern with faint lines indicates SK growth mode which forms both 2D and 3D island growth.

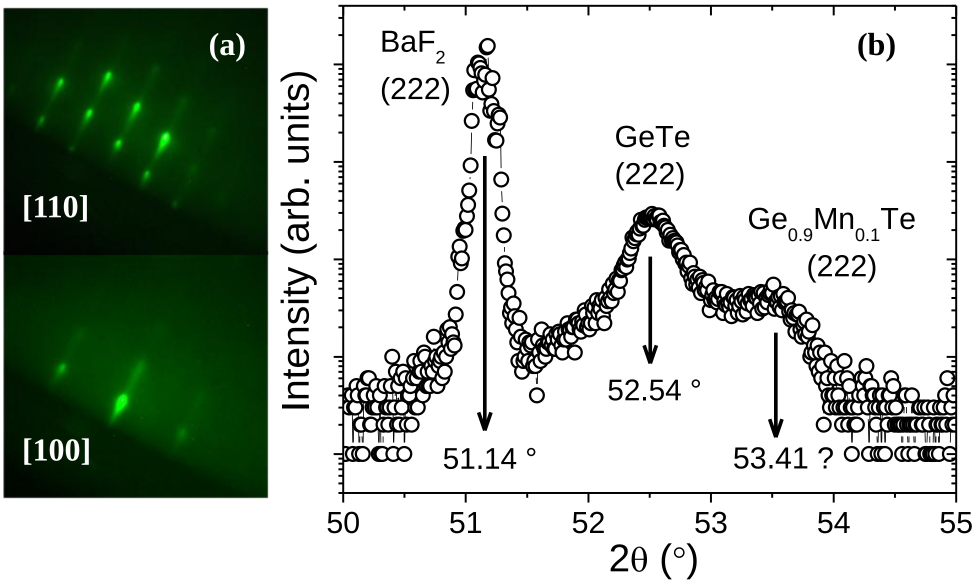

Figure 5.1 (a) The RHEED pattern of $Ge_{0.9}Mn_{0.1}Te$ after 2 hrs of growth at azimuth [110] and [100]. (b) The XRD pattern of $Ge_{0.9}Mn_{0.1}Te$.

Figure 5.1 (b) shows the XRD pattern of $Ge_{0.9}Mn_{0.1}Te$. The BaF_2 (222), GeTe (222) and $Ge_{0.9}Mn_{0.1}Te$ (222) peaks are well resolved. The lattice constant of $Ge_{0.9}Mn_{0.1}Te$ is estimated to be 0.596 nm.

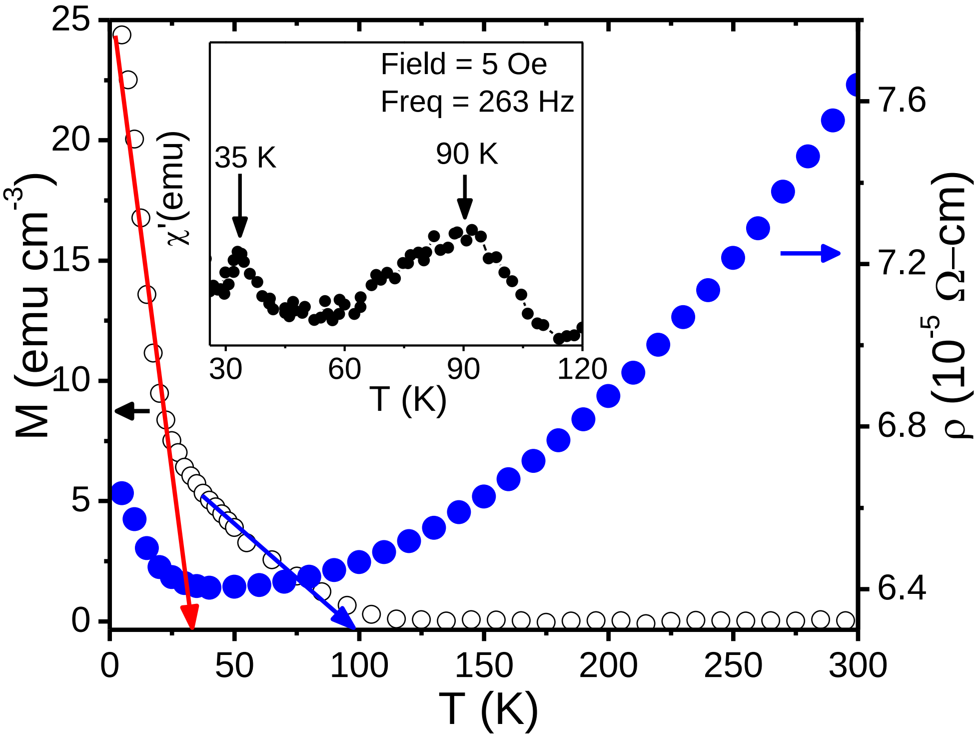

Figure 5.2 Temperature dependence of resistivity ($\rho(T)$) and field-cooled magnetization ($M(T)$) at 100 Oe for $Ge_{0.9}Mn_{0.1}Te$. The inset shows the temperature dependence of ac susceptibility measured at $H = 5$ Oe and a frequency of 283 Hz.

Figure 5.2 shows the temperature dependence of the resistivity $\rho(T)$ and field-cooled magnetization $M(T)$ at 100 Oe for the $Ge_{0.9}Mn_{0.1}Te$ sample. The shape of the $M(T)$ curve is more of a concave type, which deviates from the mean-field theory. This effect can be attributed to disordering effect present in the sample. We observed two kinks on the $M(T)$ curve. By extrapolating from the point of inflection, the $M(T)$ curve gives rise to two Curie temperature $T_c = 34$ ± 5 K (red line) and T_c^* = 100 ± 5 K (blue line) on the horizontal-axis. Our $M(T)$ curve is very similar to the one reported by Fukuma *et al.* (see Fig. 2(c) of sample W060 in Ref. [3]). It has been suggested by Fukuma *et al.* that concave $M(T)$ behavior observed for their W060 sample is due to short-range ferromagnetic order as there is not enough hole concentration to generate a uniform ferromagnetism. To further ascertain the origin of ferromagnetism, we performed the temperature dependence of ac susceptibility (χ) on our sample. The inset of Figure 5.2 shows the real part of the χ measured with ac magnetic field amplitude of 5 Oe at a frequency of 283 Hz. The occurrence of the two peaks at 35 K and 90 K correspond well to the T_c and T_c^* of the $M(T)$ curve, respectively.

A shallow minimum ρ_M in $\rho(T)$ is observed at $T_R = 34 \pm 5$K. The T_R is known to correlate directly with the T_c for different Mn composition [4]. Comparing to (Ga,Mn)As, a resistance maximum near T_c is usually observed [5]. It has been reasoned that the presence of randomly oriented ferromagnetic bubbles give rise to potential barriers that reduce the conductivity and also provide efficient spin-disorder scattering of the carriers. Both effects vanish when the system goes deeply into metallic and isolating phases [6]. According to the Mott's criterion, the critical concentration (p_c) for the metal-insulator transition (MIT) is given as $p_c^{1/3} a_H \approx 0.25$, where a_H is the Bohr radius. Our obtained carrier concentration is $p_o \sim 1.3\times10^{21}\,\mathrm{cm}^{-3}$ > $p_c \sim 4\times10^{18}\,\mathrm{cm}^{-3}$ indicating that the sample is deep in the metallic region. It is noteworthy that the upturn of $\rho(T)$ towards low temperatures ($T < T_R$) can be fitted using the function $\rho \propto \alpha \ln T$ (Kondo effect), $\rho \propto \exp(\alpha T^{-1/4})$ (variable range hopping {VRH}) and $\rho \propto \exp(\alpha T^{-1/2})$ (weak localization model). However, VRH is unlikely in view of the large dielectric constant (ε =36) that would screen the impurity ions. On the other hand, it is known that carrier spin polarization destroys the Kondo effect. Actually, this upturn of resistivity is more appropriate to be explained in terms of quantum corrections to the conductivity in the weakly localized regime for the spin-polarized universality class as extensively discussed in Ref. [6].

Figure 5.3 presents the temperature dependence of conductivity $(\sigma = 1/\rho)$. In the high temperature regime (T >T_R), the σ can be fitted with a power law of $T^{-3/2}$ as shown in Figure 5.3 (a), which suggests that the phonon scattering plays the essential role. Below the temperature T_R, the σ can be least-square fitted with a weak localization model [7,8,9,10,11] of the form $\sigma = \sigma_o + mT^{1/2}$ where σ_o is the residual conductivity due to impurity scattering and m > 0 (see Figure 5.3 (b)). It is noteworthy that the applied field does not change the scattering mechanisms.

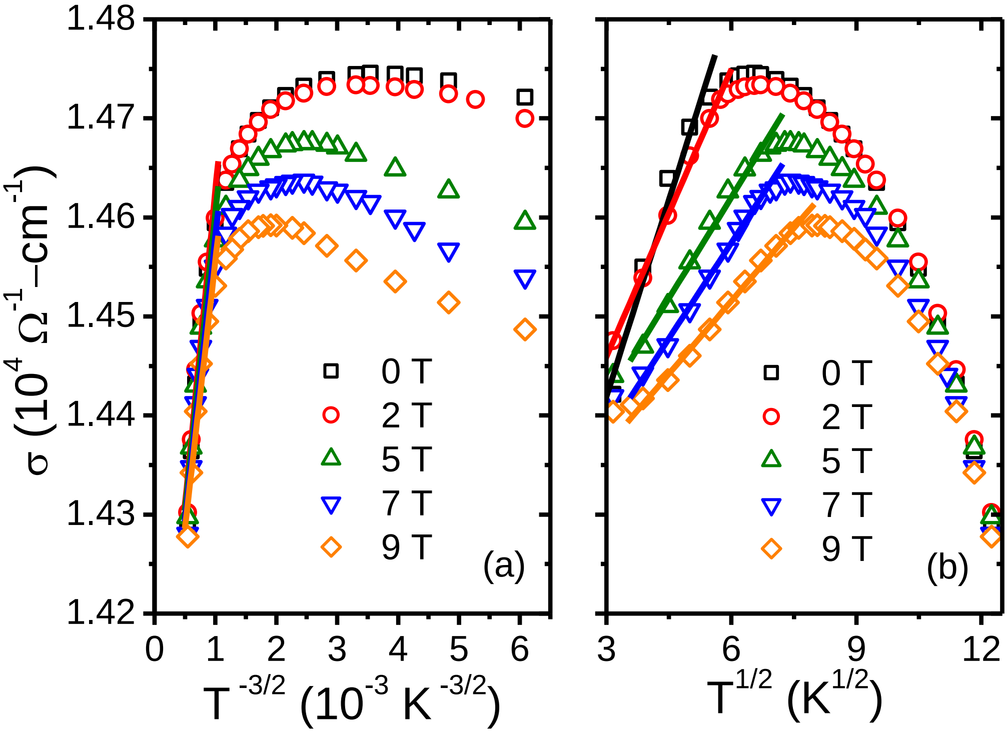

Figure 5.3 Conductivities ($\sigma(T)$) versus temperature with (a) $T^{-3/2}$ and (b) $T^{1/2}$ at various applied field with the solid lines fitted with the form of $T^{-3/2}$ and $T^{1/2}$, respectively.

5.2.2 Correlation between anormalous Hall effect and magnetization.

Figure 5.4 (a) shows the Hall resistivity ρ_{xy} plotted versus *H*, which displays as a sum of two components: $\rho_{xy} = R_o H + R_s M$ where R_o and R_s are the ordinary and anomalous Hall coefficients, respectively, *H* is the magnetic field and *M* is the magnetization. The R_s itself depends on the longitudinal resistivity as $R_s \sim c\rho_{xx}^n$, where n = 1 or 2 in the case of skew-scattering and side-jumping scattering, respectively and *c* is a constant.

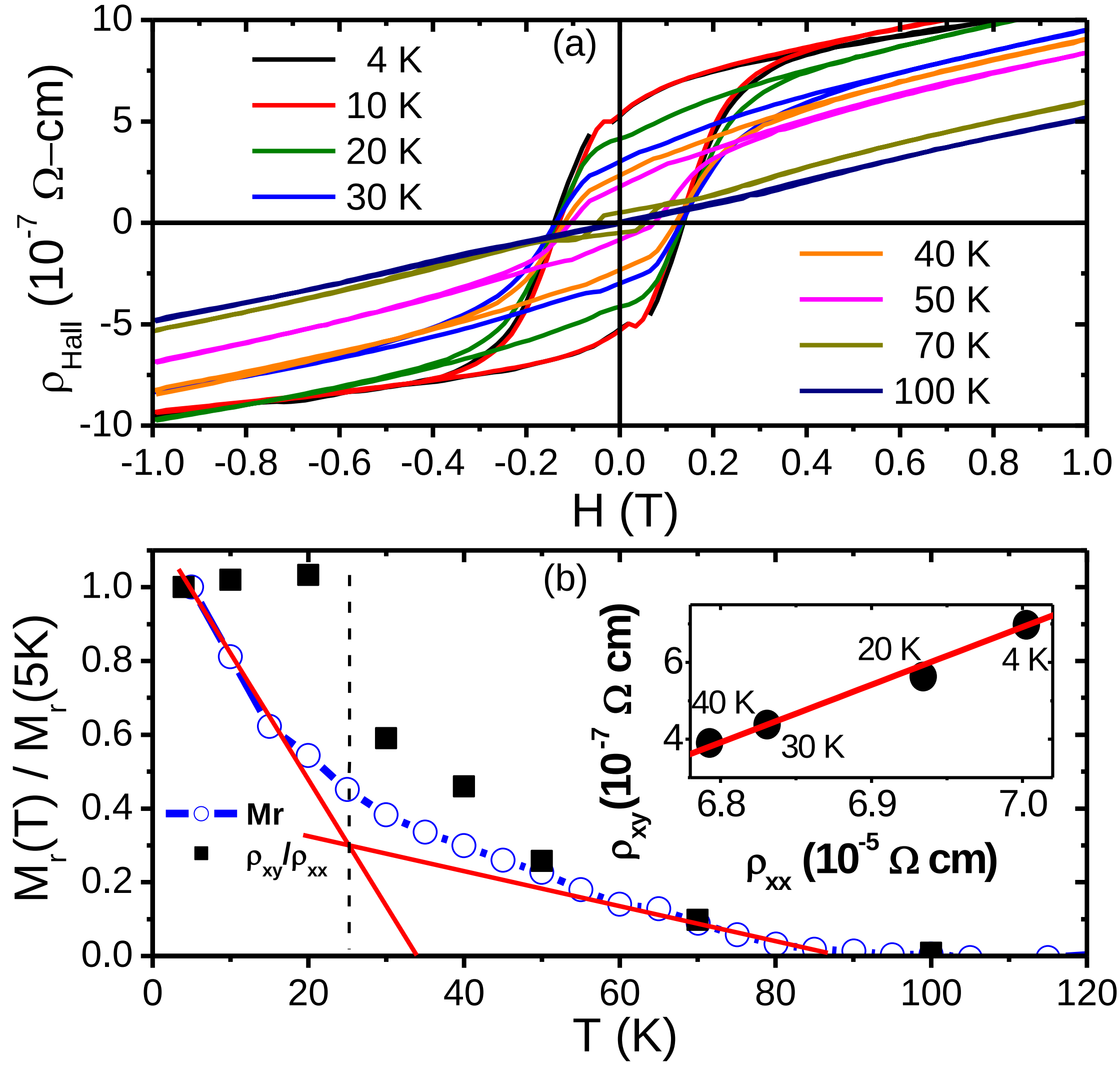

Figure 5.4 (a) Hall resistivity ρ_H versus H at various temperature and (b) the normalized temperature dependence of remanent magnetization $M_r(T)/M_r(5\text{K})$ and normalized [$\rho_{xy}/\rho_{xx}(H=0,T)$] / [$\rho_{xy}/\rho_{xx}(H=0,4\text{K})$]. The inset shows ρ_{xy} versus ρ_{xx} at fixed B = 1 T and varying T between 4 K and 40 K. The least square fit gives $\rho_{xy} \propto \rho_{xx}$.

The inset of Figure 5.4 (b) shows a linear scaling relationship between ρ_{xy} and ρ_{xx} by varying the temperature (4 K to 40 K) below the T_c [12], indicating that the skew-scattering is the dominant mechanism. By scaling M with $\frac{\rho_{xy}}{\rho_{xx}}$ [13], the ferromagnetic transition temperature can be determined from the temperature dependence of normalized $\frac{\rho_{xy}}{\rho_{xx}}$ as a function of temperature as shown in Figure 5.4 (b). We observe the behavior of $\frac{\rho_{xy}}{\rho_{xx}}$ correlates well with that obtained from the normalized remanent magnetization ($M_r(T)/M_r(5K)$) in the high temperature region. Below the critical temperature at 25 ± 5 K, defined by the cross point of the slopes at low and high temperature regions, the $\frac{\rho_{xy}}{\rho_{xx}}$ increases sharply and level off at the low temperature. This might suggest that there may be additional spin polarized current is provided at T < 25 ± 5K, leading to the enhancement of magnetic coupling that can arise from the long range ferromagnetic ordering.

Figure 5.5 (a) shows the normalized M-H loop measured by SQUID differs quite significantly from normalized ρ_{xy}-H loop. In general, the magnetization measured by SQUID can be different from ρ_{xy} as the latter is mainly due to the contribution of spin conductivity in carrier-rich regions while in the former case, spin localized in isolated clusters can also contribute to the magnetization but not to the Hall data [14]. Both coercive fields obtained from the M-H and ρ_{xy}-H loops display an enhancement at 30 K and go to zero at 100 K as shown in Figure 5.5 (b). Usually, in a homogenous ferromagnet, we would expect the coercive field to decrease with increasing temperature due to thermal fluctuations. In our sample, the enhancement of coercive field at 30 K could suggest the emergence of a soft magnetic phase at $T \leq 30\,\mathrm{K}$, which interacts and coupled with the other magnetic phase formed at 100 K [15].

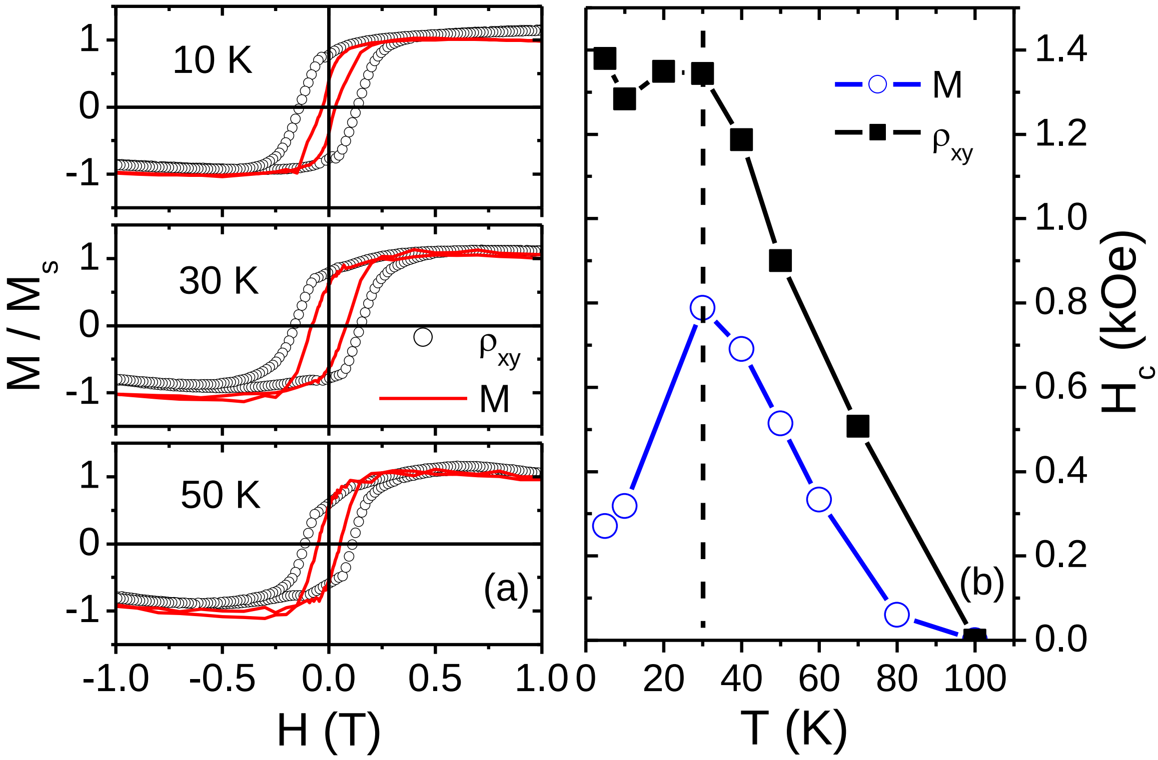

Figure 5.5 (a) Normalized magnetization M/ M_s -H and ρ_{xy} / ρ_{xy}(1T) - H loops at T = 10, 30 and 50 K and (b) the temperature dependence of coercive field from magnetization and Hall measurements.

The soft magnetic phase can be attributed to the formation of a uniform ferromagnetism where its spins can rotate coherently. The high temperature magnetic phase can exhibit larger coercvity due to spin pinning at isolated ferromagnetic clusters. Thus, we infer that T_c^* is due to short range ferromagnetic order in view of insufficient carriers to generate uniform ferromagnetism that leads to ferromagnetic clusters while T_c is ascribed to a long range ferromagnetic order.

5.3 Summary

Magnetotransport measurements were performed on $Ge_{0.9}Mn_{0.1}Te$ to study the correlation between the magnetic and the transport properties. It displays a concave *M-T* behaviour and two magnetic transition temperature can be observed from the magnetization and transport measurements where T_c = 34±5 K and T_c^* = 100±5 K. The T_R corresponding to the minimum in $\rho(T)$ is used as an indication of the T_c, which corresponds well with the extrapolation from the point of inflection of the *M(T)* curve. This minimum in $\rho(T)$ is likely to result from both the contribution of weak localization and phonon-scattering. The two magnetic transitions were further confirmed by the ac susceptibility measurement. A discrpency between the magnetization measured by SQUID and that estimated by Hall resistivity is due to the fact that the latter is mainly attributed to spin conductivity in carrier-rich regions while in the former case, spin localized in isolated clusters can also contribute to the magnetization but not to the Hall data. Thus, T_c^* can be inferred as short range ferromagnetic order due to insufficient carriers to generate uniform ferromagnetism that leads to ferromagnetic clusters while T_c is ascribed to a long range ferromagnetic order.

Chapter 5 References

[1] T. Jungwirth, J. Sinova, J. Mašek *et al.*, *Theory of ferromagnetic (III,Mn)V semiconductors*, Rev. Mod. Phys. **78**, 809 (2006).

[2] A. Bonanni and T. Dietl, *A story of high-temperature ferromagnetism in semiconductors*, Chem. Soc. Rev. **39**, 528 (2010).

[3] Y. Fukuma, H. Asada, S. Miyawaki *et al.*, *Carrier-induced ferromagnetism in* $Ge_{0.92}Mn_{0.08}Te$ *epilayers with a Curie temperature up to 190 K*, Appl. Phys. Lett. **93**, 252502 (2008).

[4] W. Q. Chen, S. T. Lim, C. H. Sim *et al.*, *Optical, magnetic, and transport behaviors of* $Ge_{1-x}Mn_xTe$ *ferromagnetic semiconductors grown by molecular-beam epitaxy*, J. Appl. Phys. **104**, 063912 (2008).

[5] F. Matsukura, H. Ohno, A. Shen *et al.*, *Transport properties and origin of ferromagnetism in (Ga,Mn)As*, Phys. Rev. B **57**, R2037 (1998).

[6] T. Dietl, *Interplay between Carrier Localization and Magnetism in Diluted Magnetic and Ferromagnetic Semiconductors*, J. Phys. Soc. Jpn. **77,** 031005 (2008).

[7] P. A. Lee, and T. V. Ramakrishnan, *Disordered electronic systems*, Rev. Mod. Phys. **57**, 287 (1985).

[8] B. L. Altshuler, and A. G. Aronov, *in Electron–Electron Interactions in Disordered Systems*, ed. A. L. Efros, and M. Pollak, **1** (North-Holland, Amsterdam, 1985).

[9] A. Prinz, G. Brunthaler, Y. Ueta *et al.*, *Electron localization in* $n\text{-}Pb_{1-x}Eu_xTe$, Phys. Rev. B **59**, 12983 (1999).

[10] F. Matsukura, M. Sawicki, T. Dietl *et al.*, *Magnetotransport properties of metallic (Ga,Mn)As films with compressive and tensile strain*, Physica E (Amsterdam) **21**, 1032 (2004).

[11] L. P. Rokhinson, Y. Lyanda-Geller, Z. Ge *et al.*, *Weak localization in* $Ga_{1-x}Mn_xAs$*: Evidence of impurity band transport*, Phys. Rev. B **76**, 161201 (R), (2007).

[12] K. W. Edmonds, R. P. Campion, K. Y. Wang *et al.*, *Magnetoresistance and Hall effect in the ferromagnetic semiconductor* $Ga_{1-x}Mn_xAs$, J. Appl. Phys. **93**, 6787 (2003).

[13] H. Ohno, *Making Nonmagnetic Semiconductors Ferromagnetic*, Science **281**, 951 (1998).

[14] Y. Pu, D. Chiba, F. Matsukura *et al.*, *Mott Relation for Anomalous Hall and Nernst Effects in* $Ga_{1-x}Mn_xAs$ *Ferromagnetic Semiconductors*, Phys. Rev. Lett. **101**, 117208 (2008).

[15] A. Hernando, P. Marín, and M. Vázquez, *Thermal dependence of coercivity in soft magnetic nanocrystals*, Phys. Rev. B **58**, 366 (1998).

CHAPTER 6

6. EFFECT OF HYDROSTATIC PRESSURE IN DEGENERATE $Ge_{1-x}Mn_xTe$

In the previous Chapter, we have studied the correlation between the magnetic and the transport properties in $Ge_{1-x}Mn_xTe$ ($x = 0.1$) (Sample A). In this Chapter, we explore the effect of hydrostatic pressure on the T_c of $Ge_{1-x}Mn_xTe$. The effect of hydrostatic pressure was utilized to investigate the magnetotransport properties of $Ge_{1-x}Mn_xTe$ ($x = 0.1$) (Sample A). The Curie temperature (T_c) was found to increase with pressure (P): $\frac{dT_c}{dP} = 0.27\,\text{K/kbar}$ which can be understood on the basis of the RKKY interaction mechanism. For sufficiently high carrier concentration of $p_o \sim 10^{21}\,\text{cm}^{-3}$, both the light holes from the L valence-band (VB) and the heavy holes from the Σ of the VB contribute to the RKKY interaction. A negative magnetoresistance is observed at low temperature and is found to decrease with pressure.

6.1 Introduction and Motivation

Recent experiments on (In,Mn)Sb under hydrostatic pressure has clearly demonstrated an increase in carrier-mediated coupling , and thus an increase in its T_c, as the lattice parameter is reduced by the applied pressure [1]. Tuning the exchange coupling by this process increases the magnetization, and also induces the ferromagnetic (FM) phase in an initially paramagnetic alloy. On the other hand, a decrease in T_c with applied pressure has been observed in ferromagnetic $Sb_{2-x}V_xTe_3$ single crystals and the phenomenon was attributed to hole-mediated ferromagnetism within the RKKY model that includes the oscillatory nature of the indirect ion–ion interaction [2]. Interestingly, earlier work on pressure studies in PbMnSnTe by Suski *et al.* shows that the observed shift in T_c with pressure is due to the redistribution of carriers of the band structure [3].

In this Chapter, we have utilized the effect of hydrostatic pressure to investigate the magnetotransport properties in degenerate *p*-$Ge_{1-x}Mn_xTe$. It is well known that carriers in $Ge_{1-x}Mn_xTe$ are generated by metal sublattice vacancies and the RKKY indirect exchange interaction via free carriers is responsible for the formation of the FM phase. We seek to understand the factors that influence the RKKY interaction in $Ge_{1-x}Mn_xTe$ from the magnetotransport studies under the effect of hydrostatic pressure. A negative MR observed at low temperature is analysed using a weak localization model. The magnetotransport measurements were carried out by conventional four-probe dc method in an Oxford Spectromag SM400 system, which was custom-designed for hydrostatic pressure measurement using an easyCell30 module up to 20 kbar and in the temperature range 2-300K at applied field up to 7 Tesla. The pressure was determined *in-situ* using a calibrated manganin manometer and pentane mixture was used as the pressure transmitting medium. The detailed experimental procedures of the hydrostatic pressure and magnetotransport experiments are given in Chapter 3, Section 3.3.2.

6.2 Results and Discussion

6.2.1 Enhancement of T_c by hydrostatic pressure effect.

Figure 6.1 shows the temperature dependence of the resistivity $\rho(T)$ for $Ge_{0.9}Mn_{0.1}Te$ (Sample A) at various pressures. The magnetization $M(T)$ curve measured at ambient pressure is also depicted in the top panel. As discussed in Chapter 5, the T_c = 34 K is obtained at the point of inflection of $M(T)$ curve (solid blue line) under 100 Oe field applied parallel to the plane. The $M(T)$ curve which goes to zero at T_c^* ~ 100 K could possibly be originated from FM $Ge_{0.9}Mn_{0.1}Te$ clusters that give rise to magnetic short range ordering [4]. A shallow minimum ρ_M in $\rho(T)$ at $T_R = 34 \pm 10\,\mathrm{K}$ is observed at ambient pressure. It has been established in Chapter 5 that the T_R correlates directly with the long range FM ordering, T_c.

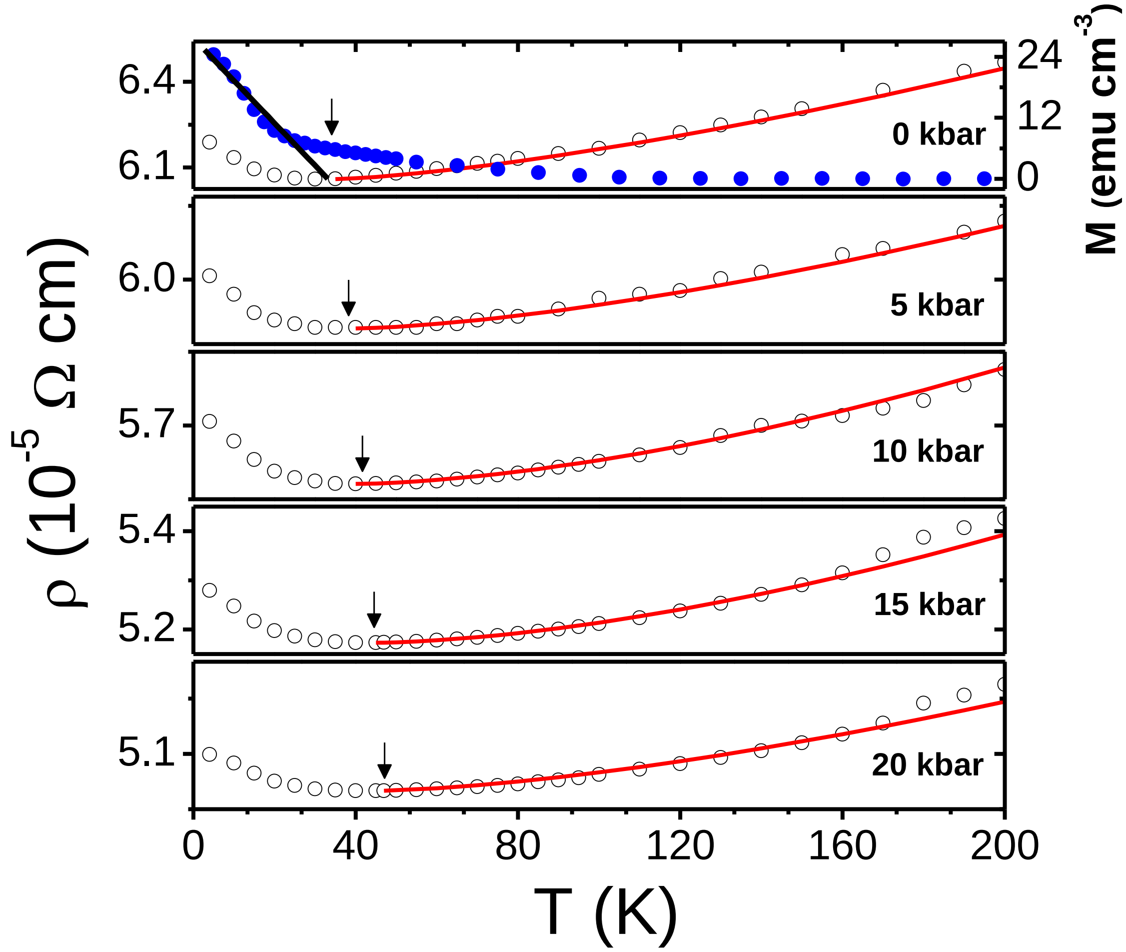

Figure 6.1 $\rho(T)$ measured at various applied pressures (open symbols) and the red solid lines are fitted to the form of $T^{1.5}$. The top panel displays the $M(T)$ curve measured with 100 Oe field at ambient pressure (solid symbols).

This indicates that the change of slope in ρ corresponds to PM-FM phase transition. The effect of an external pressure (P) on $\rho(T)$ has shifted T_R towards higher temperature (indicated by the arrows in Figure 6.1).

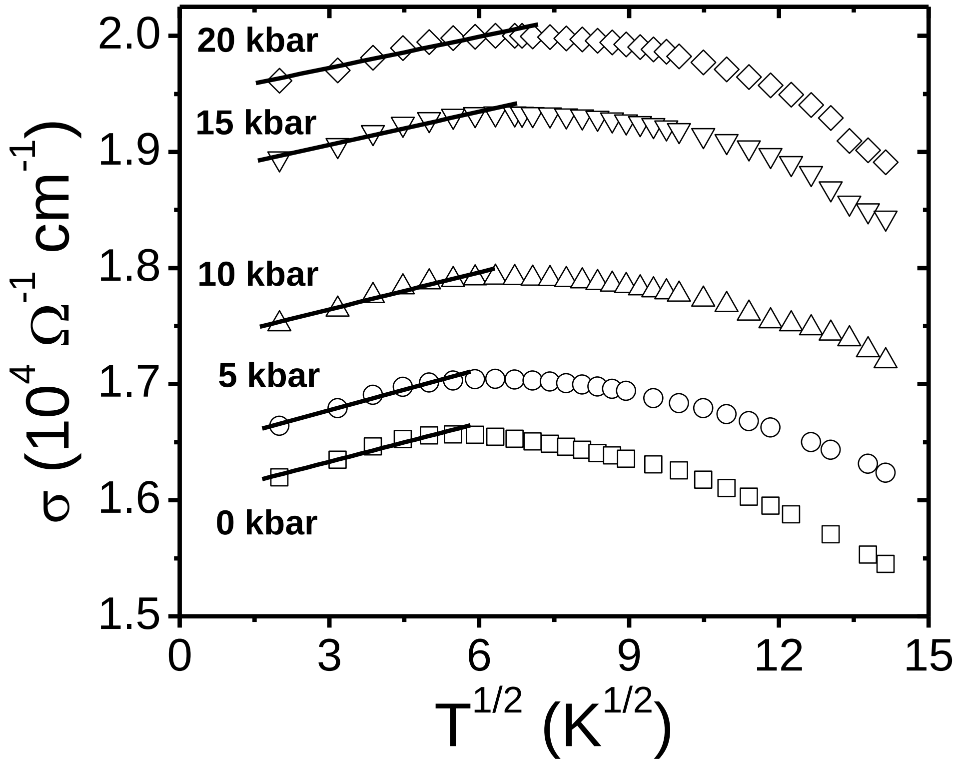

Figure 6.2 Conductivities ((σ)) versus $T^{1/2}$ for pressures. The solid lines are fitted to the to the form of $T^{0.5}$.

Figure 6.2 shows the low temperature conductivity ($\sigma = \frac{1}{\rho}$) is fitted with $\sigma = \sigma_o + mT^n$ at various pressure where σ_o is the residual conductivity due to impurity scattering and $m > 0$. The value of $n = 1/2$ gives the best least-square fit indicating that the electron-electron scattering dominates in the low temperature regime [5,6,7]. As the temperature is raised, the amount of scattering usually increases. In the high temperature regime, the ρ can be fitted with a power law of $\rho \propto T^n$ with $n = 1.5$ (red solid lines in Figure 6.1) which suggests that the phonon scattering plays the dominant role. It is noteworthy that the application of pressure does not affect the scattering mechanisms at low and high temperature regimes.

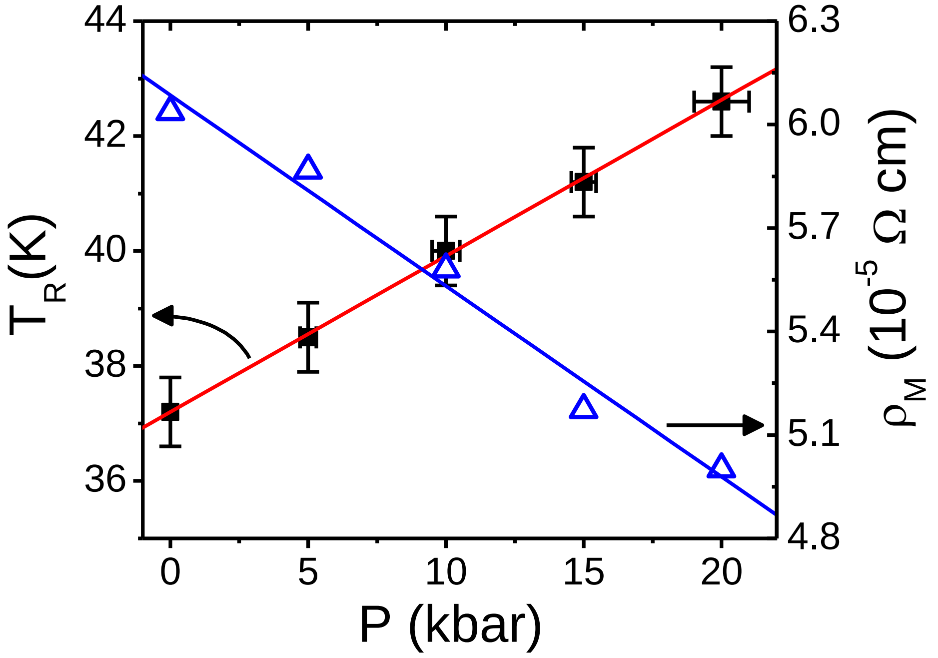

Figure 6.3 The shifts of T_R and ρ_M as functions of pressure (P).

Figure 6.3 displays a linear dependence of T_R on P with a slope of $\frac{dT_c}{dP} \approx \frac{dT_R}{dP} = 0.27$ K/kbar and a reduction in ρ. The decrease in ρ with P apparently indicates that the pressure enhances the carrier itinerancy or concentration. Our Hall measurement indicates that $p_o \sim 1.3 \times 10^{21}\ \mathrm{cm}^{-3}$ to be deep in the metallic region. In view of the contribution of the anomalous Hall effect in the Hall data, the normal Hall coefficient R_o is obtained in the linear, high field regime. We utilize the simple relation $\rho = \frac{1}{p_o q \mu}$, $\frac{d\rho}{dP} = -\left(\frac{1}{\mu q}\right)\left(\frac{1}{p_o}\right)^2\left(\frac{dp_o}{dP}\right)$ and by substituting our experimental result of $\frac{d\rho}{dP} = -5.5\times10^{-9}\ \Omega\text{m/kbar}$, we obtain $\frac{dp_o}{dP} = 11.4\times10^{-24}\,\text{m}^{-3}\text{/kbar}$. The increase in T_c with p_o, i.e. $\frac{dT_c}{dp_o}$ can be further inferred from the relation: $\frac{dT_c}{dp_o} = \frac{dT_c}{dP}/\frac{dp_o}{dP}$, giving $\frac{dT_c}{dp_o} = 2.36\times10^{22}\,\text{K/m}^{-3}$. Thus, the increase in T_c is likely a consequence of the increase in carrier concentration as a result of pressure effect.

6.2.2 Analysis of results using the RKKY, two valence band and weak localization models.

In IV-VI materials such as PbTe [8], SnTe [8] and GeTe [8,9], the band of light holes (lh) is located at the *L* point of the Brillouin zone and the band of heavy holes (hh) with its top located at the Σ point below the *L* band. The *L* and Σ bands have 4 and 12 equivalent energy valleys, respectively. Within the RKKY model and the mean field theory, the Curie temperature can be expressed as:

$$T_C = \frac{2xS(S+1)}{3k_B} I_{RKKY} \tag{6.1}$$

where S = 5/2 is the Mn spin, *x* is the Mn composition and I_{RKKY} is the total RKKY exchange integral which is the sum contributions from magnetic ions interacting with free hole carriers from the VB, i.e., $I_{RKKY} = \sum_n v_n I_n$, where *n* is the type of valley of the band and *v* is the number of equivalent energy bands in that valley. We take the band structure of $Ge_{1-x}Mn_xTe$ to be the same as GeTe assuming that the presence of Mn ions does not significantly alter the band structure. We first consider the case of a single VB model such that at high p_o, the Fermi level (E_F) lies inside the L band and only lh are involved in the interaction. Thus, the RKKY interaction can be expressed as [10,11],

$$I_{RKKY} = v_L I_L = v_L \left[\left(m^*\right) \left(\frac{a_o^2}{2^9 \pi^3 \hbar^2} \right) (2k_F a_o)^4 \right] J_{pd}^2 \sum_{ij} z_{ij} F\left(2k_F R_{ij}\right) e^{-R_{ij}/\lambda} \qquad (6.2)$$

where $m^* = 1.15 m_o$ is the lh effective hole mass, a_o = 5.967Å is the lattice constant, $k_F = \left(\frac{3\pi^2 p_o}{v_L} \right)^{1/3}$ is Fermi wave vector per one valley for a spherical Fermi surface with the number of equivalent energy valleys, $v_L = 4$ and p_o = 1.3 × 10^{-21} cm^{-3} is the carrier concentration, J_{pd} is the exchange integral between holes and Mn ions, $R_{ij} = a_o \sqrt{\frac{i}{2}}$ is the distance between Mn ion site i and j, z_{ij} is the number of nearest neighbors in the R_{ij} range, λ is the mean free paths of the carriers and $F\left(2k_F R_{ij}\right) = \left[\frac{\sin 2k_F R_{ij} - 2k_F R_{ij} \cos 2k_F R_{ij}}{\left(2k_F R_{ij}\right)^4} \right]$. We obtained J_{pd} ~216 meV and the enhancement in J_{pd} with pressure to be $\frac{dJ_{pd}}{dP} \approx 0.94\,\text{meV/kbar}$. We note that Fukuma *et al.* [12] has obtained a range of $J_{pd}\ (0.58 - 0.62\,\text{eV})$ values for different p_o and Mn composition by considering only a single valley (i.e., $v = 1$).

Next, we consider the case of two VB model such that at sufficiently high p_o, the E_F lies inside the L band as well as the Σ band. Thus, lh and hh can contribute to the RKKY interaction. This model also has been invoked to describe the transport, optical and magnetic properties of PbSnMnTe [10,11,13]. In the case of PbSnMnTe, the Σ

band is located 185 meV below the top of the L band. Ferromagnetic behavior was observed only when the p_o exceeded the threshold concentration of 3 × 10^{20} cm^{-3}, where sufficient carriers begin to fill up the Σ band. A schematic diagram of the two valence band structure is illustrated in Figure 6.4.

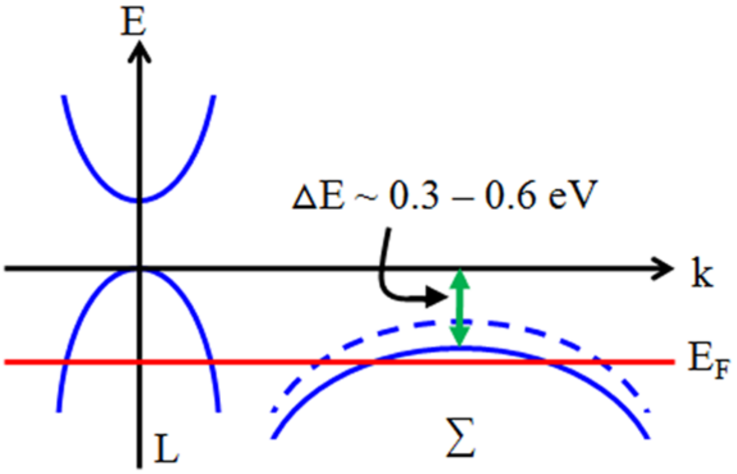

Figure 6.4 A schematic diagram of a two valance band structure. The dashed line represents the upward shift of the ∑ valence band as pressure increases.

It has been pointed out that due to the large effective mass of hh, the RKKY interaction is mostly mediated via carriers populating the Σ band. In the same vein, the increase in the p_o of $Ge_{0.9}Mn_{0.1}Te$ can be further analysed from the two VB model, which was proposed in the pressure studies of thermopower of GeTe [14]. Considering its band structure where the energy separation ΔE_v between the L and Σ bands is in the range of 0.3 ~ 0.6 eV. The carrier concentration is usually high such that the E_F is found in the L band. It has been pointed out that for $p_o \sim 10^{21}$ cm^{-3}, the E_F drops 0.6 eV below the L band, intersecting the Σ band in the absence of an applied pressure. With increasing pressure, the ΔE_v is diminished and the Σ band is successively promoted on the E_F level, thereby increasing p_o. The presence of more itinerant charge carriers could well enhance the RKKY interactions mechanism and hence increase the T_c. For $Ge_{0.9}Mn_{0.1}Te$ with p_o ~1.3 × 10^{21} cm^{-3}, we could expect that the lh from the L band and the hh from the Σ band both contribute to the RKKY interaction, i.e., $I_{RKKY} = 4I_L + 12I_\Sigma$. In this case, $p_o = p_L + p_\Sigma$ and the parameters of the subbands can be obtained from the results of Kolomoets *et al.* [15], where the lh and hh effective masses are $m_L{}^* = 1.15m_o$ and $m_\Sigma{}^* = 5m_o$ and $\frac{p_L}{p_\Sigma} = 3.6$. Using Eq. (6.1) and Eq. (6.2) and the respective band parameters, assuming the exchange integral is the same for both bands, the J_{pd} ~ 78 ± 5 meV at ambient pressure and $\frac{dJ_{pd}}{dP} \approx 0.19\,\text{meV/kbar}$. The smaller value, as compared to the case of only considering the L band, is due to the redistributions of carriers and more contribution to the RKKY interaction is attributed to the hh. Nevertheless, it is comparable to the corresponding value of 100 meV in (Pb, Sn, Mn)Te [10]. A $\frac{dT_c}{dP} \approx 0.098\,\text{K/kbar}$ is obtained for $p_o = 3.6 \times 10^{20}$ cm^{-3} in (Pb, Sn, Mn)Te [3], which is smaller than that in $Ge_{0.9}Mn_{0.1}Te$ (0.27 K/kbar). Correspondingly, a larger relative change of p_o with P is observed for $Ge_{0.9}Mn_{0.1}Te$ (0.86 %/kbar) than that for (Pb, Sn, Mn)Te (0.51 %/kbar). In the case of (Sb, V)Te material, the increase of p_o with P has led to a suppression of ferromagnetism which was attributed to a frustrated indirect coupling led by excess carrier concentrations [2]. The recent report by Fukuma *et al.* [16] has shown that the ferromagnetic ordering of $Ge_{1-x}Mn_xTe$ was found to increase with p_o up to 3.0×10^{21} cm^{-3}, after which it deceases with increasing p_o due to the similar effect. The frustration induced by RKKY oscillation is dominant when $\frac{p_o}{n_i}>>1$, where n_i is the impurity concentration [17]. In our case, the maximum p_o at 20 kbar is ~ 1.48×10^{21} cm^{-3}, and thus $\frac{p_o}{n_i}$ ~ 0.78 is less than unity. This explains the enhancement, instead of suppression, in T_c. On the other hand, there is no observation of change in p_o with P in (In, Mn)Sb while there is a slight decrease in p_o in the case of (Ga, Mn)As [18]. The T_c in thses materials were found to increase with P mainly due to the enhancement in J_{pd} and the band mass in according to the mean field model. It has also been found that in InSb:Mn that pressure induced an increase in the exchange splitting of the acceptor hole levels and a corresponding strong reduction in p_o [19].

Figure 6.5 shows the pressure (P) dependence of magnetoresistance (MR) at 4 K. We observed that the magnitude of the negative MR decreases with increasing P. We analysed the negative MR at various pressure at 4K by fitting it to a weak localization model proposed by Kawabata [20],

$$\frac{\Delta\rho}{\rho}\approx-\frac{\Delta\sigma}{\sigma}=-(\rho)\left(\frac{e^2}{2\pi^2\hbar}\right)\left(\frac{A}{l}\right)f(x)\ ; \qquad (6.3a)$$

$$f(x)=\sum_{N=0}^{\infty}\left\{2\left(\sqrt{N+1+x}-\sqrt{N+x}\right)-\frac{1}{\sqrt{N+1/2+x}}\right\}; \tag{6.3b}$$

$$x=\frac{\hbar}{eH}\left(\frac{1}{4}\right)\left(\frac{1}{L_{\Phi}^{2}}\right) \tag{6.3c}$$

where $l\left(=(\hbar/eH)^{1/2}\right)$ is the magnetic length and with the constant A and phase coherent length (L_{Φ}) are used as fitting parameters.

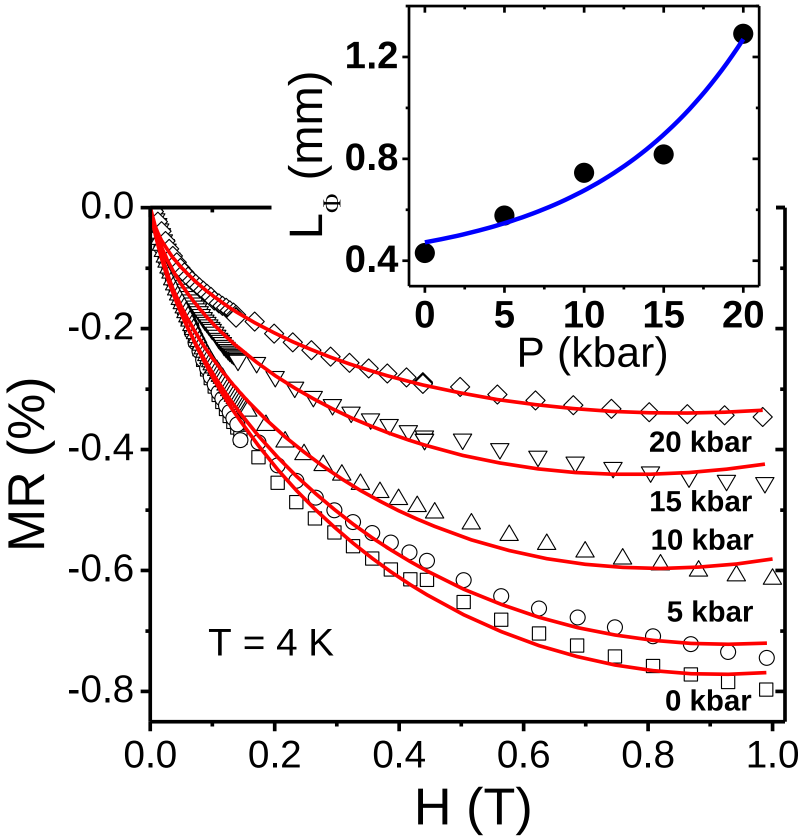

Figure 6.5 MR measured at various pressures at 4 K. The solid lines are fitted to Eq. (6.3a). The inset shows the L_{Φ} versus P.

It is noteworthy that weak localization has also been observed in other materials such as $Pb_{1-x}Eu_xTe$ [21] and (Ga,Mn)As [22,23]. Following Prinz *et al.* [21], a prefactor a of the positive MR $\Delta\rho = aH^2$ is also included as an adjustable parameter. The least-square fits to the MR curves are shown as solid lines for various P in Figure 6.5.

The inset shows the L_Φ as a function of P. As T_c increases with P, the magnetic fluctuation at low temperature is weakened, and this could lead to an increase in L_Φ with P. Further discussions on the type of scattering mechanism influencing L_Φ will be put forward in Chapter 8.

6.3 Summary

We have investigated the magneotransport properties of degenerate p-type $Ge_{1-x}Mn_xTe$ thin film with $x = 0.1$. The T_c is observed to increase with pressure mainly due to the increase in p_o responsible for the interactions between Mn ions. The RKKY and the two VB models are invoked to explain the results. The increase in p_o is still within the limit $\frac{p_o}{n_i} < 1$ where beyond which frustration induced by RKKY oscillation will dominant. Thus enhancement, instead of suppression, of T_c has been observed. The negative MR at low temperature can be attributed to the weak localization model and the extracted phase coherent length is found to increase with pressure.

Chapter 6 References

[1] M. Csontos, G. Mihály, B. Jankó *et al.*, *Pressure-induced ferromagnetism in (In,Mn)Sb dilute magnetic semiconductor*, Nat. Mater. **4**, 447 (2005).

[2] J. S. Dyck, T. J. Mitchell, A. J. Luciana *et al.*, *Significant suppression of ferromagnetism by hydrostatic pressure in the diluted magnetic semiconductor* $Sb_{2-x}V_xTe_3$ *with* $x<0.03$, Appl. Phys. Lett. **91**, 122506 (2007).

[3] T. Suski, J. Igalson, and T. Story, *Ferromagnetism of PbSnMnTe under high pressure*, J. Magn. Magn. Mater. **66**, 325 (1987).

[4] W. Q. Chen, S. T. Lim, C. H. Sim *et al.*, *Optical, magnetic, and transport behaviors of* $Ge_{1-x}Mn_xTe$ *ferromagnetic semiconductors grown by molecular-beam epitaxy*, J. Appl. Phys. **104**, 063912 (2008).

[5] P. A. Lee, and T. V. Ramakrishnan, *Disordered electronic systems*, Rev. Mod. Phys. **57**, 287 (1985).

[6] B. L. Altshuler, and A. G. Aronov, *in Electron–Electron Interactions in Disordered Systems*, ed. A. L. Efros, and M. Pollak, **1** (North-Holland, Amsterdam, 1985).

[7] T. Dietl, *Interplay between Carrier Localization and Magnetism in Diluted Magnetic and Ferromagnetic Semiconductors*, J. Phys. Soc. Jpn **77**, 031005 (2008).

[8] F. Herman, R. L. Kortum, I. B. Ortenburger *et al.*, *Relativistic band structure of GeTe, SnTe, PbTe, PbSe, and PbS*, J. Phys. Colloq. **29**, C4-62 (1968).

[9] J. E. Lewis, *Optical properties and energy gap of GeTe from reflectance studies*, Phys. Stat. Sol. (b) **59**, 367 (1973).

[10] T. Story, G. Karczewski, L. Świerkowski *et al.*, *Magnetism and band structure of the semimagnetic semiconductor Pb-Sn-Mn-Te*, Phys. Rev. B **42**, 10477 (1990).

[11] T. Story, P. J. T. Eggenkarnp, C. H. W. Swűste *et al.*, *Ruderman Kittel Kasuya Yosida exchange interaction in many-valley IV-VI semimagnetic semiconductors*, Phys. Rev. B **45**, 1660 (1992).

[12] Y. Fukuma, H. Asada, N. Nishimura *et al.*, *Ferromagnetic properties of IV-VI diluted magnetic semiconductor Ge1-xMnxTe films prepared by radio frequency sputtering*, J. Appl. Phys. **93,** 4034 (2003).

[13] H. J. M. Swagten, W. J. M. deJonge, R. R. Gałazka *et al.*, *Hole density and composition dependence of ferromagnetic ordering in Pb-Sn-Mn-Te*, Phys. Rev. B **37**, 9907 (1988).

[14] L. G. Khvostantsev, and V. A. Sidorov, *Thermoelectric properties of GeTe at high hydrostatic pressure up to 8.5 GPa and its valence-band structure*, Phys. Stat. Sol. (b) **116**, 83 (1983).

[15] N. V. Kolomoets, E. Ya. Lev, and L. M. Sysoeva, Sov. Phys. Sol. Stat. **6,** 551 (1964).

[16] Y. Fukuma, H. Asada, S. Miyawaki *et al.*, *Carrier-induced ferromagnetism in* $Ge_{0.92}Mn_{0.08}Te$ *epilayers with a Curie temperature up to 190 K*, Appl. Phys. Lett. **93**, 252502 (2008).

[17] S. Das Sarma, E. H. Hwang, and D. J. Priour, Jr., *Enhancing* T_c *in ferromagnetic semiconductors*, Phys. Rev. B **70**, 161203(R) (2004).

[18] M. Csontos, G. Mihály, B. Janko *et al.*, *Effect of hydrostatic pressure on the transport properties in magnetic semiconductors*, Phys. Stat. Sol. (c) **1**, 3571 (2004).

[19] J. Teubert, S. A. Obukhov, P. J. Klar *et al.*, *Influence of Magnetic Dopants on the Metal-Insulator Transition in Semiconductors*, Phys. Rev. Lett. **102**, 046404 (2009).

[20] A. Kawabata, *Theory of negative magnetoresistance in three-dimensional systems*, Solid State Commun. **34**, 431 (1980).

[21] A. Prinz, G. Brunthaler, Y. Ueta *et al.*, *Electron localization in* $n\text{-}Pb_{1-x}Eu_xTe$, Phys. Rev. B **59**, 12983 (1999).

[22] F. Matsukura, M. Sawicki, T. Dietl *et al.*, *Magnetotransport properties of metallic (Ga, Mn)As films with compressive and tensile strain*, Physica E **21**, 1032 (2004).

[23] L. P. Rokhinson, Y. Lyanda-Geller, Z. Ge *et al.*, *Weak localization in* $Ga_{1-x}Mn_xAs$*: Evidence of impurity band transport*, Phys. Rev. B **76**, 161201(R) (2007).

CHAPTER 7

7. EXCHANGE INTERACTION AND CURIE TEMPERATURE IN $Ge_{1-x}Mn_xTe$ FERROMAGNETIC SEMICONDUCTORS

In the previous Chapter, we have observed an enhancement of T_c in $Ge_{0.9}Mn_{0.1}Te$ with applied pressure up to 20 kbar. The pressure is not further increased due to the difficulty of maintaining good ohmic contact at higher pressure. This Chapter shows that the T_c can also be suppressed under high enough applied pressure which is attributed to the increase in antiferromagnetic superexchange between Mn ions. We present the magnetotransport studies of $Ge_{1-x}Mn_xTe$ (x = 0.3) (Sample D) under hydrostatic pressure. This sample is more homogenous than $Ge_{0.9}Mn_{0.1}Te$ (Sample A) as discussed in Chapter 4. The investigation of the normal and Hall resistivities provide an insight to the dependence of carrier concentration, mobility and magnetic properties on pressure. Our results reveal that the application of pressure changes the band structure which can be explained by a two valence band model as discussed in Chapter 6. We observe the enhancement and reduction of Curie temperature within a pressure range of 0 – 24 kbar. Analysis within the framework of the RKKY model allows us to identify the factors in controlling the T_c, in which the exchange interaction plays a predominant role in the formation of ferromagnetic phase.

7.1 Introduction and Motivation

The exchange coupling strength between local moments of magnetic ions and conduction carriers plays an important role in controlling the T_c in carrier-mediated FMS [1]. In contrast to the III-Mn-V FMS, the hole density and Mn ion concentration in IV-Mn-VI FMS such as $Ge_{1-x}Mn_xTe$ [2,3] can be controlled independently. It is well known that crystalline GeTe is a narrow band-gap (0.1 to 0.2 eV) degenerate semiconductor with a high intrinsic hole density (10^{20}-10^{21} cm^{-3}) due to native cation vacancies. The FM in $Ge_{1-x}Mn_xTe$ is then driven by the RKKY indirect exchange interaction between Mn ions via this high hole concentration. Recent progress in $Ge_{1-x}Mn_xTe$ grown by MBE shows that $T_c \sim 190$ K can be attained at Mn composition, $x \sim 10$ % [4] and T_c as high as 200 K at $x \sim 46$ % can also be achieved under appropriate growth conditions [5]. From the growth point of view, the x can be varied by controlling the stoichiometric composition via GeTe and Mn fluxes and the hole concentration can be changed by substrate temperature as well as Te flux. To achieve high T_c in $Ge_{1-x}Mn_xTe$, we need relatively high x as well as sufficient holes to mediate ferromagnetism between Mn ions. However, high x induces antiferromagnetic effect which reduces T_c. At the same time, high Te flux decreases carrier concentration and hence T_c, albeit the improvement of surface roughness. Additionally, growth conducted either at lower or higher substrate temperature will lead to precipitation of secondary phases or even phase separation [5]. As such, only a narrow window of growth conditions exists to achieve single phase $Ge_{1-x}Mn_xTe$.

In well studied III-V FMS such as (In,Mn)Sb and (Ga,Mn)As, hydrostatic pressure experiments have demonstrated that T_c can be enhanced by the exchange coupling strength [6,7] in which the exchange energy J_{pd} scales with the lattice constant (a_o^3) as $J_{pd} \propto a_o^3$ according to the Zener model [8]. At the same time, the pressure does not change the carrier concentration density {in (In,Mn)Sb)} or rather decreases it {in (Ga,Mn)As} [7]. On the other hand, the issue in achieving high T_c is more complicated in IV-Mn-VI FMS. The understanding in the interplay among factors that influences T_c is far from complete. In this Chapter, we present a detailed magnetotransport study in tuning the T_c in $Ge_{0.7}Mn_{0.3}Te$ by hydrostatic pressure. The enhancement and reduction of T_c is clearly observed within pressure range of 0 – 24 kbar. The study of Hall resistivity allows us to separate its normal and anomalous components. The application of pressure leads to a change in the bandstructure which affects directly the hole concentration. The behavior of carrier concentration and mobility as a function of pressure can be analyzed from the normal Hall resistivity and longitudinal resistivity while the magnetic properties are manifested in the anomalous Hall part. The factors that control the T_c are analyzed using RKKY model.

7.2 Results and Discussion

7.2.1 Tunning of T_c by hydrostatic pressure effect.

Figure 7.1 shows the temperature dependence of longitudinal resistivity $\rho_{xx}(T)$ and field-cooled magnetization $M(T)$ at 100 Oe applied parallel to the plane of $Ge_{0.7}Mn_{0.3}Te$ (Sample D).

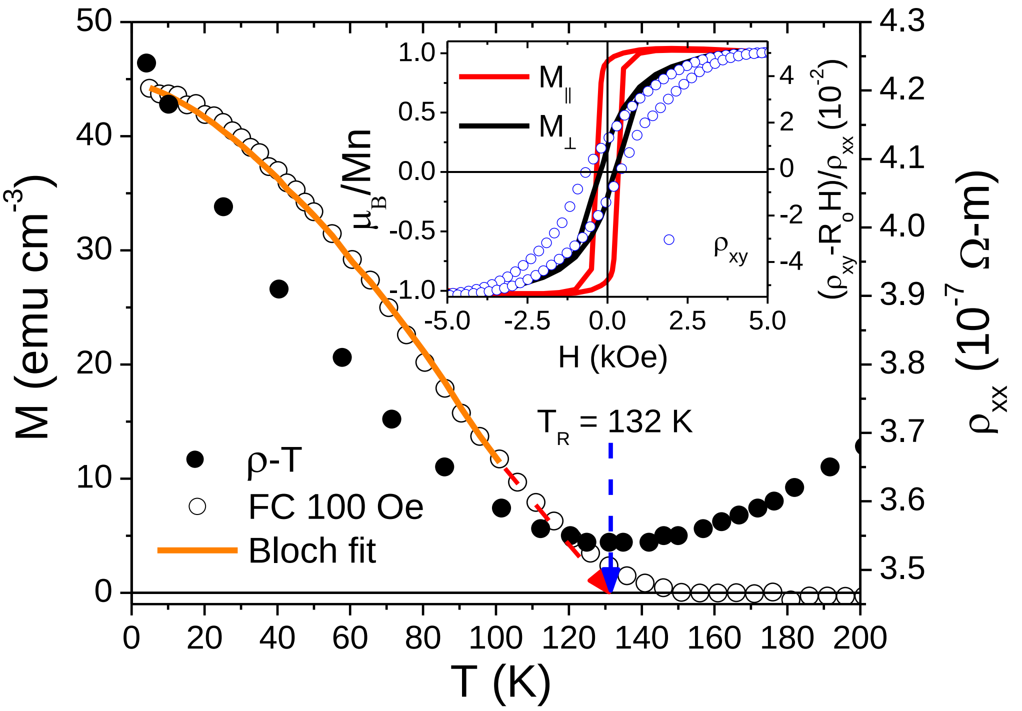

Figure 7.1 Temperature dependence of resistivity ($\rho_{xx}(T)$) and field-cooled magnetization at 100 Oe. The solid line is fitted to Bloch's law ($M \propto T^{3/2}$). The inset shows the hysteresis loops measured in-plane ($M_{\parallel}$) and out of plane ($M_{\perp}$) to the sample and the ρ_{xy} - H loop at 5 K.

As discussed in Chapter 4, the convex $M(T)$ is well fitted to the Bloch's law ($M \propto T^{3/2}$) which is usually expected for a homogenous FMS. The obtained T_c is 132

K, and agrees well with the temperature (T_R) where $\rho_{xx}(T)$ is at the minimum. In the previous Chapter, we have shown that the low ($T < T_R$) and high ($T > T_R$) temperature $\rho_{xx}(T)$ upturn can be ascribed to electron-electron scattering ($\sigma \propto T^{1/2}$) and phonon scattering ($\sigma \propto T^{-3/2}$), respectively [9]. A clear magnetic anisotropy is shown in the inset of Figure 7.1. The in-plane direction displays the easy magnetization axis and the saturation magnetization per Mn ion is measured to be ~1 μ_B/Mn at 4 K.

The magnetization properties can also be attained from the Hall resistivity ($\rho_{xy}(H)$) [10] as $M = \frac{\rho_{xy} - R_o H}{c\rho_{xx}^{\ n}}$ where R_o is the ordinary Hall coefficients, H is the magnetic field, M is the magnetization, ρ_{xx} is the longitudinal resistivity and c is a constant. We have set $n = 1$ in the case of skew-scattering. Figure 7.1 shows the M-H loop measured by SQUID resembles quite closely to that of ρ_{xy} - H loop. In (In,Mn)Sb, the anomalous part of the AHE is not proportional to the magnetization but depends on field due to Berry-phase effect [11]. In our case, the anomalous part of AHE changes with pressure. The ordinary Hall coefficient $\left(R_o\right)$ was determined from the slope of AHE $\left(\left.\frac{d\rho_{xy}}{dH}\right|_{H>1T}\right)$ in the high magnetic field region where the ordinary Hall effect dominates.

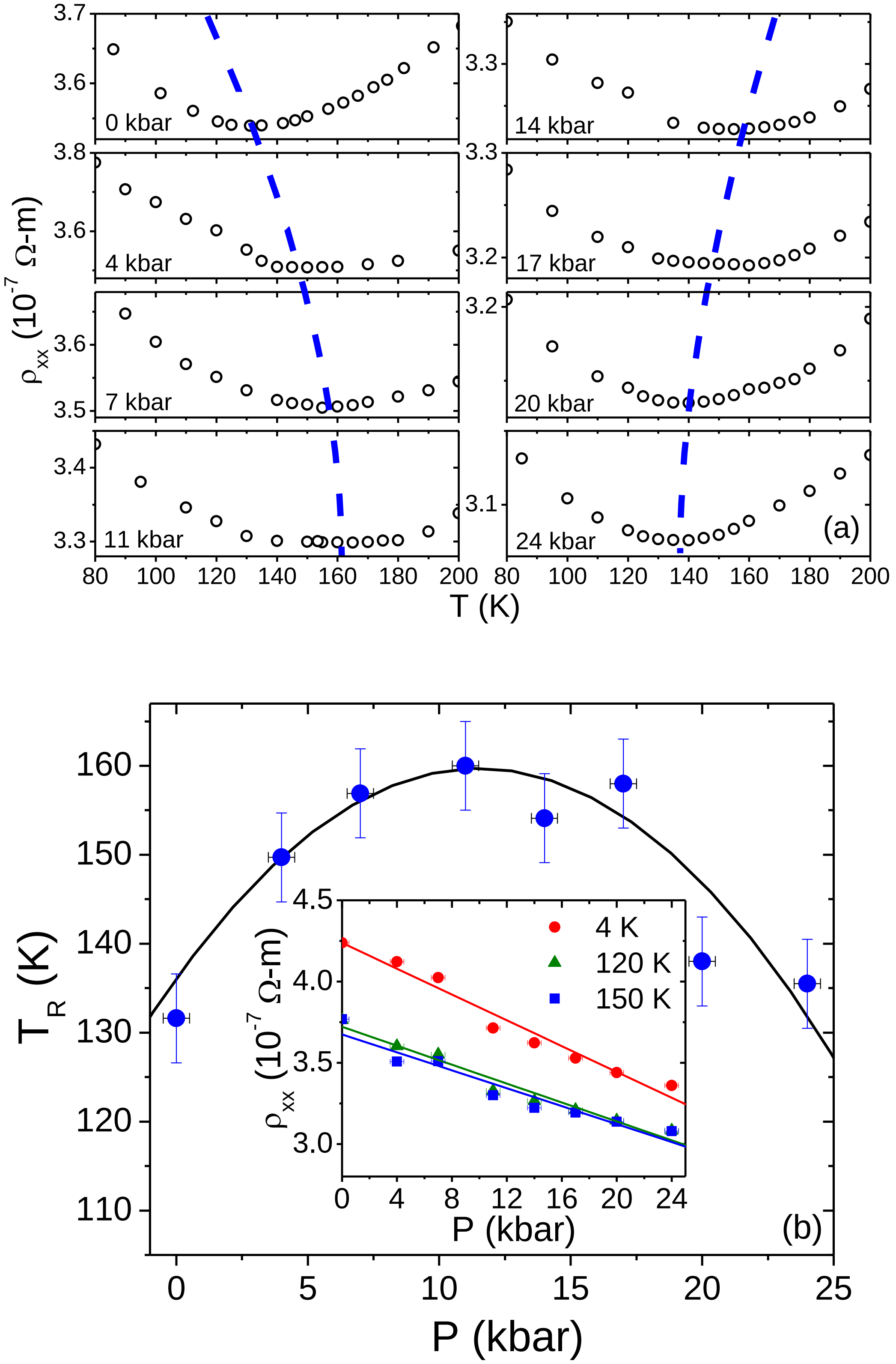

Figure 7.2 (a) $\rho_{xx}(T)$ measured at various pressures up to 24 kbar. (b) Pressure dependence of T_R. The inset shows the $\rho_{xx}(T)$ measured at 4 K, 120 K and 150 K.

The hole concentration ($p_o = \dfrac{1}{R_o e}$) and mobility ($\mu = \dfrac{1}{p_o \rho_{xx} e}$) are obtained to be $3.7\times10^{27}\, m^{-3}$ and $39.8\, cm^2V^{-1}s^{-1}$, respectively. The Mott's criterion ($p_o > p_c = \left(\dfrac{0.25}{a_H}\right)^3 = 3.9\times10^{24}\, m^{-3}$) and the products of $k_F\lambda \approx 24-27>1$ indicate that the system is in the metallic regime.

Figure 7.2 (a) shows the $\rho_{xx}(T)$ curves at various pressure (P). The shift in T_R with pressure (P) denotes a corresponding change in T_c. In view of the difficulty of identifying T_R from the broad minimum of $\rho_{xx}(T)$, we determine T_R from the temperature derivative of resistivity $\dfrac{d\rho_{xx}}{dT}$ at the temperature-axis intercept. We show in Figure 7.2 (b) that $T_R\left(\approx T_c\right)$ increases and reaches a maximum at 160 K before decreases with pressure. Within the same pressure range, this parabolic behavior of T_c differs from that of (In,Mn)Sb [6], (Sb,V)Te [12] and (Pb, Sn, Mn)Te [13], where either an increase or decrease in T_c was observed in a single sample. The inset of Figure 7.2 (b) shows that $\rho_{xx}(T)$ decreases linearly at $\dfrac{d\rho}{dP} \sim 3.2\times10^{-9}\ \Omega\text{-m/kbar}$. We note the resistivity as a function of pressure is an intrinsic property of $Ge_{1-x}Mn_xTe$ given the fact that BaF_2 substrate is highly insulating and thus it does not influence the results. In the previous Chapter, we have studied the pressure effect of magnetotransport in $Ge_{1-x}Mn_xTe$ ($x \sim 0.1$). Here, we recollect that the M-T curve shows a concave behavior which indicates a short-range ferromagnetic order. The T_c only exhibits a linear increase with pressure. The monotonic increase in

$J_{pd}\left(\approx 0.19\,\mathrm{meV/kbar}\right)$ is small, which can be attributed to the large average-spacing between Mn ions ($R_{ave} \sim 0.81\,\mathrm{nm}$) and there is no reduction in T_c with pressure up to 20 kbar.

Figure 7.3 (a) shows the Hall resistivity $\rho_{xy}(H)$ measured at 4K with various pressures. The hole concentration and mobility as functions of pressure can be obtained from $\rho_{xy}(H)$ as shown in Figure 7.3 (b). The increase in the hole concentration ($\frac{dp_o}{dP} \approx 8.5\times10^{25}\ \mathrm{m}^{-3}/\mathrm{kbar}$) and the decrease in mobility with pressure can be explained using a two valence band (VB) model [14,15]. The schematic diagram of the two valence band structure is as illustrated in Figure 6.4. At a hole concentration of $3.7\times10^{27}\ \mathrm{m}^{-3}$, the Fermi level ($E_F$) lies inside both the L and $\sum$ bands [16]. The effect of pressure shifts the $\sum$ band upwards and thus descends E_F further into the valence bands. This results in an increase of light holes and heavy holes density from L and $\sum$ band, respectively. The contribution of the heavy holes is predominant due to the large effective mass of these carriers at the $\sum$ band, which leads to a decrease in the overall mobility. This scenario has also been observed by T. Story *et al.* in (Pb,Sn,Mn)Te especially for those samples with higher hole concentrations [17]. Nonetheless, the increase in carrier concentration dominates over the reduction in mobility which leads to an overall decrease in $\rho_{xx}(T)$ with pressure.

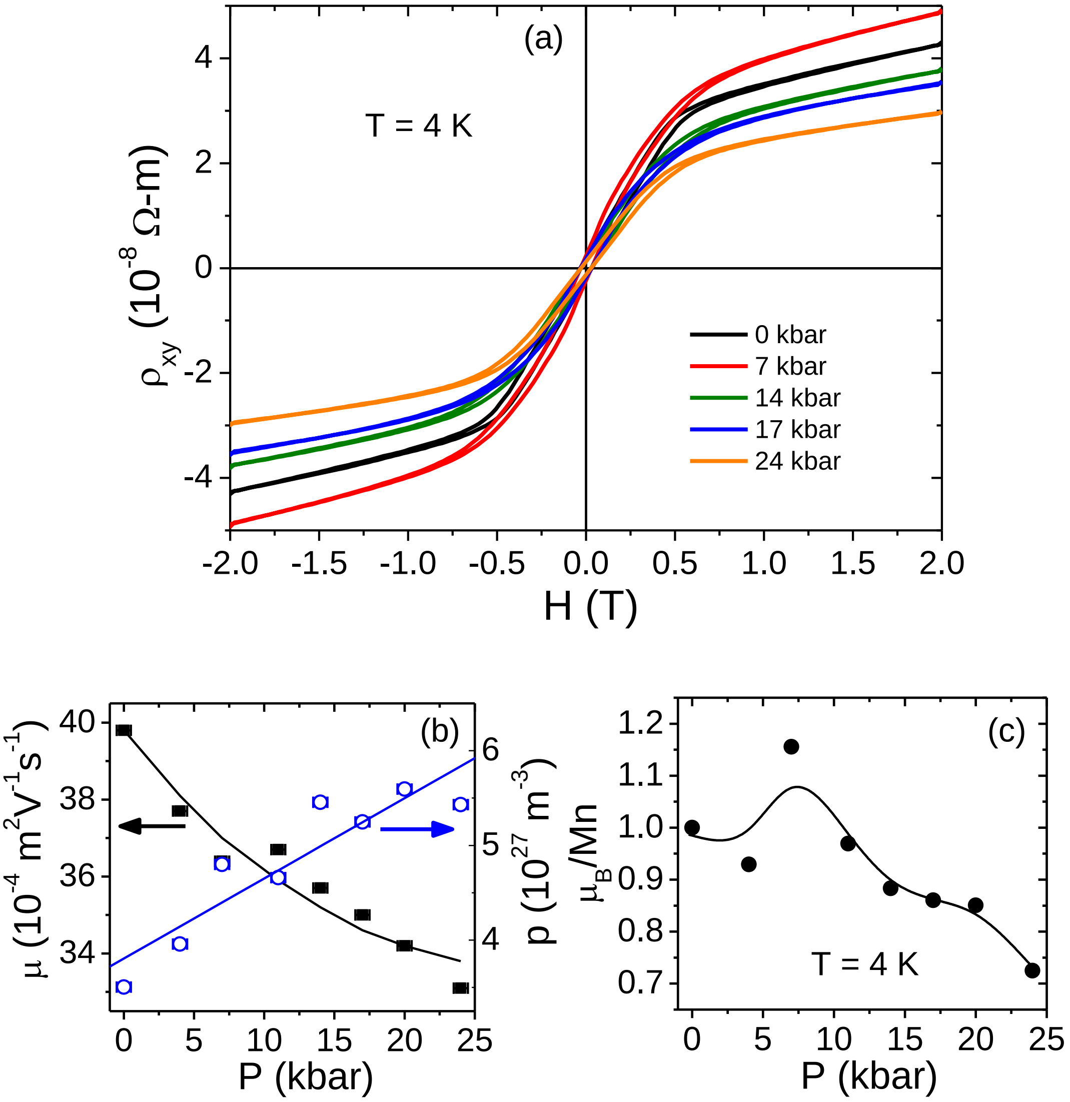

Figure 7.3 Pressure dependence of (a) $\rho_{xy}(H)$, (b) mobility and hole concentration and (c) μ_B/Mn measured at 4 K.

The magnetization deduced from $\rho_{xy}(H)$ indicates a slight increase in the effective magnetic moment contributed by the Mn ions at pressure lower than 11 kbar followed by a decrease at higher pressure as shown in Figure 7.3 (c).

7.2.2 Influence of exchange interaction on T_c of Ge$_{1-x}$Mn$_x$Te.

The *prima facie* experimental observation in the increase of T_c seems to indicate an increase in carrier concentration as observed in most carrier-mediated FMS [4]. It is known that the increase in carrier concentration can also lead to the suppression in T_c due to the frustration induced by RKKY oscillation when $\frac{p_o}{n_i} >> 1$ [18], where $n_i = \frac{4x}{a_o^3}$ is the impurity concentration, as discussed in Chapter 6. However, in our case, the p_o at the maximum P of 24 kbar is $\sim 5.4 \times 10^{27}$ m^{-3} which gives a value of $\frac{p_o}{n_i} \approx 0.9$. Thus, the frustration induced by RKKY oscillation does not fully explain the decrease in T_c beyond 11 kbar.

In order to explain the change in T_c with pressure, we take into account a two VB model where T_c can be expressed as

$$T_C = \frac{2xS(S+1)}{3k_B}\left[v_L I_L + v_\Sigma I_\Sigma\right] \tag{7.1}$$

where S = 5/2 is the Mn spin, $v_L = 4$ and $v_\Sigma = 12$ are the number of valleys in the L and $\sum$ band, respectively, I_L and I_Σ are the RKKY exchange integral contributions from magnetic ions interacting with free hole carriers from the VB and can be expressed as [17],

$$I = \left(m^*\right)\left(\frac{a_o^2}{2^9 \pi^3 \hbar^2}\right)\left(2k_F a_o\right)^4 J_{pd}^2 \sum_{ij} z_{ij} F\left(2k_F R_{ij}\right) e^{-R_{ij}/\lambda} \tag{7.2}$$

where J_{pd} is the exchange integral between holes and Mn ions, $R_{ij} = a_o\sqrt{\frac{i}{2}}$ is the distance between Mn ion site *i* and *j*, z_{ij} is the number of nearest neighbors in the R_{ij} range and $F(2k_F R_{ij}) = \left[\frac{\sin 2k_F R_{ij} - 2k_F R_{ij}\cos 2k_F R_{ij}}{(2k_F R_{ij})^4}\right]$ is the oscillatory spatial function. For a fixed x, the main factors that affect T_c in Eq. (7.2) are a_o, k_F, J_{pd} and $F(2k_F R_{ij})$. The effect of pressure directly leads to a decrease in a_o, which can be determined from the bulk modulus (*B*) of $Ge_{1-x}Mn_xTe$. We assume the *B* value is the same as that of GeTe, i.e. $B = -V\frac{dP}{dV} = 510\,kbar$, where *V* is the volume of the unit cell. The corresponding a_o value at each pressure is shown at the top axis of Figure 7.4 (a). Additionally, pressure suppresses $F(2k_F R_{ij})$ for both the light holes (p_L) and heavy holes (p_Σ). The $F(2k_F R_{ij})$ function can be observed to shift towards a smaller R_{ave} where $R_{ave} \sim 0.55\,\text{nm}$ is the average distance between Mn ions as shown in the inset of Figure 7.4 (b) (vertical dash line). We observe that the $F(2k_F R_{ij})$ function is dominated by heavy holes from the $\sum$ band since heavier carrier leads to a more critically damped and larger magnitude of $F(2k_F R_{ij})$. On the other hand, k_F value increases with pressure due to the increase in p_o. Taking all these factors into consideration, we can calculate the J_{pd} as a function of pressure, which is depicted in Figure 7.4 (a). Interestingly, J_{pd} correlates well with the trend of T_c as a function of pressure.

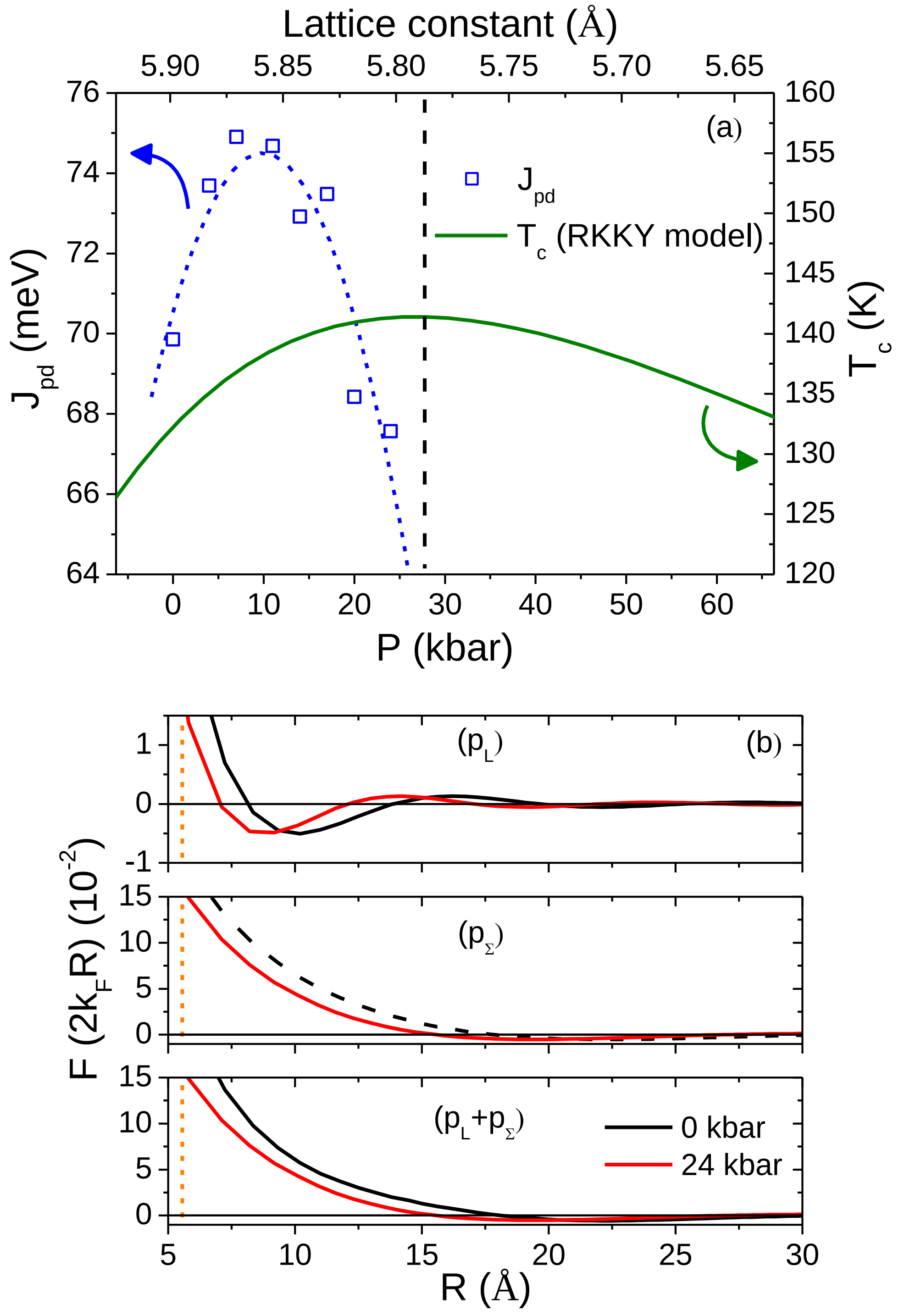

Figure 7.4 (a) The exchange integral (J_{pd}) as a function of pressure. The solid line shows the calculated pressure dependence of T_c at a fixed exchange integral using the RKKY model. (b) The dependence of the RKKY oscillatory function ($F(2k_FR)$) for light holes light holes (p_L), heavy holes (p_Σ) and the sum of p_L and p_Σ as a function of ion-ion separation (R) at 0 and 24 kbar.

For a fixed value of J_{pd} ~ 70 meV, we would only expect T_c to decrease gently at P > 28 kbar, as shown by the black dashed line in Figure 7.4 (a). While the change in T_c can be attributed to competing effects between $(k_F)^4$ and $(a_o)^6 F(2k_F R_{ij})$, they seem to be dominated by the effect of $(J_{pd})^2$.

The increase in J_{pd} can be ascribed to the dependence of *p-d* hybridization energy on the bond length [1]. A total of 1.7% reduction in the lattice constant is expected at P ~24 kbar and R_{ave} also decreases accordingly. We note that the lattice constant (a_o) of $Ge_{1-x}Mn_xTe$ decreases linearly with x [19] and a maximum T_c is usually observed at $x \sim 0.5$ for the same carrier concentration [2,3,5]. Thus, the decrease in a_o by pressure in a given sample shares the similar effect of having a higher x. As R_{ave} further decreases, antiferromagnetic superexchange interaction becomes apparent and competes with RKKY indirect-exchange coupling between Mn ions. The antiferromagnetic superexchange is that of the Anderson-type superexchange interaction between Mn cations via Te anions. Thus, the superexchange is strongly dependent on the cation-anion distance. The cation-anion distance (*d*) for a rock-salt structure is $0.5a_o$. It has been observed in IV-VI compound magnetic semiconductors that a small difference in *d* can lead to a change of superexchange interaction (J_{se}) parameter by an order of magnitude or more. It is known that J_{se} scales as $(1/d^{16})$ [20]. Thus, a decrease in the lattice constant of 1.7%

can translate to an increase in the antiferromagnetic superexchange of 27%. The result is significant enough to decrease J_{pd} by ~ 10%. Hence, we observed a decrease in J_{pd} as a_o shrinks beyond 0.587 nm.

Lastly, we conclude on the effects of pressure observed for the present sample with $x = 0.3$ and $x = 0.1$ discussed in Chapter 6. The increase in T_c with pressure for both samples is due to the increase in carrier concentration and exchange interaction between Mn ions and hole carriers. The increasing pressure causes the lattice constant to become smaller. A smaller lattice constant will enhance J_{pd} which depends on the bond length. However, a smaller lattice constant also increases the J_{se} between Mn ions via Te anions. This effect is more severe in $x = 0.3$ sample due to a higher Mn concentration. In $x = 0.1$ sample, the T_c increases monotonically with pressure while in $x = 0.3$ sample, the T_c changes parabolically as J_{se} becoming more significant at high pressure. Additionally, the $x = 0.3$ sample has a higher hole carrier concentration, and this causes the E_F to move further below the valence band as compared with the $x = 0.1$ sample. The effect of pressure elevates the $\sum$ valence band which allows more hole carriers to fall within the E_F. Thus the increment of hole carriers for $x = 0.3$ is more than that for $x = 0.1$. This also leads to a larger slope (2.5 K/kbar) for $x = 0.3$ sample.

7.3 Summary

We have measured the magnetotransport properties as a function of pressure on $Ge_{1-x}Mn_xTe$ (x = 0.3). While the carrier concentration increases linearly with pressure, the longitudinal resistivity and carrier mobility both decreases with pressure. The exchange interaction correlates well with the behavior of T_c with pressure using the RKKY and two valence band models. The factors influencing the T_c can be identified as ρ_o, a_o, $F(2k_F R_{ij})$ and J_{pd}. The increase in T_c with pressure for both samples (x = 0.1 and 0.3) is mainly due to the increase in carrier concentration and exchange interaction between Mn ions and hole carriers. However, owing to the higher Mn ions concentration in x = 0.3 sample, the effect of antiferromagnetic superexchange becomes more prominent than that of x = 0.1 as lattice constant is reduced, leading to the suppression of T_c.

Chapter 7 References

[1] T. Dietl, H. Ohno and F. Matsukura, *Hole-mediated ferromagnetism in tetrahedrally coordinated semiconductors*, Phys. Rev. B **63**, 195205 (2001).

[2] W. Q. Chen, K. L. Teo, M. B. A. Jalil *et al.*, *Compositional dependencies of ferromagnetic* $Ge_{1-x}Mn_xTe$ *grown by solid-source molecular-beam epitaxy*, J. Appl. Phys. **99**, 08D515 (2006).

[3] Y. Fukuma, H. Asada, N. Nishimura *et al.*, *Ferromagnetic properties of IV-VI diluted magnetic semiconductor* $Ge_{1-x}Mn_xTe$ *films prepared by radio frequency sputtering*, J. Appl. Phys. **93**, 4034 (2003).

[4] Y. Fukuma, H. Asada, S. Miyawaki *et al.*, *Carrier-induced ferromagnetism in* $Ge_{0.92}Mn_{0.08}Te$ *epilayers with a Curie temperature up to 190 K*, Appl. Phys. Lett. **93**, 252502 (2008).

[5] M. Hassan, G. Springholz, R. T. Lechner *et al.*, *Molecular beam epitaxy of single phase GeMnTe with high ferromagnetic transition temperature*, J. Cryst. Growth **323**, 363 (2011).

[6] M. Csontos, G. Mihály, B. Jankó *et al.*, *Pressure-induced ferromagnetism in (In,Mn)Sb dilute magnetic semiconductor*,, Nature Mater. **4**, 447 (2005).

[7] M. Csontos, G. Mihály, B. Jankó *et al.*, *Effect of hydrostatic pressure on the transport properties in magnetic semiconductors*, Phys. Stat. Sol. (c) **1**, 3571 (2004).

[8] T. Dietl, H. Ohno, F. Matsukura *et al.*, *Zener model description of ferromagnetism in Zinc-Blende magnetic semiconductors*, Science **287**, 1019 (2000).

[9] S. T. Lim, J. F. Bi, K. L. Teo *et al.*, *Effect of hydrostatic pressure in degenerate* $Ge_{1-x}Mn_xTe$, Appl. Phys. Lett. **95**, 072510 (2009).

[10] H. Ohno, *Making Nonmagnetic Semiconductors Ferromagnetic*, Science **281**, 951 (1998).

[11] G. Mihály, M. Csontos, S. Bordács *et al.*, *Anomalous Hall Effect in the (In,Mn)Sb Dilute Magnetic Semiconductor*, Phys. Rev. Lett. **100**, 107201 (2008).

[12] J. S. Dyck, T. J. Mitchell, A. J. Luciana *et al.*, *Significant suppression of ferromagnetism by hydrostatic pressure in the diluted magnetic semiconductor* $Sb_{2-x}V_xTe_3$ *with* $x<0.03$, Appl. Phys. Lett. **91**, 122506 (2007).

[13] T. Suski, J. Igalson, and T. Story, *Ferromagnetism of PbSnMnTe under high pressure*, J. Magn. Magn. Mater. **66**, 325 (1987).

[14] F. Herman, R. L. Kortum, I. B. Ortenburger *et al.*, *Relativistic band structure of*

GeTe, SnTe, PbTe, PbSe, and PbS, J. Phys. Colloq. **29**, C4-62 (1968).

[15] J. E. Lewis, *Optical properties and energy gap of GeTe from reflectance studies*, Phys. Stat. Sol. (b) **59**, 367 (1973).

[16] N. V. Kolomoets, E. Ya. Lev, and L. M. Sysoeva, Sov. Phys. Sol. Stat., **6,** 551 (1964).

[17] T. Story, G. Karczewski, L. Świerkowski *et al.*, *Magnetism and band structure of the semimagnetic semiconductor Pb-Sn-Mn-T*e, Phys. Rev. B 42, 10477 (1990).

[18] S. Das Sarma, E. H. Hwang, and D. J. Priour, Jr., *Enhancing* T_c *in ferromagnetic semiconductors*, Phys. Rev. B **70**, 161203(R) (2004).

[19] J. F. Bi and K. L. Teo, *Nanoscale* $Ge_{1-x}Mn_xTe$ *ferromagnetic semiconductors,* in The Oxford Handbook of Nanoscience and Technology (Materials, Structures, Properties and Characterization Techniques, ed. By A. V. Narlikar and Y. Y. Fu, vol. II page 632 (2010).

[20] M. Górska and J. R. Anderson, *Magnetic susceptibility and exchange in IV-VI compound diluted magnetic semiconductors,* Phys. Rev. B **38**, 9120 (1988).

CHAPTER 8

8. WEAK LOCALIZATION AND ANTILOCALIZATION OF HOLE CARRIERS IN DEGENERATE *p*-$Ge_{1-x}Mn_xTe$

In the previous Chapter, we have investigated the effects of hydrostatic pressure on $Ge_{1-x}Mn_xTe$ and identified some of the factors that influence its T_c. This Chapter will focus on the study of magnetotransport properties of $Ge_{0.7}Mn_{0.3}Te$ (Sample D) at various applied pressures and temperatures. In particular, we are interested to investigate its magnetoresistance behavior. The magnetoresistance (MR) is characterized by both positive and negative contributions, which can be described by the antilocalization and weak localization models, respectively. The temperature and pressure dependence of spin-orbit, elastic and inelastic scattering times as well as coherence length of $Ge_{0.7}Mn_{0.3}Te$ will be discussed. The spin-orbit scattering time is found to be independent of pressure and temperature and it dominates over the inelastic scattering time leading to the observed positive MR. The phase coherent length is correlated to the inelastic scattering which is predominately due to electron-electron scattering.

8.1 Introduction and Motivation

Magnetotransport studies of FMS have served as direct and convenient means of probing the electronic and magnetic properties of the material [1,2,3,4,5]. Magnetization is often manifested in the anomalous Hall term of the Hall resistivity which may arise from scattering processes involving spin-orbit coupling such as side-jump and skew scattering [6]. Additionally, the strong spin-dependent coupling between the carriers and the localized magnetic states often leads to the giant spin splitting of electronic states and spin-disorder scattering which affects the electronic transport, and resulting in positive and negative MR [7]. In widely studied FMS, such as II-Mn-VI ($Cd_{1-x}Mn_xTe$ and $Zn_{1-x}Mn_xO$) [1,2], the weak-field positive MR has been attributed to giant spin splitting of the electron states that affects quantum corrections to the conductivity due to disorder modified electron-electron interactions while the negative MR at higher field is associated with the suppression of magnetic fluctuations leading to formation of bound magnetic polarons. In the case of III-Mn-V FMS ($Ga_{1-x}Mn_xAs$) [3], weak-field positive MR is not observed as the hole states are already spin polarized in the absence of magnetic field and its negative MR can be quantitatively described by the weak-localization orbital effect. In $In_{1-x}Mn_xAs$, the negative MR is due to spin-dependent scattering of carriers in an impurity band by localized magnetic moments [4]. Recent magnetotransport studies on $In_{1-x}Mn_xSb$ also show that the positive MR can be described by a two band model in which the bands consist of spin-split hybridized *p-d* subbands [5].

Although carrier mediated ferromagnetism [8,9] and anomalous Hall effect (AHE) [10,11] have been observed in IV-Mn-VI FMS, such as $Ge_{1-x}Mn_xTe$, magnetotransport studies on this material have been limited. In contrast to III-Mn-V FMS, where Mn is both the source of localized magnetic moment moments and free carriers, Mn^{2+} incorporated in $Ge_{1-x}Mn_xTe$ is isoelectronic to Ge and free carriers are only contributed by Ge vacancy and defects. Additionally, ferromagnetism in $Ge_{1-x}Mn_xTe$ is attributed to RKKY interaction owing to the deep positioning of the 3*d* states of Mn in the valence band [12].

We present the results of the magnetoresistance measurements on *p*-type $Ge_{0.7}Mn_{0.3}Te$ thin films (Sample D). The sample is subjected to hydrostatic pressure to induce changes in the T_c as well as scattering properties, which in turn affects the MR results. Fundamentally, MR can be ascribed to the consequence of the scattering of carriers in response to a field perturbation. This scattering is due to the relative contributions from elastic (τ_e^{-1}), inelastic (τ_{ie}^{-1}), spin-orbit (τ_{so}^{-1}) and magnetic scattering (τ_s^{-1}) processes (i.e. $\tau^{-1} = \tau_e^{-1} + \tau_{ie}^{-1} + \tau_{so}^{-1} + \tau_s^{-1}$). We analyze the positive MR using the model proposed by Fukuyama and Hoshino [13], which we are able to obtain the temperature and pressure dependence of inelastic and spin-orbit scattering times. On the other hand, the negative MR is analyzed using the model developed by Kawabata [14] and Althuler *et al.* [15] where the temperature and pressure dependence of the phase coherent length can be acquired. We show that both analyses are consistent and lead to the conclusion that inelastic scattering at low temperature is predominately due to electron-electron scattering.

8.2 Results and Discussion

8.2.1 Temperature dependence of Hall resistivity.

In FMS, the Hall resistivity (ρ_{xy}) can be described as the sum of normal Hall contribution (ρ_o) due to Lorentz force and anomalous Hall term (ρ_{AH}) that is proportional to the magnetization (*M*),

$$\rho_{xy} = \rho_o + \rho_{AH} = R_o H + R_s M$$

$$M \propto \frac{\rho_{xy} - R_o H}{{\rho_{xx}}^{n}} \tag{8.1}$$

where *H* is the magnetic field, ρ_{xx} is the longitudinal resistivity, *n* = 1 (for skew-scattering) and *n* = 2 (for side-jump), R_o and R_s are the ordinary and anomalous Hall coefficients, respectively. Figure 8.1 (a) shows the temperature dependence of Hall resistivity ($\rho_{xy}(T)$). The ρ_{AH} can be observed to dominate over ρ_o at low magnetic field (*H*) for T < 140 K after which $\rho_{xy}(T)$ becomes linearly dependent of *B*. This result is in agreement with the magnetization measurement which shows that the T_c ~132 K. As temperature approaches T_c, the effect of ρ_{AH}

diminishes and $\rho_{xy} \cong R_o H$. The linear dependence of $\left(\rho_{xy} - R_o H\right)/\rho_{xx}$ with the magnetization (measured from SQUID) is verified in Figure 8.1 (c).

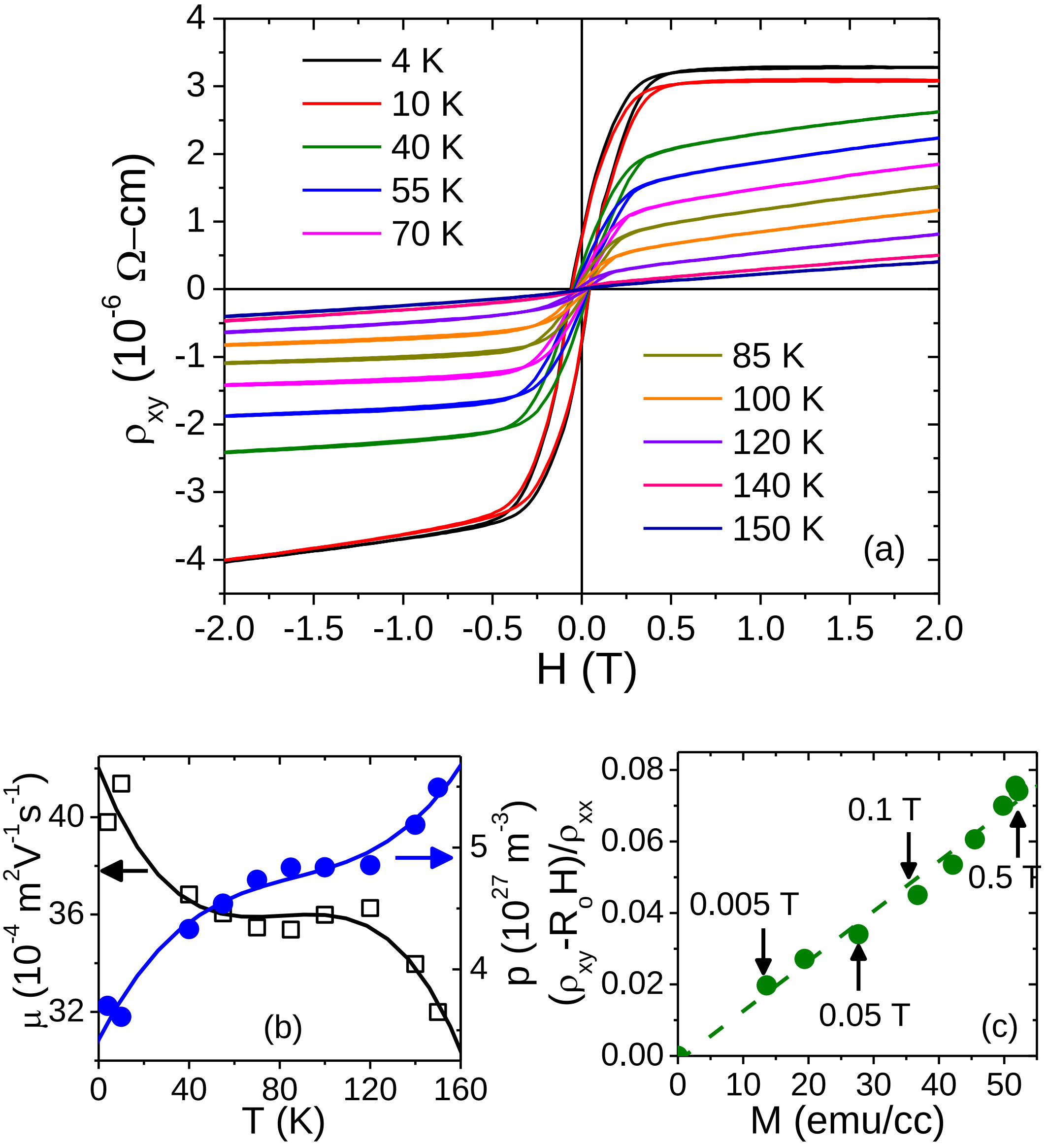

Figure 8.1 Temperature dependence of (a) Hall resistivity ($\rho_{xy}(T)$), (b) mobility (open symbols) and hole concentration (close symbols). (c) The linear dependence of magnetization with $(\rho_{xy}\text{-}R_oH)/\rho_{xx}$.

The hole concentration, $p_o = 1/(R_o e)$ and mobility, $\mu = 1/(p_o \rho_{xx} e)$ were calculated from R_o, which can be determined from the slope of ρ_{xy}, ($d\rho_{xy}/dH|_{H>1T}$) at high H region where the ordinary Hall effect dominates. However, we note that for $T > T_c$, the values obtained are approximates due to the paramagnetic effect. The behavior of hole concentration ($p_o(T)$) and mobility ($\mu(T)$) as a function of temperature is shown in Figure 8.1 (b). In order to ascertain the conduction regime of the sample, we analyzed the product $k_F \lambda$, where $k_F = (3\pi^2 p/v)^{1/3}$ is the Fermi wave number (v is the number of valleys) and $\lambda = \hbar k_F \mu/e$ is the mean free path. The values obtained for $k_F \lambda$ at each temperature are about 25, indicating that the system should behave like metal.

8.2.2 Temperature and pressure dependence of antilocalization effect in Ge$_{1-x}$Mn$_x$Te.

In the metallic regime, especially for disordered electronic systems, single-particle and many-body quantum interference effects are associated with localization [16]. It is also known that weak localization occurs in these systems at very low temperatures and it manifest itself as a quantum correction to the conductivity in metal or semiconductor. Additionally, in the weak localized regime, where $k_F \lambda > 1$, positive MR (antilocalization effect) is originated from giant splitting of electron state and spin-orbit scattering effects, which lead to destructive interference and reduces the probability of electrons forming closed paths (i.e. weak localization effect) [17]. However, since magnetic field suppresses localization effect, negative MR is often observed at high magnetic field.

The MR measurements on $Ge_{0.7}Mn_{0.3}Te$ reveal the presence both positive and negative components. A cross-over between antilocalization and localization at T = 4 K is observed at H = 0.2 T, where $\Delta\rho = 0$. We analyzed the positive MR using the model proposed by Fukuyama and Hoshino [13]. The model considers the effects of Zeeman splitting and spin-orbit interaction on MR in three dimensional disordered systems in the weakly localized regime as

$$\frac{\Delta\rho}{\rho} \approx -\frac{\Delta\sigma}{\sigma} = -\rho \mathrm{A} \left[\begin{array}{l} \sqrt{h}\, f\left(\frac{1+\mathrm{t}}{\mathrm{h}}\right) + \frac{1}{2}\sqrt{\frac{h}{1-\gamma}}\left\{ f\left(\frac{\mathrm{t}_+}{\mathrm{h}}\right) - f\left(\frac{\mathrm{t}_-}{\mathrm{h}}\right)\right\} \\ -\frac{1}{\sqrt{1-\gamma}}\left(\sqrt{\mathrm{t}_-}-\sqrt{\mathrm{t}_+}\right)+\sqrt{\mathrm{t}}-\sqrt{\mathrm{t}+1} \end{array}\right] \tag{8.2}$$

where $\mathrm{A} = \frac{\sqrt{3}e^2}{2\pi^2\lambda\hbar}\sqrt{\frac{\tau_e}{\tau_{so}}}$, $h = \left(\frac{\lambda}{\lambda_B}\right)^2\left(\frac{\tau_{so}}{3\tau_e}\right)$, $\mathrm{t} = \frac{\tau_{so}}{4\tau_{ie}}$, $\gamma = \left(\frac{g\mu_B H\tau_{so}}{2\hbar}\right)$, $t_\pm = t + \frac{1}{2}\left(1 \pm \sqrt{1-\gamma}\right)$, $\lambda_B = \sqrt{\frac{\hbar}{eH}}$ is the magnetic length, τ_e , τ_{ie} and τ_{so} are the elastic, inelastic and spin-orbit (s-o) scattering times, respectively. The g is the Landé factor and $f(x) = \sum_{N=0}^{\infty}\left\{2\left(\sqrt{N+1+x}-\sqrt{N+x}\right)-\left(\sqrt{N+\frac{1}{2}+x}\right)^{-1}\right\}$ is Kawabata's function [14]. Considering a metallic system and using the Drude relation for the conductivity, we assume the elastic scattering time $\tau_e = \frac{m^*\lambda}{\hbar k_F}$ and m^* is the hole effective mass. Since the hole concentration is relatively high ~10^{27} m^{-3}, we would expect the Fermi level to intercept both the L and $\sum$ valence bands [18], Thus, by considering a two valence band (VB) model, Eq. (8.2) can be re-expressed:

$$\frac{\Delta\rho}{\rho} = v_L \frac{\Delta\rho_L}{\rho_L} + v_\Sigma \frac{\Delta\rho_\Sigma}{\rho_\Sigma} \tag{8.3}$$

where $v_L = 4$ and $v_\Sigma = 12$ are the number of equivalent valleys in the L and $\sum$ valence bands, respectively.

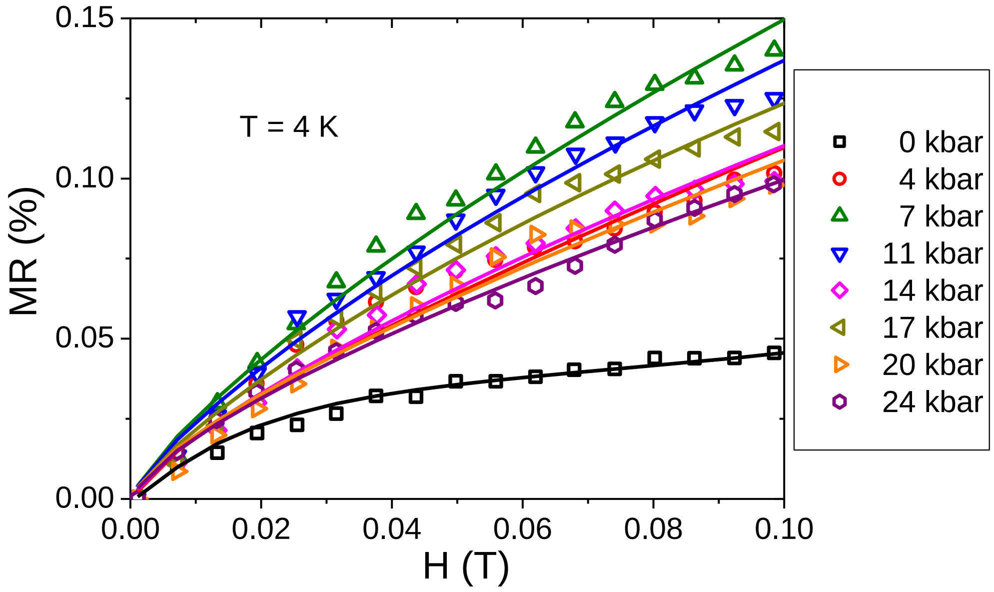

Figure 8.2 Pressure dependence of Weak-field MR measured at 4 K. The solid lines are curve fitting using Eq. (8.3).

We shall first discuss the effects of pressure (P) on the positive MR at T = 4 K. The curve fittings at each pressure are depicted as solid lines in Figure 8.2, with τ_{ie} and τ_{so} as fitting parameters. The pressure (P) dependence of $\tau_{ie}(P)$, $\tau_{so}(P)$ and $\tau_e(P)$ are shown in Figure 8.3 (a). We have also plotted the inelastic scattering time $\tau_{ie}*(P)$ obtained from the weak localization model (negative MR), which shall be discussed later in section 8.3.3. We denote it as τ_{ie} * to differentiate it from τ_{ie} obtained from the antilocalization effect (Eq. (8.2)). The magnetic scattering time is estimated to be $\tau_s \sim 10^{-9}$ s using the equation proposed by Amaral [19], with an exchange integral of 70 meV obtained for our sample at T = 4 K in Chapter 7.

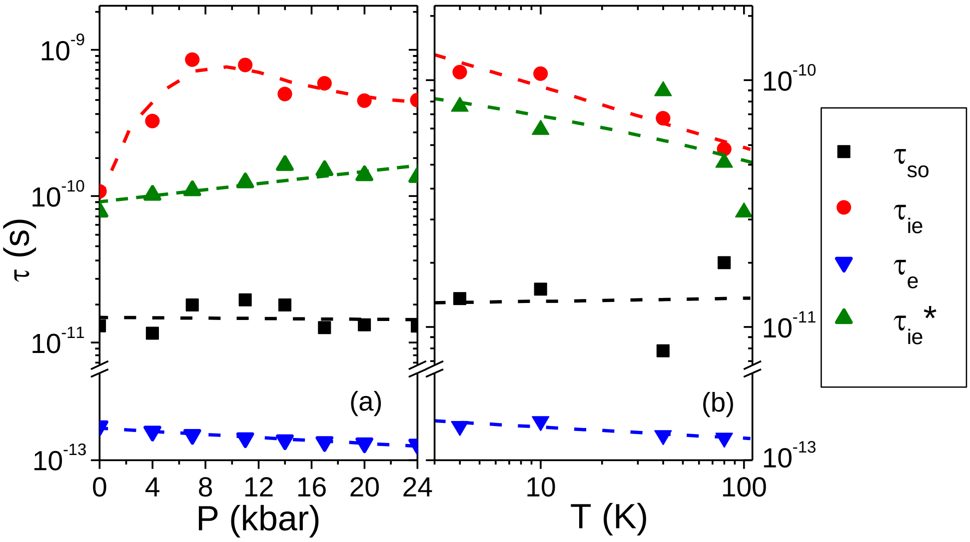

Figure 8.3 (a) Pressure and (b) temperature dependence of inelastic (τ_{ie} and τ_{ie}^*), spin orbit (τ_{so}) and elastic (τ_e) scatterings.

Since τ_s is an order of magnitude smaller than τ_{ie}, we expect the magnetic scattering to play a minor role in the scattering process. We observe that τ_{so} to be independent of pressure and lower in magnitude than that of τ_{ie} as well as τ_{ie}* for all applied pressure. This indicates that the s-o scattering is dominant at 4 K. On the other hand, an increase in τ_{ie} by an order of magnitude is observed as pressure is raised from 0 to 10 kbar and subsequent increase in pressure causes τ_{ie} to gradually decrease. This feature corresponds well with the observed enhancement of positive MR for $P < 11$ kbar in Figure 8.2 as s-o scattering becomes more dominant over inelastic scattering. The initial increase in τ_{ie} could be attributed to an effective screening of Coulomb interactions as more carriers are introduced with increasing pressure. This postulation shall be further discussed later.

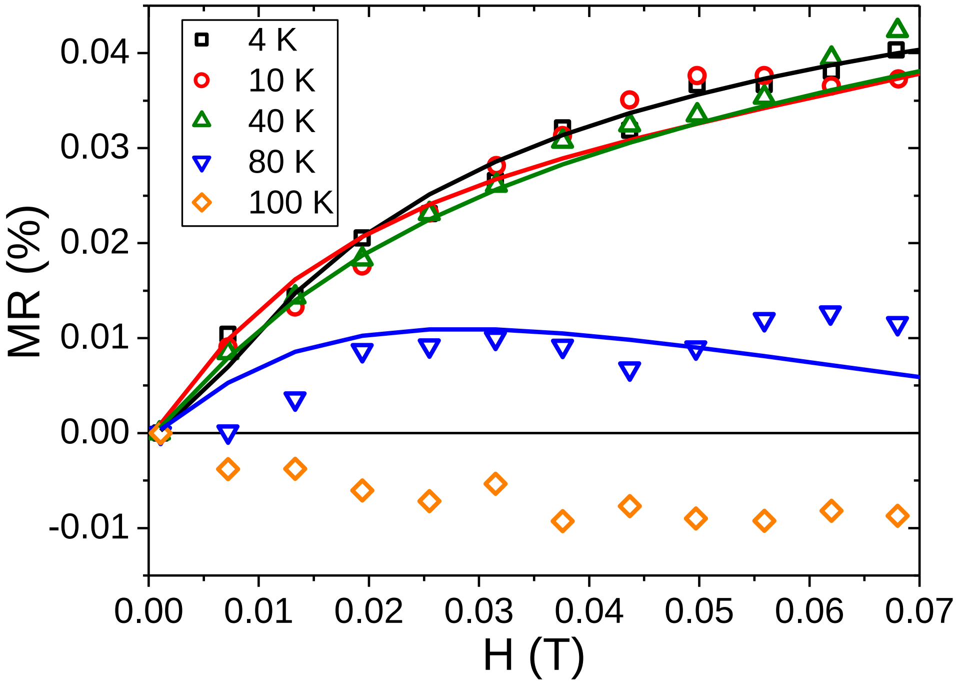

Figure 8.4 Weak-field MR measured at various temperatures. The solid lines are curve fitting using Eq. (8.3).

Figure 8.4 shows the temperature dependence of MR at low field. A transition from positive to negative MR can be observed at temperatures between 80 and 100 K. We note that this transition does not coincide with the ferromagnetic-paramagnetic transition and thermal effect could have assisted the suppression of localization at low field. The solid lines in Figure 8.4 show the curve fitting using Eq. (8.3). The temperature dependence of $\tau_{ie}(T)$ and $\tau_{so}(T)$ obtained from the fitting as well as $\tau_e(T)$ and $\tau_{ie}*(T)$ are shown in Figure 8.3 (b). The τ_{so} dominates over τ_{ie} (or $\tau_{ie}*$) at temperatures below 100 K. Both τ_{so} and τ_e are relatively indifferent to temperature with $\tau(T) \propto T^{-n}$ (n < 0.05) as compared to $\tau_{ie}(T)$ or $\tau_{ie}*(T)$ (n = 0.24). We note that in PbEuTe, antilocalization is also observed at weak-field and $\tau_{so}(T)$ < $\tau_{ie}(T)$ at T > 5 K leading to positive MR enhancement. Additionally, the $\tau_{ie}(T)$ is found to scale with $T^{-2.2}$ which was attributed to electron-phonon scattering mechanism [20].

8.2.3 Temperature and pressure dependence of weak localization effect in $Ge_{1-x}Mn_xTe$.

In the presence of a strong magnetic field, the localization of carriers are suppressed which results in negative MR. For $\tau_H > \tau_{so}$, the coherent interference is destructive. Here $\tau_H = \hbar/(4eDH)$ and $D = \left(v_F^2 \tau_e / d\right)$ is the diffusion constant [21]. However, for $\tau_H < \tau_{so}$ the phase coherence of two partial wave is destroyed, leading to $\Delta\rho < 0$. The cross-over from positive to negative MR occurs at $H \sim 0.2\,\mathrm{T}$, where we have obtained $\tau_H \approx \tau_{so} \approx 2\times10^{-11}\mathrm{s}$. In the case of negative MR, we analyzed it using the model developed by Kawabata [14] and Altshuler *et. al.* [15] for $k_F \lambda >> 1$.

For weak localization,

$$\frac{\Delta\rho}{\rho} \approx -\frac{\Delta\sigma}{\sigma} = -(\rho)\left(\frac{e^2}{2\pi^2\hbar}\right)\left(\frac{f_o}{\lambda_B}\right) f\left(\frac{\hbar}{4eH}\left(\frac{1}{L_\Phi{}^2}\right)\right) \tag{8.4}$$

where f_o is a fitting parameter which relates to the valley occupations and inter-valley scattering rates and L_Φ is the phase coherence length. The additional prefector *a* of the positive MR due to Lorenz force, $\Delta\rho = aH^2$, gives a better curve fitting. However, typical values of *a* are small (10^{-5} ΩmT^{-2}). The curve fittings of negative MR at each pressure are represented as solid lines in Figure 8.5.

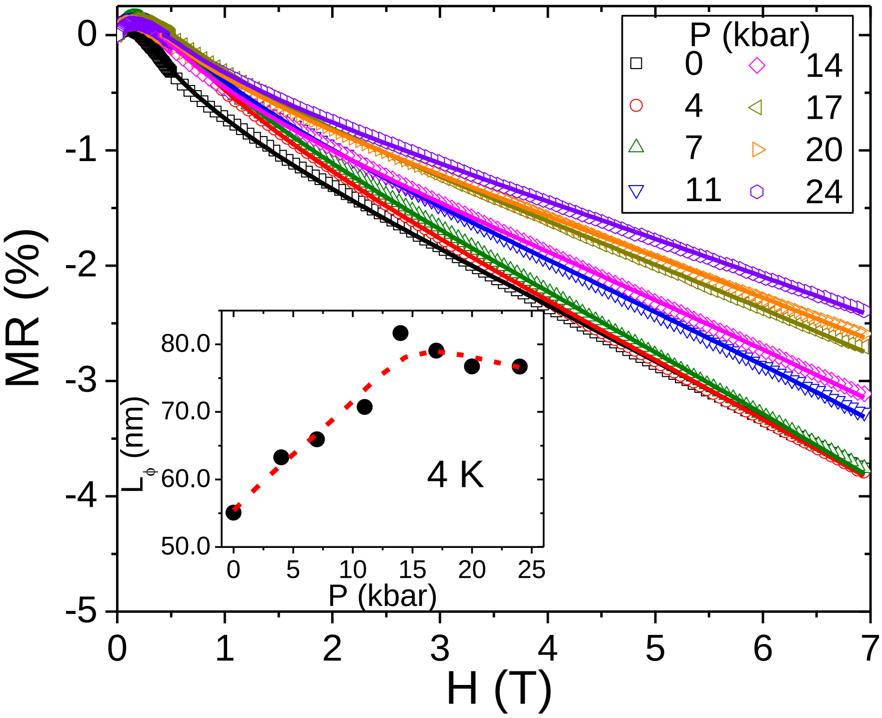

Figure 8.5 Pressure dependence of high field MR measured at 4 K. The solid lines are curve fitting using Eq. (8.4). The inset shows the variation of phase coherent length with pressure.

The inset shows the obtained $L_\Phi(P)$ increases linearly with pressure up to ~14 kbar before it begins to saturate. The initial rise of L_Φ is due to the increase in $k_F\lambda$ with pressure, which suggests a reduction in disordering in the system. The saturation of $L_\Phi(P)$ coincides with the pressure where the exchange integral is near maximum as shown in Figure 7.4. Thus, the effect of magnetic scattering could be one of the phase breaking mechanisms which opposes any further increase in $L_\Phi(P)$. Additionally, we have observed an increase in inelastic scattering (τ_{ie} or τ_{ie}^*) as pressure increases. As such, the saturation of $L_\Phi(P)$ could be due to phase breaking mechanism from the combined effects of magnetic scattering and enhanced e-e scattering at higher pressure. We note that L_Φ value is notably smaller than that obtained for $Ge_{1-x}Mn_xTe$ ($x = 0.1$) in Chapter 6. This is possibly also due to a higher carrier concentration in the present case, which increases the e-e scattering that break the dephasing time.

The inelastic scattering leads to random fluctuations which limit quantum interference necessary for localization [22]. Given that $\tau_{ie} >> \tau_e$, the electron can diffuse a distance:

$$L_\Phi = \sqrt{D\tau_{ie}^*} \tag{8.5}$$

between dephasing inelastic collision where $d = 3$ for 3-D case. The contributions of holes from both the L and Σ valence bands should be taken into account when determining the value of *D*. We would expect the heavier hole to be a dominating factor. From Eq. (8.5), we can obtain the inelastic scattering times from L_ϕ as

$$\tau_{ie}^{*} = \frac{L_\Phi^2 d}{v_F^2 \tau_e} \tag{8.6}$$

The calculated $\tau_{ie}^{*}(P)$ as a function of pressure, using Eq. (8.6), is shown in Figure 8.3 (a). We note that τ_{ie}^{*} coincides with τ_{ie} only at ambient pressure but deviates as pressure increases. In principle, we should expect only one single inelastic scattering time parameter, i.e. τ_{ie}^{*} or τ_{ie}. However, we note that τ_{ie}^{*} and τ_{ie} are obtained from the curve-fitting of MR based on two different models at different *H* field regime. On the other hand, we have seen that the temperature dependence of $\tau_{ie}^{*}(T)$ and $\tau_{ie}(T)$ correlate well based on the two models (Figure 8.3 (b)), within the experimental error bar.

The inelastic scattering can be attributed either to electron-electron (τ_{e-e}) or electron-phonon (τ_{e-p}) scattering mechanisms. Here, the electron-electron (e-e) scattering actually refers to hole-hole interactions in our *p*-type $Ge_{0.7}Mn_{0.3}Te$. We keep the notation τ_{e-e} to mean the hole-hole scattering. We note that the temperature dependence of inelastic scattering, as shown in Figure 8.3 (b), does not favor the electron-phonon scattering mechanism as we would expect a T^{-2} dependence [21]. Thus, we would expect e-e scattering to be the dominate mechanism in inelastic scattering. This is not surprising due to the high carrier concentration present in $Ge_{0.7}Mn_{0.3}Te$.

In the case of pressure effect, the deviation of τ_{ie}^{*} and τ_{ie} (except at ambient pressure) values can be explained by the effective Coulomb screening between carriers. The Coulomb potential due to screening effect can be expressed as [23]

$$V_s(\vec{r}) = \frac{q^2}{4\pi\kappa_o\varepsilon_o r}\exp(-\vec{q}_s \bullet \vec{r}) \tag{8.7}$$

where κ_o is the dielectric constant, ε_o is the permittivity of free space, r is the distance between holes and $q_s = \sqrt{3q^2 p/(2\kappa_o\varepsilon_o E_F)}$ (p is the carrier density and E_F is the Fermi energy) is the inverse of the screening length for degenerate semiconductor. The effect of pressure reduces the lattice constant a, which affects r in a similar way, and in our case, we see a reduction of a by 1.7 % for P = 24 kbar. We have also observed a corresponding increase in the p and E_F of 52 % and 32 %, respectively, in Chapter 7. This result in an overall increase of the damping term in Eq. (8.7) which is a consequence of the screening effect and hence a relatively lower Coulomb potential is felt between carriers. This could explain the initial increase in τ_{ie} as pressure increases. On the other hand, this screening effect is weakened at high field owing to the increase in E_F due to Zeeman splitting. The effect is more significant in τ_{ie}^{*} obtained from the weak localization model (at high fields) as compared with τ_{ie} from the antilocalization model (at a much lower field). This may account for the slight deviation between τ_{ie}^* and τ_{ie}.

Figure 8.6 shows the temperature dependent of MR. The solid lines depict the fitting of negative MR using Eq. (8.4) for T = 4, 10, 40, 80 K. The fitted parameter $L_\Phi(T)$ as a function of temperature is shown in the inset of Figure 8.6. The value of L_Φ at T = 100 K was obtained from the fitting of negative MR at low field. We note that L_Φ does not change much for $T < 80$ K.

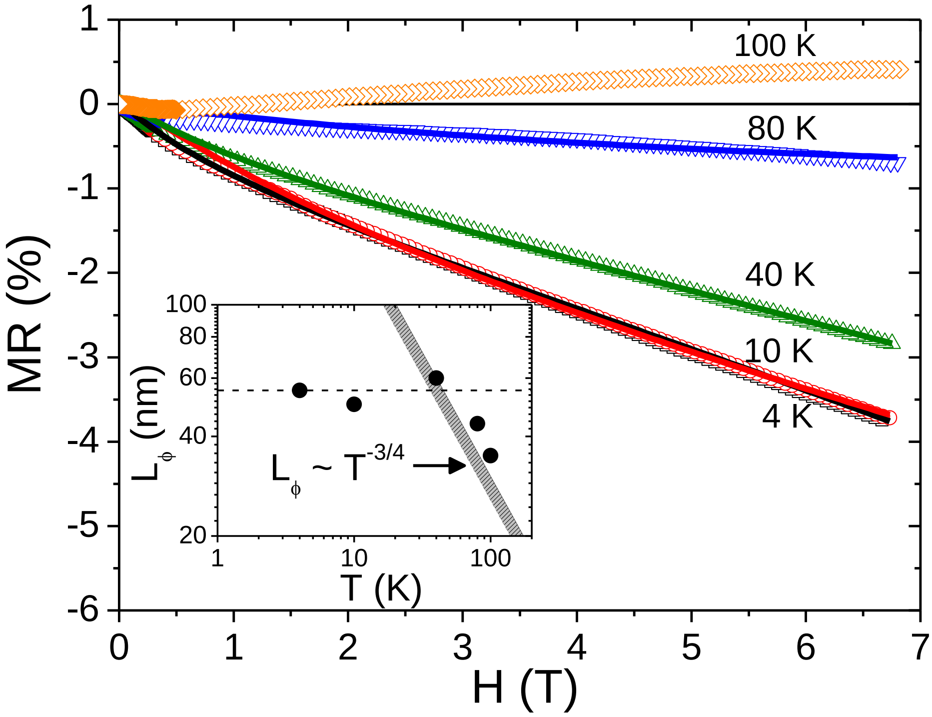

Figure 8.6 High field MR measured at various temperatures. The solid lines are curve fitting using Eq. (8.4). The inset shows the temperature dependence of the phase coherent length.

This saturation could be due to the presence of magnetic impurities or a change in the effective dimensionality of the system [14]. Altshuler *et al.* [24] predicts a

$L_\Phi(T) \propto T^{-3/4}$ behavior for the phase-breaking mechanism due to e-e interactions in the 3-D case. The grey solid bar in Figure 8.6 is a theoretical prediction of $L_\Phi(T) = \alpha T^{-3/4}$, where the constant α is related to the effective dimensionality of the system and its value varies from 8×10^{-7} to 1×10^{-6} m/K. We observed that the values of $L_\Phi(T)$ obtained from the negative MR fitting is in agreement with the theoretical prediction. This supports the notion that inelastic scattering is dominated by e-e scattering mechanism.

8.3 Summary

We have performed magnetotransport studies on *p*-type $Ge_{0.7}Mn_{0.3}Te$ at various applied pressures and temperatures. The results from Hall resistivity measurements show that the system is in the metallic regime within the temperature range studied. Both antilocalization and weak localization are evident from the magnetoresistance results. The spin-orbit scattering time is the dominant mechanism and is independent of pressure and temperature. The phase coherent length is associated with the e-e scattering and found to increase with pressure but saturates at high pressure due to the increase in effective scattering rate.

Chapter 8 References

[1] J. Jaroszyński, T. Andrearczyk, G. Karczewski *et al.*, *Intermediate phase at the metal-insulator boundary in a magnetically doped two-dimensional electron system*, Phys. Rev. B **76**, 045322 (2007).

[2] T. Andrearczyk, J. Jaroszyński, G. Grabecki *et al.*, *Spin-related magnetoresistance of n-type ZnO:Al and $Zn_{1-x}Mn_xO$:Al thin films*, Phys. Rev. B **72**, 121309 (2005).

[3] F. Matsukura, M. Sawicki, T. Dietl *et al.*, *Magnetotransport properties of metallic (Ga,Mn)As films with compressive and tensile strain*, Physica E **21**, 1032, (2004).

[4] S. J. May, A. J. Blattner, and B. W. Wessels, *Negative magnetoresistance in (In,Mn)As semiconductors*, Phys. Rev. B **70**, 073303 (2004).

[5] J. A. Peters, N. D. Parashar, N. Rangaraju, and B. W. Wessels, *Magnetotransport properties of InMnSb magnetic semiconductor thin films*, Phys. Rev. B **82**, 205207 (2010).

[6] A. Crépieux, and P. Bruno, *Theory of the anomalous Hall effect from the Kubo formula and the Dirac equation*, Phys. Rev. B **64**, 014416 (2001).

[7] Modern Aspects of Spin Physics, Lecture Notes in Physics Vol. 712 ed. by W. Pötz, J. Fabian, and U. Hohenester (Springer, Berlin, 2007).

[8] Y. Fukuma, H. Asada, M. Arifuku *et al.*, *Carrier-enhanced ferromagnetism in $Ge_{1-x}Mn_xTe$*, Appl. Phys. Lett. **80**, 1013 (2002).

[9] Y. Fukuma, M. Arifuku, H. Asada *et al.* , *Correlation between magnetic properties and carrier concentration in $Ge_{1-x}Mn_xTe$*, J. Appl. Phys. **91**, 7502 (2002).

[10] Y. Fukuma, K. Goto, S. Senba *et al.*, *IV-VI diluted magnetic semiconductor $Ge_{1-x}Mn_xTe$ epilayer grown by molecular beam epitaxy*, J. Appl. Phys. **103**, 053904 (2008).

[11] S. T. Lim, J. F. Bi, K. L. Teo *et al.*, *Magnetism and Magnetotransport studies in $Ge_{1-x}Mn_xTe$*, J. Appl. Phys. **109**, 07C314 (2011).

[12] Z. Xie, W. D Cheng, D. S. Wu *et al.*, *Ab initio study of ferromagnetic semiconductor $Ge_{1-x}Mn_xTe$,* J. Phys.: Condens. Matter, **18,** 7171 (2006).

[13] H. Fukuyama, and K. Hoshino, *Effect of Spin-Orbit Interaction on Magnetoresistance in the Weakly Localized Regime of Three-Dimensional Disordered Systems*, J. Phys. Soc. Jpn. **50**, 2131 (1981).

[14] A. Kawabata, *Theory of Negative Magnetoresistance I. Application to Heavily Doped Semiconductors*, J. Phys. Soc. Jpn **49**, 628 (1980).

[15] B. L. Altshuler, and A. G. Aronov, *in Electron–Electron Interactions in Disordered Systems*, ed. A. L. Efros, and M. Pollak, **1** (North-Holland, Amsterdam, 1985).

[16] T. Dietl, *Interplay between Carrier Localization and Magnetism in Diluted Magnetic and Ferromagnetic Semiconductors*, J. Phys. Soc. Jpn. **77**, 031005 (2008).

[17] P. A. Lee, and T. V. Ramakrishnan, *Disordered electronic systems*, Rev. Mod. Phys. **57**, 287 (1985).

[18] N. V. Kolomoets, E. Ya. Lev, and L. M. Sysoeva, Sov. Phys. Sol. Stat., **6,** 551 (1964).

[19] V. S. Amaral, *On the contribution of magnetic scattering to weak localization magnetoresistance*, J. Phys.:Condens. Matter **2**, 8201 (1990).

[20] Marcelos L. Peres, V. A. Chitta, Nei F. Oliveira *et al.*, *Antilocalization of hole carriers in* $Pb_{1-x}Eu_xTe$ *alloys in the metallic regime*, Phys. Rev. B **79**, 085309 (2009).

[21] G. Bergmann, *Weak localization in thin films a time-of-flight experiment with conduction electrons*, Phys. Rep. **107**, 1 (1984).

[22] D. J. Thouless, *Maximum Metallic Resistance in Thin Wires*, Phys. Rev. Lett. **39**, 1167 (1977).

[23] C. Hamaguchi, *Basic Semiconductor Physics*, 1st Edition. page 230 (Springer, Berlin, 2001).

[24] B. L. Altshuler, A. G. Aronov, and D. E. Khmel'nitskii, *Effects of electron-electron collisions with small energy transfers on quantum localization*, J. Phys.C **15**, 7367 (1982).

CHAPTER 9

9. EXCHANGE BIAS EFFECT OF $Ge_{1-x}Mn_xTe$ WITH ANTIFERROMAGNETIC MnTe AND MnO MATERIALS

In this Chapter we aim to investigate the exchange bias (EB) effect between the FM $Ge_{1-x}Mn_xTe$ and AFM layer using either MnTe or MnO. In the case of GeMnTe/MnTe bilayer, we observe only an enhancement of coercivity, while in GeMnTe/MnO bilayer, both the hysteresis loop-shift and enhancement of the coercivity are observed. The T_c and the blocking temperature (T_B) of GeMnTe/MnO bilayer are 60 K and 20K, respectively as compared to the T_c ~ 95 K of a GeMnTe single layer.

9.1 Introduction and Motivation

The study of EB effect between FMS and AFM materials has attracted much attention as it provides a strong motivation for their integration into potential spintronic devices [1,2,3,4,5]. The manifestations of EB effect are notably the coercivity enhancement as well as shift in the hysteresis loop. In widely studied $Ga_{1-x}Mn_xAs$, proximity effects on the magnetic properties when interface with either MnTe or ZnMnSe have been studied [1]. However, only enhancement in coercivity has been observed in these samples. On the other hand, EB coupling was reported in $Ga_{1-x}Mn_xAs$ [2,3] and Cr doped GaN [4] by using an AFM MnO overlayer. In other

FM semiconductors, such as ZnCoO when coupled to NiO, the vertical shift in the hysteresis loop is observed as well [5]. Recently, EB effect was also observed in FM IV-VI $Ge_{1-x}Mn_xTe$ and it was attributed to the coexistence of FM $Ge_{1-x}Mn_xTe$ and AFM MnTe phases arising from the phase separation [6]. Apart from this report, there has been no report of EB in GeMnTe from a grown FM/AFM bilayer structure. In this Chapter, we present the EB results of GeMnTe/MnTe and GeMnTe/MnO bilayer structures grown by MBE.

In most studied cases of exchange bias system, the condition $T_B < T_N << T_c$ is met, where T_N is the Néel temperatures of the AFM layer [7]. When cooling with an applied field (H_{FC}) at $T > T_N$ through the T_N, the AFM spins are aligned to the FM spins and the coupling between them results in the EB effect. Both MnTe and MnO are well known to exhibit AFM properties below their respective T_N. For bulk hexagonal and zinc-blende MnTe, the T_N values are 310 K [8] and 65 K [9], respectively while the bulk MnO is 118 K [10]. In this study, the MnTe acquired a zinc-blende structure and the T_c of a single GeMnTe layer is ~ 95 K. The coupling effect for both kinds of bilayer, i.e. GeMnTe/MnTe and GeMnTe/MnO are studied. The magnetic properties of these bilayers are investigated and compared to a GeMnTe single layer in order to understand the proximity effects.

9.2 Experimental Details

The samples were grown by low temperature MBE on GaAs (100) substrates. The detailed growth of the GeMnTe grown on GaAs is discussed in Chapter 4 and growth conditions used to grow the GeMnTe is similar to that of Sample L. A 120 nm thick buffer layer of ZnTe was first deposited at substrate temperature, T_s = 250 °C, followed by ~ 200 nm thick FM GeMnTe single layer at T_s = 180 °C. Next, the AFM layer of either MnTe (~ 20 nm) or Mn (~ 50 nm) was deposited at T_s = 180 °C and 40 °C, respectively. During the growth process the surface quality of the samples was monitored by *in situ* RHEED. The crystal lattice mismatch between zinc-blende ZnTe and cubic GeTe is about 2 %. This allows the GeMnTe layer to be grown on ZnTe without much strain and distortion. The RHEED pattern during the growth of GeMnTe has a streaky 3×3 surface reconstruction (see Figure 4.11) suggesting the good crystalline quality of the layer. A post-annealing process was performed on the sample with Mn capping using a rapid thermal annealing system at 150 °C for 2 minutes in an oxygen atmosphere. The crystal structures of the films were studied by Cu $K\alpha$ high-resolution XRD. The XRD 2θ scan of the bilayers are shown in Figure 9.1. The broad peak observed near 2θ angle ~ 63 ° of the GeMnTe/MnTe sample can be resolved and identified to be originated from GeMnTe (400) and MnTe (400).

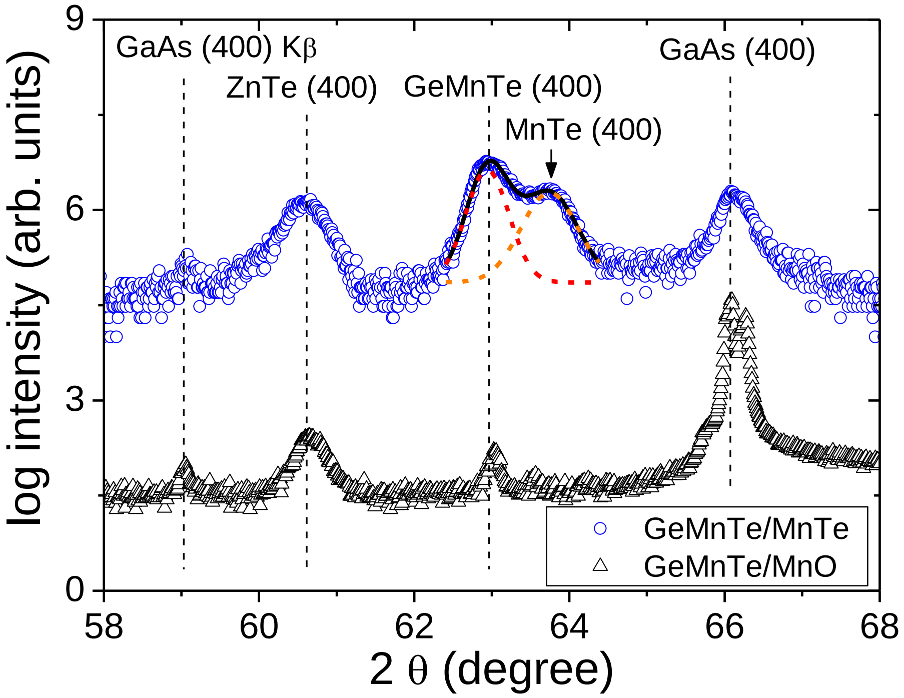

Figure 9.1 The XRD 2θ scan of GeMnTe/MnTe and GeMnTe/MnO samples.

Thus the 2θ scan peaks at 62.94 °, 60.56 °, and 63.60 ° correspond to the rock-salt GeMnTe (400), zinc-blende ZnTe (400) and MnTe (400) with lattice constants of 5.90 Å, 6.10 Å and 5.85 Å, respectively. However, we did not observe any peak attributed to the MnO layer for GeMnTe/MnO bilayer. The Mn composition of GeMnTe was estimated to be $x \sim 0.35$ using the XPS.

9.3 Results and Discussion

9.3.1 Proximity effect in GeMnTe/MnTe bilayer.

Figure 9.2 shows the temperature (*T*) and magnetic field (*H*) dependence of magnetization (*M*) for a GeMnTe single layer and a GeMnTe/MnTe bilayer samples.

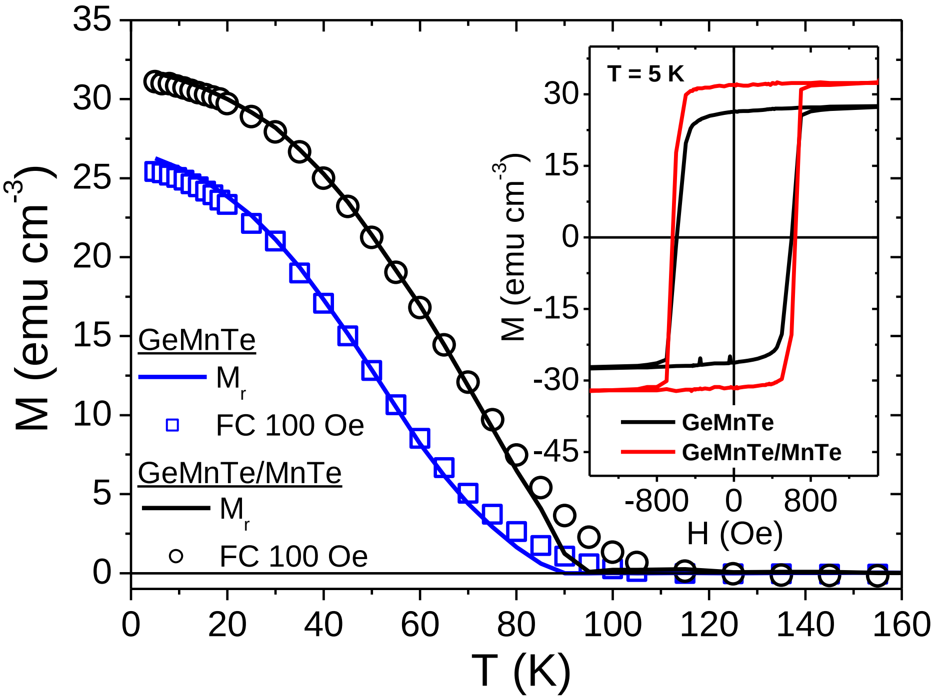

Figure 9.2 Temperature dependence of the M_r (solid lines) and FC magnetization curves (open symbols) at 100 Oe for GeMnTe single layer and GeMnTe/MnTe bilayer. The inset shows the ZFC and FC hysteresis loops of GeMnTe and GeMnTe/MnTe, respectively at 5 K after cooling with H_{FC} = 1 T from 300 K.

The magnetic properties were measured with H applied parallel to the plane of the sample. The field-cooled (FC) magnetization curves were measured with a cooling field of 100 Oe applied at 300 K. It can be observed that the temperature dependence of the remanent (M_r) and the FC magnetizations show convex shapes for both samples. The T_c of both samples are ~ 95 K. In order to examine the EB effect, the hysteresis loops (M-H) for GeMnTe and GeMnTe/MnTe are measured at 5 K as shown in the inset of Figure 9.2. The GeMnTe/MnTe bilayer was measured after a FC process with a H_{FC} = 1 T applied at T = 300 K. There is no obvious shift observed in the M-H loop except for an enhancement in the coercivity (H_C) by ~ 48 Oe. Similar observations were also observed for GaMnAs/GaAs/MnTe system [2,3]. This can be attributed to a small magnetic anisotropy of the zinc-blende MnTe layer which is sufficient to support an enhancement of H_C but not an exchange bias effect [11,12]. Additionally, it is well known that the exchange bias field (H_E) varies inversely with the thickness of the FM layer [7,13]. As such, a GeMnTe thickness of 200 nm might be too large to result in an observable shift in the *M-H* loop. However, attempts to observed shift in the *M-H* loop using thinner GeMnTe are not successful.

9.3.2 Exchange bias effect in GeMnTe/MnO bilayer.

Figure 9.3 shows the zero field-cooled (ZFC) *M-H* loop at 5 K and FC *M-H* loop at various temperatures of GeMnTe/MnO bilayer, after cooling with H_{FC} = 1 T from 300 K. The ZFC *M-H* loop exhibits no shift from the origin and the H_C obtained is ~ 3800 Oe and it is larger than that of GeMnTe single layer (H_C ~ 590 Oe). This indicates that some degree of coupling is induced due to the presence of the AFM layer even after zero field-cooling [12,13]. However, since the AFM spins are not aligned during the cooling process, the induced coupling at the interface with the FM spins would be random. Consequently, only the H_C enhancement rather than a hysteresis loop shift is observed.

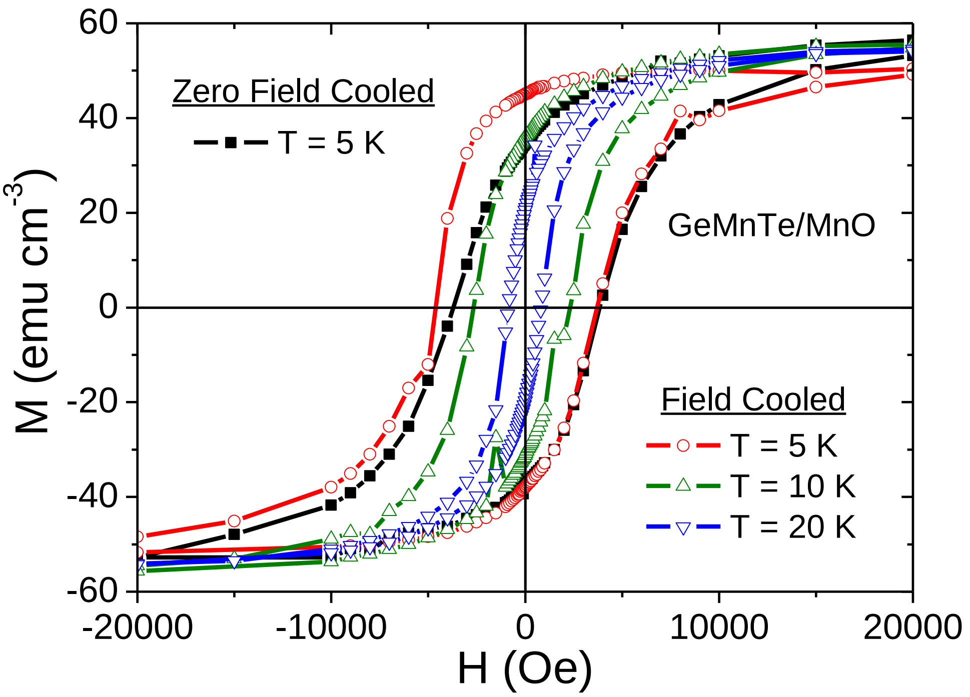

Figure 9.3 ZFC hysteresis loop at 5 K and FC at T = 5, 10 and 20 K of GeMnTe/MnO sample after cooling with H_{FC} = 1 T from 300 K.

In the case of field-cooling process, the coercivity (H_C ~ 4100 Oe) and the hysteresis loop shift as well as a vertical upward shift (δM) of the *M-H* loop are observed. These *M-H* loops are measured up to magnetic field of 2 T to ensure that saturation magnetization is reached and the shifts in the *M-H* loops are not due to minor loop effect. The occurrence of δM suggests possibly the presence of uncompensated pinned spins at the FM/AFM interface [5]. We use a separate GeMnTe single layer as a controlled sample and annealed it in the same condition as the GeMnTe/MnO bilayer. Our results show that the annealed GeMnTe single layer shows no hysteresis loop shift after the field-cooling process except for a slight increase in H_C of 60 Oe.

Thus, the observed EB effect in GeMnTe/MnO bilayer is not likely to be attributed to the AFM MnTe cluster (due to the phase separation of GeMnTe arising from the annealing process) but as a result of the AFM MnO layer.

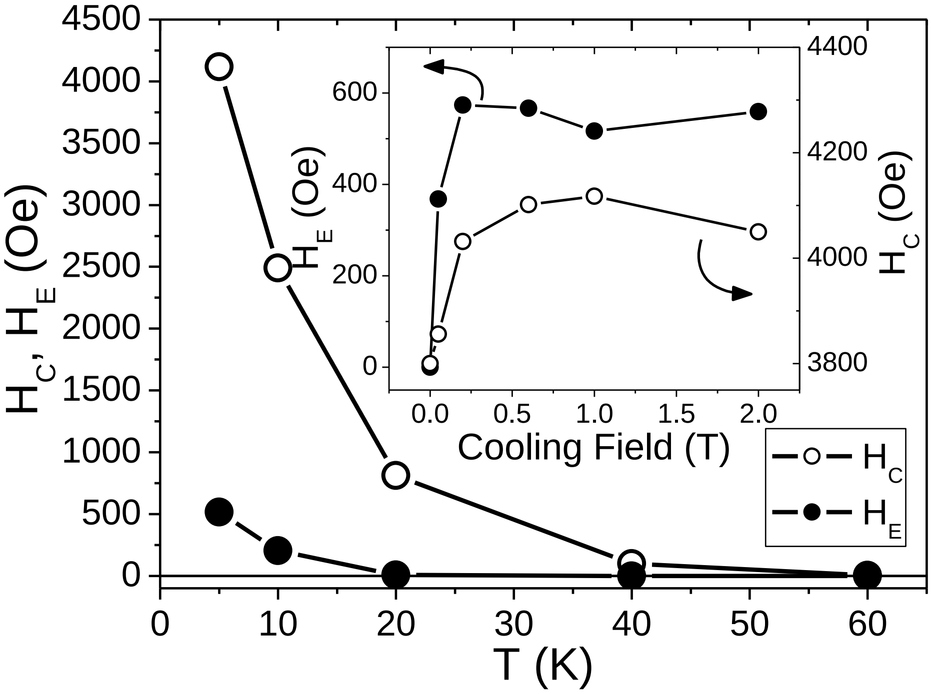

Figure 9.4 The H_C and H_E as function of temperatures for H_{FC} = 1 T. The inset shows the cooling field dependence of H_C and H_E obtained from the hysteresis loops measured at 5 K.

Figure 9.4 presents the H_C and H_E as a function of temperature obtained from the FC *M-H* loops with H_{FC} = 1 T. The H_C and H_E values are obtained as $H_E = \left(H_C^+ + H_C^-\right)/2$ and $H_C = \left(H_C^+ - H_C^-\right)/2$ where H_C^+ and H_C^- are the positive and negative field axis intercepts, respectively. It is observed that the H_C decreases with temperature and ceases to exist at *T* = 60 K. This suggests that the T_c of

GeMnTe/MnO bilayer is lower than that of GeMnTe single layer (T_c ~ 95 K). The T_B ~ 20 K where H_E vanishes. In most cases, the value of T_B is correlated to the grain size and thickness of the AFM layer [7,12]. For EB systems with thick AFM layers, usually $T_B \approx T_N$, while for other systems with very thin or polycrystalline AFM layers, $T_B << T_N$. The obtained T_B in GeMnTe/MnO is found to be much lower than the T_N of bulk manganese oxides, such as MnO (118 K) [10], MnO_2 (92 K) [14], Mn_2O_3 (79 K) [15] and Mn_3O_4 (43 K) [15,16] as shown in Table 9.1.

Table 9.1 The structures and Neel temperature (T_N) of bulk manganese oxides.

Compounds	Structure	T_N	References
MnO	Rock-salt a = 4.445 Å	118 K	[10]
MnO_2	Tetragonal Pyrolusite a = 4.387 ± 0.005Å c = 2.860 ± 0.002Å	92 K	[14]
Mn_2O_3	Orthorhombic a = 9.414 Å b = 9.424 Å c = 9.405 Å	79 K	[15]
Mn_3O_4	Tetragonal Hausmanite a = 5.756 ± 0.005Å c = 9.441 ± 0.003Å	43 K	[15,16]

However, it does correspond to the T_B of MnO nanoparticles [17]. The cooling field dependence of H_C and H_E are shown in the inset of Figure 9.4, where both are found to saturate beyond H_{FC} = 0.2 T. This shows that the expansion in H_C is correlated to the EB effect.

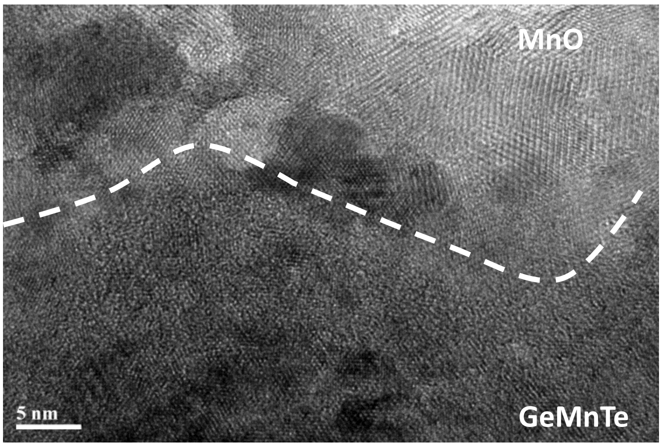

Figure 9.5 A TEM image of the interface between the GeMnTe and MnO layers.

The interface between the two layers was characterized using the TEM as shown in Figure 9.5. It reveals that the interface is not clear and the MnO layer is polycrystalline. The waviness of the interface could be resulting from the oxidation of the bottom GeMnTe layer owing to an oxidised Mn capping layer. As for the polycrystalline nature of the MnO layer, it can be attributed to the large lattice mismatch between MnO and the underneath GeMnTe layer. Since exchange bias is an interfacial effect, the origin of the observed exchange bias can be due to MnO clusters with various crystal orientations along the uneven GeMnTe/MnO interface. We have attempted to grow thicker Mn and annealing it to achieve thicker MnO layer but the oxide layer thickness remains either thin or polycrystalline.

We note that disordered and dilute magnetic spins in a crystal can lead to a glassy behavior that gives rise to EB effect below the spin freezing temperature [18,19]. In order to elucidate this feature, we have performed ZFC magnetization as a function of temperature measured at various applied fields as shown in Figure 9.6 (a). The peak position (T_p) shifts to lower temperatures with increasing applied field. The T_p versus $H^{2/3}$ dependence plotted in Figure 9.6 (b) shows a nonlinear trend which disagrees with the de Almeida-Thouless behavior [19]. Hence, the possibility of an exchange bias induced by spin-glass behaviors can be rule out.

Figure 9.6 (c) shows the ac susceptibility measurement which only one peak at T ~ 95 K can be observed. This value corresponds well with the T_c of the GeMnTe single layer. The ac susceptibility measurements were carried out with an oscillating field of 5 Oe at frequency of 2 and 263 Hz. Such oscillating field methodology should completely suppress the EB effect and the result should be equivalent to that of a single FM layer. We note that the T_c obtained from the ac susceptibility measurement differs with that acquired from the H_C versus temperature plot as shown in Figure 9.4.

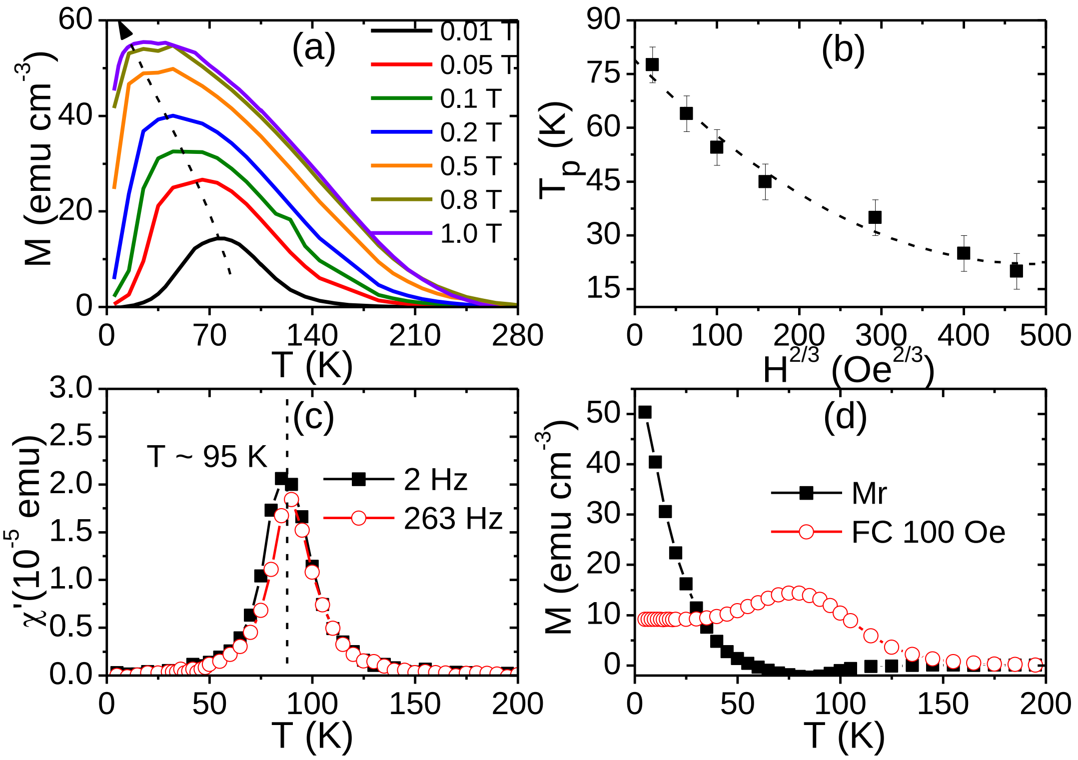

Figure 9.6 (a) ZFC magnetization curve measured at various applied fields; (b) The applied field ($H^{2/3}$) as a function of T_p; (c) The ac susceptibility measured at H = 5 Oe and a frequency of 2 and 283Hz and (d) Temperature dependence of the M_r and FC magnetization curves at 100 Oe. All measurements are for for GeMnTe/MnO.

To understand this discrepancy, we have further performed magnetization dependence of temperature of GeMnTe/MnO sample and the results are shown in Figure 9.6 (d). The temperature dependence of M_r is found to decrease in a concave manner and cease to exist at 60 K. While the FC magnetization measured with 100 Oe applied field shows a non-vanishing magnetization persisting up to 140 K. This suggest that in the absence of an applied field (M_r-T curve) as temperature is increased above T_B, the randomization of the AFM spins also causes disorder in the FM spins due to coupling effect between them resulting T_c to occur at 60 K. However, in the presence of a 100 Oe applied field (FC M-T curve), it is sufficient to sustain some of the AFM spins even above T_B. Consequently, the exchange coupling between the FM and AFM spins result in a magnetic ordering above 95 K and vanished only at 140 K.

9.4 Summary

In this Chapter the exchange biasing of a GeMnTe layer by either a MnTe or MnO overlayer is being studied. For GeMnTe/MnO bilayer, the magnetic measurements show that the sample has a larger coercivity field (4100 Oe), than is observed in a single GeMnTe layer (590 Oe). The hysteresis loop shows a clear shift to a negative magnetic field when measured after a positive field cooling. We have rule out the possibility on the existence of phase separation and spin-glass behavior but rather the observed exchange bias is attributed to the presence of MnO grains or clusters at the MnO/GeMnTe interface with $T_B \sim 20\,\mathrm{K}$. Additionally, we note that as the temperature is raised beyond T_B in the absence of an applied field, the randomization of the AFM spins also reduces the overall magnetization of the GeMnTe/MnO sample. In the case of GeMnTe/MnTe, only an enhancement of coercivity by 48 Oe is observed as compared to a single GeMnTe layer. This could be due to the small magnetic anisotropy of the zinc-blende MnTe and a relatively thick GeMnTe layer.

Chapter 9 References

[1] J. K. Furdyna, X. Liu, Y. Sasaki *et al.*, *Ferromagnetic III–Mn–V semiconductor multilayers: Manipulation of magnetic properties by proximity effects and interface design (invited),* J. Appl. Phys. **91**, 7490 (2002).

[2] K. F. Eid, M. B. Stone, K. C. Ku *et al.*, *Exchange biasing of the ferromagnetic semiconductor* $Ga_{1-x}Mn_xAs$, Appl. Phys. Lett. **85**, 1556 (2004).

[3] K. F. Eid, M. B. Stone, O. Maksimov *et al.*, *Exchange biasing of the ferromagnetic semiconductor (Ga,Mn)As by MnO (invited)*, J. Appl. Phys. **97**, 10D304 (2005).

[4] H. X. Liu, Stephen Y. Wu, R. K. Singh, and N. Newman, *Exchange biasing of ferromagnetic Cr-doped GaN using a MnO overlayer*, J. Appl. Phys. **98**, 046106 (2005).

[5] Po-Hsiang Huang, Hsin-Hung Huang, and Chih-Huang Lai, *Coexistence of exchange-bias fields and vertical magnetization shifts in ZnCoO/NiO system*, Appl. Phys. Lett. **90**, 062509 (2007).

[6] R. T. Lechner, G. Springholz, M. Hassan *et al.*, *Phase separation and exchange biasing in the ferromagnetic IV-VI semiconductor* $Ge_{1-x}Mn_xTe$, Appl. Phys. Lett. **97**, 023101 (2010).

[7] J. Nogués, I. K. Schuller, *Exchange bias*, J. Magn. Magn. Mater. **192**, 203 (1999).

[8] C. Reig, V. Muñoza,b, C. Gómez *et al.*, *Growth and characterisation of MnTe crystals,* J. Crystal Growth **223**, 349 (2001).

[9] B. Hennion, W. Szuszkiewicz, E. Dynowska *et al.*, *Spin-wave measurements on MBE-grown zinc-blende structure MnTe by inelastic neutron scattering*, Phys. Rev. B **66**, 224426 (2002).

[10] A. P. Kantor, L. S. Dubrovinsky, N. A. Dubrovinskaia *et al.*, *Phase transitions in MnO and FeO at low temperatures: A neutron powder diffraction study*, J. Alloys Comp. **402**, 42 (2005).

[11] A. E. Berkowitz, K. Takano, *Exchange anisotropy - a review*, J. Magn. Magn. Mater. **200**, 552 (1999).

[12] J. Nogués, J. Sort, V. Langlais *et al.*, *Exchange bias in nanostructures*, Phys. Rep. **422**, 65 (2005).

[13] P. Miltényi, M. Gierlings, M. Bamming *et al.*, *Tuning exchange bias*, Appl. Phys. Lett. **75**, 2304 (1999).

[14] R. A. Robie and B. S. Hemmingway, *Low-temperature molar heat capacities*

and entropies of MnO_2 (pyrolusite), Mn_3O_4 (hausmanite), and Mn_2O_3 (bixbyite), J. Chem. Thermodyn. **17**, 165 (1985).

[15] S. Geller and G. P. Espinosa, *Magnetic and Crystallographic Transitions in Sc^{3+}, Cr^{3+}, and Ga^{3+} Substituted Mn_2O_3*, Phys. Rev. B **1**, 3763 (1970).

[16] D. Jarosch, *Crystal Structure Refinement and Reflectance Measurements of Hausmannite, Mn_30_4*, Mineral. Petrol. **37**, 15 (1987).

[17] A. E. Berkowitz, G. F. Rodriguez, J. I. Hong *et al.*, *Antiferromagnetic MnO nanoparticles with ferrimagnetic Mn_3O_4 shells: Doubly inverted core-shell system*, Phys. Rev. B **77**, 024403 (2008).

[18] M. Ali, P. Adie, C. H. Marrows *et al.*, *Exchange bias using a spin glass*, Nature Mater. **6**, 70 (2007).

[19] D. P. Shoemaker, E. E. Rodriguez, R. Seshadri *et al.*, *Intrinsic exchange bias in $Zn_xMn_{3-x}O_4$ ($x<1$) solid solutions*, Phys. Rev. B **80**, 144422 (2009).

CHAPTER 10

10. CONCLUSIONS AND OUTLOOK

Tremendous effort has been devoted into the research of FMSs in the past decade to realize novel practical devices with multifunctional capabilities. Although, the T_c in these materials has yet to reach a technologically significant value, they have already critical role in advancing material characterization tools and exploring new physics and concepts in spintronics. Apart from the widely studied $Ga_{1-x}Mn_xAs$, $Ge_{1-x}Mn_xTe$ emerged to be one of the carrier mediated FMS to achieve a high T_c of ~200 K. This thesis focuses on the study of magnetic and transport properties of $Ge_{1-x}Mn_xTe$ thin films grown by MBE. The important results and findings are summarized below.

In Chapter 4, the effects of various growth conditions, such as GeTe, Mn, Te fluxes and T_s on the physical properties of $Ge_{1-x}Mn_xTe$ grown using MBE on BaF_2 and GaAs substrates have been presented. The T_s have to be sufficiently low, 180°C and 250 °C for GaAs and BaF_2, respectively, for the surface adsorption of Ge atoms and also a homogenous layer to be grown. Although excess Te flux improves the surface roughness and crystal quality of the film, excessive Te flux also results in separate phases of GeTe and $Ge_{1-x}Mn_xTe$. For films grown on GaAs, the use of a relatively low GeTe or Mn flux can result in single crystallographic orientation of

{200} or {111}, respectively. Under these appropriate growth conditions homogeneous $Ge_{1-x}Mn_xTe$ has been achieved in both BaF_2 and GaAs substrates.

In Chapter 5, the magnetotransport measurements performed on $Ge_{1-x}Mn_xTe$ (x = 0.1) show concave *M*-*T* behaviour and two magnetic transition temperature at T_c = 34±5 K and T_c^* = 100±5 K. The T_R corresponding to the minimum in $\rho(T)$ can be used as an indication of the T_c, which corresponds well with the extrapolation from the point of inflection of the *M(T)* curve. This minimum in $\rho(T)$ is likely to result from both the contribution of weak localization and phonon-scattering. The deviation of the *M*-*T* from the Bloch's law, which exudes a convex *M*-*T* trend, suggests the presence of disordering within the sample. The T_c^* can be inferred as short range ferromagnetic order due to insufficient carriers to generate uniform ferromagnetism that leads to ferromagnetic clusters while T_c is ascribed to a long range ferromagnetic order.

In Chapter 6 and 7, the T_c of $Ge_{1-x}Mn_xTe$ (x = 0.1 and 0.3) is tunned by hydrostatic pressure effect. The RKKY and the two VB models are invoked to explain the results. The factors influencing the T_c can be identified as ρ_o, a_o, $F(2k_F R_{ij})$ and J_{pd}. The increase in T_c with pressure for both samples (x = 0.1 and 0.3) is mainly due to the increase in carrier concentration and exchange interaction between Mn ions and hole carriers. However, owing to the higher Mn ions concentration in x =

0.3 sample, the effect of antiferromagnetic superexchange becomes more prominent than that of $x = 0.1$ as lattice constant is reduced, leading to the suppression of T_c.

In Chapter 8, magnetoresistance measurement were performed on the $Ge_{1-x}Mn_xTe$ ($x = 0.3$) at various applied pressures and temperatures. From Hall resistivity analysis, the system is shown to be in the metallic regime within the temperature range studied. The MR is characterized by both positive and negative contributions, which can be described by the antilocalization and weak localization models. The spin-orbit scattering time is found to be the dominant mechanism and is independent of pressure and temperature. The phase coherent length is associated with the e-e scattering and found to increase with pressure but saturates at high pressure due to the increase in effective scattering rate.

In Chapter 9, the exchange bias effect is observed in GeMnTe layer with MnTe or MnO AFM overlayer. A significant coercivity field enhancement is observed for the GeMnTe/MnO bilayer (4200 Oe) as compared to that of a single GeMnTe layer (590 Oe). Its hysteresis loop also shows a clear shift to a negative magnetic field when measured after a positive field cooling. We have rule out the possibility on the existence of phase separation and spin-glass behavior but rather the observed exchange bias is attributed to the presence of nanoparticle-like MnO grains or clusters at the MnO/GeMnTe interface with $T_B \sim 20\,\mathrm{K}$. In the case of GeMnTe/MnTe, only an enhancement of coercivity by 48 Oe is observed as compared to a single GeMnTe layer. This could be due to the small magnetic anisotropy of the zinc-blende MnTe and a relatively thick GeMnTe layer.

Overall, these results provide useful information in achieving high quality $Ge_{1-x}Mn_xTe$ in attaining high T_c. The interplay between carrier localization and magnetism which is an important topic in FMS is also discussed. The exchange bias effect using $Ge_{1-x}Mn_xTe$ and AFM layer is also demostrated. To date, $Ge_{1-x}Mn_xTe$ remains a promising FMS and our findings pose challenges as well as opportunities for future studies of $Ge_{1-x}Mn_xTe$ for spintronic applications.